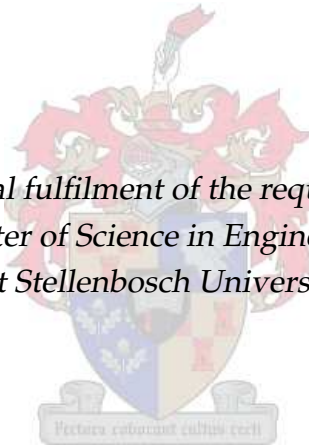


Probes in HF Metrology

by

Daniël Johannes Rossouw

*Thesis presented in partial fulfilment of the requirements for the degree of
Master of Science in Engineering
at Stellenbosch University*



Supervisor: Prof. Howard Charles Reader
Department of Electrical and Electronic Engineering

December 2010

Declaration

By submitting this thesis electronically, I declare that the entirety of the work contained therein is my own, original work, that I am the owner of the copyright thereof (unless to the extent explicitly otherwise stated) and that I have not previously in its entirety or in part submitted it for obtaining any qualification.

December 2010

Abstract

Flanged coaxial probes are widely used to conduct accurate, broadband permittivity measurements of various dielectric materials. A metrology study, discussed in [1], revealed that small perturbations in measured permittivity data, are due to escaping common-mode (CM) current that propagates onto exposed VNA feed cabling. This is not considered in published permittivity extraction algorithms, like the National Institute of Standards and Technology (NIST) full-wave code that assumes an infinite flange radius. To characterise this effect we validate a finite volume time domain (FVTD) CST simulation model of an SMA coaxial probe, by probing sensitive E-fields in a metallic shielding cylinder, placed around it.

For this process, electro-optic (EO) E-field sensors are considered and a Mach-Zehnder type sensor is designed. Manufacturing difficulties discontinues this approach, but the revisited extended centre conductor E-field probing technique proves successful. The technique entails a high dynamic range, two-port VNA measurement. Through CST we gain knowledge of the physics behind the CM-problem and the behaviour of fields around the coaxial probe. Different shielding environments are simulated to establish their ability to impede CM-current coupling onto measurement cabling.

To study the CM-effect on extracted permittivity results, the investigation is extended to Short-Open-Load (SOL) calibrated face-plane measurements of dielectric solids. A CST model, which considers escaping CM-energy, is used to generate open circuit (OC) calibration coefficients and to serve as an independent extraction method. We inspect the effect of different shielding environments and through CST, extract accurate permittivity results for ϵ'' , to a degree not previously achieved for such systems. This allows comment on the infinite-flange-radius assumption of the NIST method and proves the significance of the CM-effect.

Samevatting

Geflensde koaksiale probes word algemeen in die praktyk gebruik om akkurate, wyeband permitiwiteitmetings van diëlektriese materiale te verrig. 'n Studie wat in [1] bespreek word, dui aan dat klein verskynsels in gemete resultate, verband hou met gemene-modus (GM) stroom, wat ontsnap en teenwoording is aan die buitekant van onbeskernde voerkabels. Hierdie verskynsel word nie deur huidige volgolf ekstraksie-algoritmes, soos die van NIST wat 'n onëindige flensradius aanvaar, in ag geneem nie. Om die GM-effek te karakteriseer, verifieer ons 'n eindige-volume tyd-gebied CST simulasiemodel, deur sensitiewe metings binne 'n silindriese metaalskerm, wat om so 'n probe geplaas word.

Vir hierdie meting word elektro-optiese E-veld probes eers oorweeg. In gevolg word 'n Mach-Zehnder-tipe probe ontwerp, maar vervaardigingsprobleme en tyd-oorwegings kniehalter hierdie benadering. Heroorweging van die verlengde koaksiale sentraalgeleier, E-veld-probe tegniek, wat hoë dinamiese bereik twee-poort netwerkanaliseerder metings behels, slaag uiteindelik in hierdie doel. CST maak dit nou moontlik om die GM stroomprobleem te simuleer en spesifieke veldgedrag te kan waarneem. Verskillende afskermingsmetodes se vermoë om GM-koppeling na kabels te beperk word ondersoek.

Die GM studie word uitgebrei na SOL-gekalibreerde, flensvlakverwysde permitiwiteitmetings van diëlektriese vastestowwe. 'n CST model, wat GM stroom in ag neem, word gebruik om oopgeslote kalibrasiekofisiënte te genereer en dien ook as 'n alternatiewe permitiwiteit ekstraksiemetode. Die effek van die verskillende afskermingstegnieke word ondersoek en deur die CST metode te gebruik, word 'n aansienlike verbetering in akkuraatheid van ϵ'' waardes verkry. Dit regverdig kommentaar oor die aannames wat in die NIST metode gemaak word en beklemtoon die belangrikheid om GM stroom in ag te neem.

Acknowledgements

I acknowledge my Saviour, Jesus Christ, through whom all things are possible.

I would like to thank the following individuals and institutions who have contributed to the success of this project:

- Prof H.C. Reader for his meticulous nature, his guidance, support and humour.
- My parents and brother for their love and support.
- Ulrich Buttner for his talents with a Leatherman and his friendship.
- Wessel, Lincoln and Martin Siebers for their friendly advice and support.
- Prof E. Rohwer and Alexander Heidt at the US physics department for their support.
- Prof K.D. Palmer, Prof D. Davidson and other academic staff for their open doors!
- My colleagues: Paul, Braam, Gideon, Evan, Eben, Philip, Andre, Alwyn, Carlo and all the others, for the memorable times.
- Van Zyl De Villiers and Bert Bekker at NECSA for handling many frustrations.
- Dr. Nkosi at iThemba labs and Rikus Cronje at Zeiss.
- CST for their gracious support to the US E&E dept.
- NIST for the use of their extraction algorithm
- Concept to Volume for the use of their optical simulation software

Contents

Contents	6
List of Figures	8
List of Tables	12
1 Introduction	2
1.1 Thesis layout	2
2 Literature Study	4
2.1 Measuring Permittivity	4
2.2 Coaxial Probe: A Transmission Line Method	5
2.3 Probe Measurement Procedure	6
2.4 Coaxial Probe Developments	7
2.5 CM-Current Effects	10
2.6 Optical E-field Sensors	11
2.7 Conclusion	14
3 Mach-Zehnder Design and Simulation	15
3.1 Linear Electro-Optic Effect in LiNbO ₃ Crystal	15
3.2 Mach-Zehnder Theory	16
3.3 Titanium Diffusion in LiNbO ₃	19
3.4 Design Considerations	20
3.5 Mach-Zehnder Waveguide Design	20
3.6 Electrode Design	27
3.7 Mask layout	28
3.8 System Topology and Test Strategy	30
3.9 Conclusion	31
4 Mach-Zehnder Manufacture	32
4.1 Fabrication Process Overview	32
4.2 Lithography	33
4.3 Titanium Deposition	36

4.4	Lift-off	40
4.5	Diffusion	41
4.6	Conclusion	43
5	Exterior Field Analysis	44
5.1	The Coaxial Probe	44
5.2	CST Simulation	45
5.3	VNA Field Probing Measurements	49
5.4	Field Discussion	56
5.5	Coaxial Probe Environments	57
5.6	Conclusion	60
6	Material Property Measurements	61
6.1	System Background	62
6.2	Traceability and Strategy	62
6.3	CST Simulation	63
6.4	Face-Plane-Calibrated Measurements	69
6.5	Material Property Extraction	73
6.6	Discussion	77
6.7	Conclusion	79
7	Conclusion	80
7.1	Recommendations	81
	Appendices	82
A	Other S21 Field Results	83
B	CST and NIST OC Coefficients	84
	Bibliography	85

List of Figures

2.1	Coaxial Transmission Line Configurations for permittivity measurement from [2].	6
2.2	Open-ended SMA coaxial probe with panel-mount flange.	6
2.3	Probe showing bead burr extending over the outer conductor.	8
2.4	Exposed-core multimode fibre with PDLC coating form [3].	12
2.5	D-fibre sensor embedded under electronic circuit components from [4].	12
2.6	Mach-Zehnder interferometer structure from[5].	13
2.7	E-field sensor with segmented electrodes from[3].	13
3.1	Basic Mach-Zehnder operation: a) Zero voltage across electrodes: output is in-phase and b) Voltage applied: output phase-cancellation.	17
3.2	Electrode configurations for two LiNbO ₃ crystal cuts: a) X-cut: horizontal field and; b) Z-cut: vertical field.	17
3.3	Mach-Zehnder transfer-function.	18
3.4	Change in local refractive index after Titanium diffusion in LiNbO ₃	19
3.5	Calculated optical bend-loss in dB vs bend length for a fixed 27 μ m horizontal bend-offset. Three cases of initial Titanium film thickness, given in Angstrom are plotted. Constant diffusion parameters are stated above.	23
3.6	C2V design-view of Mach-Zehnder waveguide bend-curves. Shown with adapted width-to-length aspect ratio.	24
3.7	Complete Mach-Zehnder design with asymmetric waveguide bends.	24
3.8	3D-view of 1D effective index profile after Titanium diffusion.	24
3.9	Mach-Zehnder with zero phase-shift: a) Optical wave-propagation; b) End-field comparison.	26
3.10	Mach-Zehnder with 90 degree phase-shift: a) Wave-propagation; b) End-field comparison.	26
3.11	Mach-Zehnder with 90 degree phase-shift: a) Wave-propagation; b) End-field comparison.	26
3.12	Electrode designs: a) Z-cut test electrodes; b) X-cut test electrodes; c) Z-cut, four-element, segmented electrodes; d) X-cut, four-element, segmented electrodes. . .	27
3.13	CST plane-wave excitation in simulation of segmented electrode.	28
3.14	CST simulation results: electrode vector E-field distribution at 500 MHz.	28

3.15	View of final mask layout in C2V. Bottom-left: generic waveguide patterns. Top-left: X-cut electrode patterns. Top-right and bottom-right: Z-cut electrode patterns.	29
3.16	Independent, fibre-connected system with laser diode (LD) on the input and photodiode (PD) at the output. A stable DC supply feeds the LD and the PD connects to a spectrum analyser.	30
3.17	Preliminary test system using bulk optics and an optical spectrum analyser.	30
4.1	Illustration of the required fabrication process to manufacture the optical E-field sensor.	33
4.2	Microscope view of lithography.	34
4.3	AFM scan of lithography.	34
4.4	Undercut edges achieved through prolonged development.	35
4.5	Illustration of photoresist edge-bead and induced mask offset which influences UV-exposure.	35
4.6	Under-exposure due to edge bead.	35
4.7	Successful channel after experimentation.	35
4.8	Standard Tungsten boat with low resistance and insufficient temperature.	36
4.9	Modified, narrower Tungsten boat with increased resistance and higher temperature.	36
4.10	Pulsed Laser Deposition (PLD).	37
4.11	Poor Titanium film by PLD.	37
4.12	Cross-section illustration of Inverse Cylindrical Magnetron (ICM).	38
4.13	ICM plasma during deposition, seen through viewing glass.	38
4.14	Cryo-cooled, high-vacuum e-Beam evaporator at iThemba labs.	39
4.15	Inside the chamber: Copper crucible with filament, large U-magnet and Titanium evaporant.	39
4.16	Lift-off in Acetone taking place in a Pyrex beaker.	40
4.17	AFM scan of a Mach-Zehnder structure after clean Titanium lift-off.	40
4.18	Illustration of furnace setup for Titanium diffusion after [6].	41
4.19	Quartz tube at furnace entrance.	41
4.20	Diffusion setup, as shown in Fig. 4.18.	41
4.21	AFM scans of diffusion results with: a) Titanium structure before diffusion; b) X-cut for 6 hrs at 1050 °C; c) X-cut for 9 hrs at 1050 °C; and d) Z-cut for 6 Hrs at 1050°C.	42
5.1	Cut-plane illustration of coaxial probe with surrounding shield and side E-field probe.	45
5.2	3D view of coaxial probe with semi-transparent shield and E-field probe on the left.	45

5.3	Semi-ridged cable dimension is maintained through the female connector.	46
5.4	Simplification of interior transition from semi-ridged to male connector at the top.	46
5.5	Local meshing at coaxial probe flange.	48
5.6	Local meshing at E-field probe.	48
5.7	CST cut-plane mesh-view of coaxial probe, showing global and localised meshing.	48
5.8	VNA field probing: port one feeds the E-field probe and port two the coaxial probe.	50
5.9	Error-model for forward path of full two-port calibration from [7].	51
5.10	CST and VNA comparison of $ S_{21} $ field results in dB, for position one.	52
5.11	CST and VNA comparison of $ S_{21} $ field results in dB, for position three.	53
5.12	Field-probing measurement with Teflon on the coaxial probe face.	53
5.13	Comparison of probed $ S_{21} $ results in dB for Air, Teflon and Rexolite samples, placed on the coaxial probe.	54
5.14	E-field probe with and without a Bazooka balun.	55
5.15	EMCO current-probe placed around E-field probe to test for expected CM-current.	55
5.16	Comparison of probed $ S_{21} $ results at position 4, with and without a balun.	56
5.17	Scale-clamped E-field magnitude plot at 3 GHz with four E-field probes super-imposed.	57
5.18	Scale-clamped vector E-field plot at 3 GHz with an E-field probe at position 4.	57
5.19	Three levels of defined probe environment: a) bare probe: undefined environment; b) probe with shield base only: loosely defined and c) cut-plane view of fully-shielded probe: well defined. a) also shows the placement of the H-field probe for all three cases.	58
5.20	Simulated H-field strength (dBA/m) versus frequency for the H-field probe in the three environments, depicted in Fig. 5.19.	59
5.21	Scale-clamped E-field magnitude plot without field probes at 1.67 GHz.	59
5.22	Scale-clamped E-field magnitude plot without field probes at 2.5 GHz.	59
6.1	VNA and CST full-length de-trended results, both non-linear compared to the desired form of the NIST data set in blue. Dispersion in the semi-ridged bead is suspected to be the cause.	64
6.2	Coaxial probe face plane with port reference extension shown.	65
6.3	Simplification at top connector and semi-ridged cable.	65
6.4	Simplification at bottom female connector.	65
6.5	Cut-plane view of meshing for the fully-shielded case.	66
6.6	Cut-plane view of meshing for the NSB case.	66
6.7	Simplification at top connector and semi-ridged cable.	67
6.8	Coaxial probe face plane with port reference extension shown.	67
6.9	a) Comparison of computed OC phase-results and b) Zoomed-in view at 3 GHz. Computed results are from: NIST full-wave code; CST-NSB; and, CST-Shield models.	68

6.10	Polishing machine, used to flatten and polish the probe face.	69
6.11	Short Circuit with separate foam backing and brass contact foil on the left and Load calibration standard on the back right.	71
6.12	Measurement setup with clamp securing Load calibration standard. Data to memory comparison visible on VNA screen.	71
6.13	a) Measured $ S_{11} $ in dB and b) S_{11} phase in degrees for Air. Result comparison for: Shield, NSB and NIST probe environments.	72
6.14	a) Measured $ S_{11} $ in dB and b) S_{11} phase in degrees for Teflon. Result comparison for: Shield, NSB and NIST probe environments.	72
6.15	a) ϵ' and b) ϵ'' for Teflon from: NSB data with CST-derived OC coefficients for VNA calibration; NSB data with NIST-coefficients; and, Shield data with CST-coefficients.	74
6.16	a) ϵ' and b) ϵ'' for Rexolite from: NSB data with CST-coefficients; NSB data with NIST-coefficients; and, Shield data with CST-coefficients.	74
6.17	CST iterative matching a) ϵ' and b) ϵ'' for Teflon.	75
6.18	CST extracted permittivity for NSB-measured Teflon sample with: a) ϵ' and; b) ϵ''	76
6.19	Comparison of NIST and CST permittivity extraction for NSB-measured Teflon sample: a) ϵ' and; b) ϵ''	78
A.1	CST and VNA comparison of $ S_{21} $ field results in dB, for position two.	83
A.2	CST and VNA comparison of $ S_{21} $ field results in dB, for position four.	83

List of Tables

2.1	Comparison of popular permittivity measurement techniques	5
5.1	Global mesh settings.	47
6.1	Final measurement phase drift at 3 GHz.	72
6.2	Parameters used for the NIST inversion code.	73

Nomenclature

Symbols

Symbol	Name	Value	Symbol	Name	Value
a	atto	10^{-18}	k	kilo	10^3
f	femto	10^{-15}	M	Mega	10^6
p	pico	10^{-12}	G	Giga	10^9
n	nano	10^{-9}	T	Tera	10^{12}
μ	micro	10^{-6}	P	Peta	10^{15}
m	milli	10^{-3}	E	Exa	10^{18}

Abbreviations

Abbr.	Meaning	Abbr.	Meaning
AFM	Atomic Force Microscope	OSA	Optical Spectrum Analyser
BPM	Beam Propagation Method	PCB	Printed Circuit Board
C2V	Concept to Volume	PDLC	Polymer Dispersed Liquid Crystal
CM	Common-Mode	PLD	Pulsed Laser Deposition
DC	Direct Current	PM	Polarisation Maintaining
EMC	Electromagnetic Compatibility	RAM	Random Access Memory
EO	Electro-Optic	RIN	Random Intensity Noise
FDTD	Finite Difference Time Domain	SA	Spectrum Analyser
FVTD	Finite Volume Time Domain	SC	Short Circuit
ICM	Inverse Cylindrical Magnetron	SMA	Standard Military Adapter
IF	Intermediate Frequency	SOL	Short-Open-Load
LD	Laser Diode	SOLT	Short-Open-Load-Thru
LiNbO3	Lithium Niobate	TEM	Transverse Electromagnetic
MUT	Material Under Test	Ti:LiNbO3	Titanium-Diffused Lithium Niobate
NIST	National Institute of Standards and Technology	VCSEL	Vertical Cavity Surface Emitting Laser
OC	Open Circuit	VNA	Vector Network Analyser

Chapter 1

Introduction

In many fields apart from high frequency (HF) engineering, the accurate measurement of dielectric properties of materials is important. The flanged coaxial permittivity probe is a widely used technique for this purpose, due to its ease of use, accuracy and broadband operation. These probes measure reflected electromagnetic (EM) energy off a material under test (MUT), which is then converted into material properties via mathematical extraction.

A metrology study [1], performed on such a probe system at the national institute of standards and technology (NIST) in the United States, by H.C. Reader and M.D. Janezic, revealed the presence of unwanted CM-energy on the exterior of VNA feed cabling. This was associated with resonances seen in measured results and it became apparent that low levels of unaccounted energy escapes such systems. Further investigations revealed that the CM-effect induces cable-related resonances in extracted permittivity results.

This thesis presents an HF metrology study on this issue, with the emphasis placed on probing electric fields. The aim is to inspect the escaping energy by using a new experimental setup, to characterise its effect on material property results and to contribute to the future development of more accurate extraction algorithms that would take this lost energy into account.

1.1 Thesis layout

Chapter 2 presents a literature study on coaxial permittivity probes and optical E-field sensors, which represent two distinct, but coupled, parts of this work. Relevant aspects are covered for the coaxial probe that are referenced in later sections of this thesis. The chapter also explains the background of the CM-issue in detail and notes prior work that was done in attempts to characterise it. This sets the stage for the work presented here, which includes an attempt to develop an optical E-field sensor for making sensitive measurements around the coaxial probe.

In chapter 3, the design of such an optical E-field sensor, based on a Lithium Niobate (LiNbO₃), Mach-Zehnder-type, integrated optical circuit, is presented. An expedient design strategy is followed since the emphasis remains on the coaxial probe problem. Use is made

of published device parameters and specialised optical simulation software to design an optical waveguide and electrode structures. These elements are combined in the layout of a lithography mask which is required in the manufacturing process.

The attempted manufacture of this sensor is covered in chapter 4. Unfortunately, due to manufacturing difficulties with concomitant time constraints, the decision was made to discontinue fabrication. For possible future reference, the successfully completed fabrication steps are documented and solutions to specific problems are noted.

Attention reverts to the original CM-issue in chapter 5. Here, the extended centre conductor E-field probing technique, previously considered in [8], is applied in conjunction with CST to investigate external E-fields and CM-current. With CST modelling verified by carefully-conducted vector network analyser (VNA) measurements, the merit of different probe shielding-environments is studied exclusively in CST.

In chapter 6, the investigation is continued by studying the influence of CM-current on permittivity measurements. CST-supported, Short-Open-Load (SOL) calibrated, face-plane measurements of dielectric solids are considered. This allows the effect of the different shielding environments on permittivity results to be studied and finally, the consequence of escaping CM-current on the absolute accuracy of the probe is considered.

Chapter 7 concludes the thesis and places the findings into perspective. As a result future recommendations are made.

Chapter 2

Literature Study

This chapter serves as a literature study for two distinct aspects of this work and also introduces the reader to background developments that initiated it. Since the main focus concerns an issue in the measurement of permittivity with flanged coaxial permittivity probes, these probes comprise the first aspect that is considered. Starting out, a general discussion of permittivity measurement techniques, places the coaxial probe system into perspective. It is established as a subset of the transmission line class of methods and the basic concepts behind its operation is explained. A brief description of its application and the mechanism of its operation is then followed by a discussion of various developments that contributed to the improvement of these systems over the years. This paves the way for the introduction of the current system, a detailed explanation of the CM-current issue and a description of prior work that was done in pursuit of this issue. Through this, the need is explained to design and develop an optical E-field sensor for sensitive measurements around the coaxial probe, which marks the final aspect in this literature review. Various alternative sensor topologies are considered and finally an integrated optical sensor, based on a Mach-Zehnder interferometer is chosen.

2.1 Measuring Permittivity

Accurate permittivity measurements using radio frequency (RF) techniques can be traced back to the 1870's [9], where L. Boltzmann measured the real part of air's permittivity as 1.000590 for standard conditions of temperature and pressure. This value is still accepted today, some 130 years later. Up to the present, permittivity measurement techniques, stretching into the microwave regime, has expanded into various methods, each having different characteristics. Some are elementary, but lack accuracy, some are very accurate, but lack bandwidth, while still others require elaborate sample preparation. These methods can generally be subdivided into two main categories, namely: resonant and non-resonant. Resonant techniques [10] make use of structures where the inserted sample material influences the resonant behaviour. Non-resonant techniques employ other means, usually the measurement of reflected or transmitted EM-energy off-or-through a material sample. Table 2.1

below presents an elementary list of some popular permittivity measurement techniques and their characteristics.

Table 2.1: Comparison of popular permittivity measurement techniques

Method	Band	Sample Preparation	Accuracy	Application Example
Capacitive Plates	Lower Frequencies	Little	Good	PCB's
Resonator	Narrow Band	Required	Best	Solids and Liquids
Free Space	Higher Frequencies	Little	Good	Large, Flat Slabs
TX Line	Broadband and Lower Frequencies	Varies	Good	Geological Specimens

Despite the differences, all have one thing in common: permittivity cannot be measured directly, but has to be derived mathematically from measured data. This is normally from VNA scattering parameters (S-parameters). The conversion either uses an analytic solution for permittivity or a numeric solution of Maxwell's equations for the particular geometry, from which permittivity can be extracted. The general term for this process is material property extraction and will frequently be referred to in this document.

2.2 Coaxial Probe: A Transmission Line Method

The flanged coaxial permittivity probe is a subset of the transmission line class of techniques, listed in table 2.1. Use is made of the well-known impedance and loss characteristics of RF and Microwave transmission lines and how these parameters change with the addition of a material sample. The test sample is either placed within the transmission line, which is connected between two VNA ports, or it is placed bordering the end of a line for a one-port reflection measurement. Both rectangular and coaxial waveguides may be used in the prior sense. This usually requires thorough sample preparation since it is important that the sample fits snugly into the transmission line. For a coaxial waveguide, an annular-shaped sample is thus required. This is diagrammatically shown in Fig. 2.1 a). The advantage of the two-port technique is that both reflected and transmitted signals provide data for material property extraction, which specifically increases the measurement accuracy of loss parameters.

The second case, where the test material is situated at the end of a waveguide, is commonly referred to as reflection type measurements. Several forms of this type have been used and a few coaxial variants are shown in Fig. 2.1 b) - 2.1 f). With the exception of the

open-ended coaxial line, shown in 2.1 e), all other configurations require precise sample preparation. For this reason the open-ended probe provides considerable practical advantages. The sample material can virtually be any size or shape and only requires a suitably flat contact area to connect perpendicular to the probe end. This probe configuration is suitable for accurate broadband measurements of solid and liquid dielectric samples and is relatively easy to use.

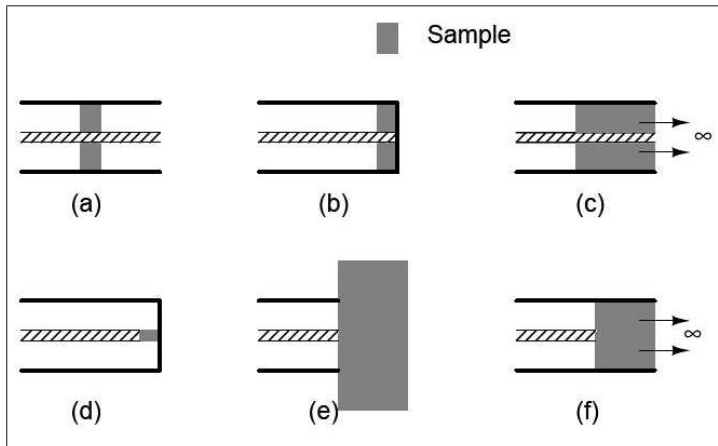


Figure 2.1: Coaxial Transmission Line Configurations for permittivity measurement from [2].

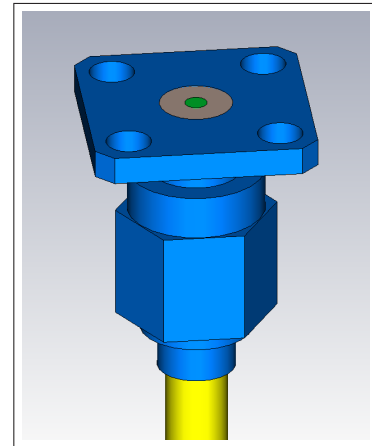


Figure 2.2: Open-ended SMA coaxial probe with panel-mount flange.

Most practical open-ended coaxial permittivity probes, including the one studied here, have an end-flange that extends the outer conductor radially to form a larger flat plane. This is shown in Fig. 2.2. It ensures that solid samples are accurately aligned to the probe end and also serves as a base to repeatably secure calibration standards. In addition, the flange plays a part in the accuracy of extraction algorithms that assume an infinite flange radius. Unflanged probes find use in more specialised applications such as *in vivo* permittivity measurements of biological tissue, where a flange would make insertion impractical. In [11] a more recent report on developments concerning this probe type can be found. Note that in the remainder of this thesis, the flanged, open-ended, coaxial permittivity probe that is used will in short be referred to as the coaxial probe, and the flanged case assumed.

2.3 Probe Measurement Procedure

In this investigation, only solid material samples are measured. Conducting permittivity measurements of solid materials using the coaxial probe requires four basic steps: 1) Preparation of the measurement setup; 2) Calibration to establish a reference at the face-plane; 3) Measurement of the material samples and; 4) Material property extraction. Preparation of the measurement setup includes entering all required parameters to setup the VNA, securing a physical jig which holds the coaxial probe, cleaning, connecting and torquing cabling,

cleaning measurement samples and calibration standards and monitoring room temperature for stability. Calibration establishes a VNA reference plane of zero phase and magnitude at the probe face. This requires three custom artefact calibration standards to be securely fitted in turn onto the probe face and measured. After such a calibration the probe is ready for sample measurement. Measurement entails placing a solid material sample onto the flange and initiating a new VNA sweep to record reflection data. Following this, use is made of an extraction algorithm to obtain complex material permittivity. The real part is ϵ' and the imaginary part is ϵ'' . Each of the four steps influences the accuracy of the measurement system and will be discussed in greater detail throughout this investigation.

2.4 Coaxial Probe Developments

To place the work of this investigation and its contribution into perspective, some background information regarding the development of the coaxial probe is relevant. Due to the practical advantages offered by the coaxial probe, many investigations and developments have contributed to its improvement. Usually these are spurred by some specific need that identify deficiencies in the current system. Common themes amongst these contributions are the development or improvement of calibration procedures, that of the physical probe design and enhancements in permittivity extraction techniques. The main objectives are to improve measurement accuracy, to simplify measurement procedure and to optimise the extraction of material permittivity.

2.4.1 Physical Probe Design

In practice, coaxial probes range from truncated lengths of standard coaxial cable to different sizes and shapes of custom designed probes, accurately manufactured from quality materials [12]. The sensitivity of coaxial probes is frequency and sample-permittivity dependent. A given probe dimension has an optimum frequency of sensitivity which reduces with diverging frequency. For samples of lower permittivity, a given probe size may, for instance, be used at higher frequencies and *vice versa*. This is coupled to capacitive effects of fringing E-fields and is discussed in more detail in [13].

Probes are used at frequencies below cut-off for higher order modes, which allow only the transverse electromagnetic (TEM) mode to propagate in the coaxial line. High quality probes frequently use air-line geometries but require an end-bead for structural integrity, and to avoid sample ingress. In this case the bead presents an impedance mismatch. Despite calibration, this results in residual errors that affect the sensitivity of such systems. As a solution, impedance-matching bead-geometries have been implemented [12], which require design principles similar to that used for matched beaded connectors. Probes with large flange radii approximate an infinite half-space geometry, which make computational models using analytical techniques feasible. The criteria for this assumption to be valid has been studied by various authors [11],[14]. Common consensus is reached that a factor of

about three times the outer conductor inner radius, for the flange radius, is acceptable. An investigation by [14] revealed that the effect of the thickness of the probe flange is negligible.

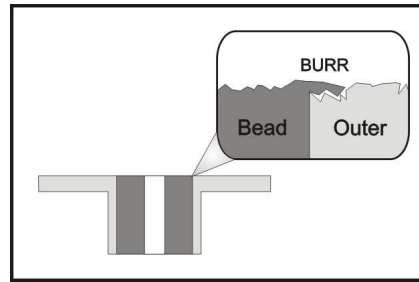


Figure 2.3: Probe showing bead burr extending over the outer conductor.

Effects of mechanical flaws in the probe aperture due to mechanical imperfections, handling and thermal expansion has been described by [15]. They used a 2D finite difference time domain (FDTD) computational code to simulate the probe face-plane geometry. It was found that small flaws, which cannot be perceived by the naked eye, can cause serious measurement errors. Special mention was made of the effect of slightly protruding or retracted bead material, as this was found to be the most common physical flaw. They report that such imperfections on the scale of 0.1 mm can cause errors as large as 25% at higher frequencies. Another source of mechanical flaw which they described was the presence of bead material burr, which slightly covered the inner or outer conductor. This flaw may result from stretching and pulling of the bead material during polishing procedures to flatten the probe face. This is illustrated in Fig: 2.3. For the measurement of non-malleable solid materials, air gaps between the probe face and MUT, also known as lift-off, are the primary source of measurement errors. This effect has been described by [1], [16], [13] and others.

2.4.2 Calibration procedure

Five possible calibration techniques for coaxial probe measurements are summarised in [16]. The recommended method entails using a reference liquid in conjunction with a short and open standard. The response for the reference liquid is predicted numerically from physical models. The open circuit is simply a measurement of the probe radiating into air with that response also numerically computed. The short circuit (SC) is obtained by pressing a metallic element of high conductance onto the probe face and a perfect SC-response definition of $-1+j0$ is assumed. The second method, which is used in this investigation, is a variation of the first, where the reference liquid is substituted by a mechanical load standard of known impedance. In [14], the third method is also proposed: The probe that is used must be very accurately characterised and connected to a pre-calibrated VNA. Numerical de-embedding is then applied during the measurement, through time-domain gating and normalisation, or afterwards to the recorded data. Another possibility is to substitute a removable flange with

a perfectly matched connector. This allows connection of artefact commercial standards, after which the flange is reconnected. The final method employs a two-stage process where, for instance, a standard calibration is first performed at the end of the VNA feed cable. The probe is then fitted to the cable and another measurement, usually with the probe radiating into air, is performed to correct for its electrical length and loss.

Most reported calibration refinements relate to the first and second methods described above. The use of a phase and temperature stable VNA cable is essential, since the value of extracted permittivity is sensitive to small changes in phase [1]. For this reason, physical disturbance of cabling is highly unwanted and warrants extensive mechanical support. A temperature-controlled room is recommended [13]. In [16], the repeatability of SC-standard connections are discussed. It was found that poor SC-connections are frequently the main cause of erroneous calibration. Accordingly a clamp mechanism, which applies pressure onto a thin pliable strip of polished copper foil that is placed on the probe face, was developed and tested successfully. In addition, an algorithm for least squares calibration was implemented which allows complex error-coefficients to be over determined and optimum values to be found. Other important considerations that are discussed in literature mainly apply to liquid-based calibration schemes and include aspects like liquid suitability, temperature, purity and the presence of air-bubbles on the probe face. These issues make liquid calibration less user-friendly.

2.4.3 Extraction Algorithms

Material property extraction algorithms fall into four major categories: 1) full-wave computational codes that considers Maxwell's equations for an assumed half-space geometry [13]; 2) methods that treat the probe as a radiating antenna into air and uses the Deschamps antenna theorem to relate a solution for the specific MUT [2]; 3) Circuit equivalent models that lump fringing field components into various capacitive elements [17], [18] and; 4) the use of standard computational codes to model the probe geometry and to simulate a material response. Since there is no closed-form solution for extracting permittivity, all of the methods either solve the problem numerically or assume a simplified model which can be solved directly. The full-wave algorithms are currently considered to be the most accurate[13], but they are more computationally demanding compared to methods such as circuit theory extraction. Traditionally the main problem associated with using full-wave solutions was the computational overhead, but with ever increasing computing power, this is no longer such a problem in most applications. The NIST full-wave algorithm, that is available to us, computes complex permittivity results from measured S-parameter data at discrete frequencies. It takes higher order modes that form at the probe-MUT interface into account and allows compensation for sample lift-off by definition of an air gap between the sample and the probe face. This algorithm also assumes an infinite half-space geometry which implies an infinite flange radius.

2.5 CM-Current Effects

A detailed metrology study [1], of a standard military adapter (SMA) type, coaxial probe system, conducted by H.C. Reader and M.D. Janezic at NIST, resulted in the discovery that low levels of CM-current exist on measurement cabling and can result in small perturbations in measured data. In their investigation they placed an electromagnetic compatibility (EMC) current-probe, connected to a hand-held, battery-driven spectrum analyser (SA) around VNA feed cabling and detected low levels of CM-current on the outside of the probe and feed cable. This was seen across the measured band. Further investigation revealed that these low levels of CM-current were even present on the VNA power chord. As a result, a small, reoccurring perturbation in their measured data sets at 200 MHz was associated with reflections of CM-energy on the specific cable length between the probe face and VNA test port. This proved that low levels of CM-current on the outside of the probe can significantly influence the accuracy of measured permittivity and that arbitrary cable lengths would make the occurrence of these effects unpredictable.

With the CM-issue discovered, it needed to be characterised to better understand it on a field level and to gauge the extent of its influence on permittivity measurements. In an initial study, conducted by J. Badenhorst [8], the current-probe theme was expanded in an attempt to directly measure CM-currents on the coaxial probe. Despite extended efforts in calibration, it was found that such a current probes lacked the necessary dynamic range to detect these small values in any detail. A new method was needed that could provide greater dynamic range. With the idea of isolating feed cabling from CM-current on the outside of the probe, a metallic shielding cylinder was placed around the probe structure. This is shown later in Fig. 5.1 of Chapter 5. It then became apparent that E-fields, associated with this CM-current, would be confined inside this cavity and that it could possibly be measured as an indirect way to determine CM-current levels. Emphasis thus shifted to measuring sensitive electric fields within the cavity.

J. Badenhorst started experimentation with a probing technique described in [19], that uses an extended centre-conductor coaxial cable as an E-field probe. A second VNA-port is connected to such a probe, which is inserted through a small side-hole in the shielding cylinder, at a predetermined position. The extended centre-conductor protrudes slightly into the cavity and serves as an E-field pickup. After diligent characterisation of such a field probe it would be possible to relate E-fields to S21 measurements. The problem with this, or any other available E-field probing techniques that employs metallic elements, is the issue of field perturbation. As an alternative method to avoid this problem, J. Badenhorst attempted to use the probing technique purely as a method to validate a CST computational model. This could then directly report on field and current levels for the case with no field probes present.

Despite the promise of this method, the simulated and measured results did not match within acceptable levels to validate the CST model. Consequently, the need still existed for a small, sensitive, non-perturbing E-field probe that could be used to measure anywhere

within the shield cavity. This spurred an interest in optical E-field probes and resulted in the design and attempted manufacture of such a probe in this work.

2.6 Optical E-field Sensors

The idea of using optically based sensors for sensitive E-field measurements has been reported since the 1980's [20], and have since seen more discrete development, mostly for in-house company use or military applications [4]. The merit in using optical means lies in the fact that it supports the use of sensitive, all-dielectric sensing elements, which avoid large field perturbations. Since fibre-optic connections are used, these sensing elements are electrically isolated from measurement equipment and can be used in harsh electromagnetic environments. Modern optical E-field sensors provide attractive sensitivity and spatial resolution and make use of advances in nano-technology and material science. Unfortunately these specialised sensors have only recently become commercialised and are still expensive. Therefore, the option of manufacturing a lower cost in-house sensor is investigated. Various methods for manufacturing optical E-field sensors have been published. Devices are either active or passive in nature. Active devices use make use of electrically or optically biased laser diodes which provide E-field-modulated output light intensity via fibre-optic cable. Passive sensors are based on specific materials which exhibit one of a variety of useful EO-effects that alters the way in which light propagates through that material. In consideration of building such a device, the advantages and disadvantages of the various methods must be weighed up. A thorough review of developments can be found in [3].

2.6.1 Vertical Cavity Surface Emitting Laser Sensor

In [21], an active optical E-field sensor, based on a vertical-cavity surface-emitting laser (VCSEL), is reported. The laser is modulated via a small antenna by the surrounding E-field and transmits these optical signals via fibre-optic to a remote monitoring unit. The usual drawback of these devices are field perturbations caused by electrical wires that are required to provide a bias-current. The reported implementation negates this problem by optically transmitting a bias signal via another fibre-optic cable, connected to a solar-cell array. Sensitivity of $50\mu\text{V}/\text{m}\sqrt{\text{Hz}}$ is reported at 100 MHz and a Dynamic range of 130 dB was achieved. Dominant noise in the system is attributed to random intensity noise (RIN) of the VCSEL. Despite the fact that this system is both small and sensitive, the device needs two fibre-optic systems, which makes it expensive. In addition the integrated dipole antenna still presents a small but present metallic element in the system.

2.6.2 Fibre-Optic Based Sensors

In fibre-optic based E-field sensors the fibre optic is used as a sensing element. A combined EO-effect is created by making physical alterations to the fibre and adding some materials. This usually results in intensity-modulated light output as a function of the measured

E-field. One method [3], entails covering an exposed section of multimode fibre-optic core with polymer-dispersed liquid crystals (PDLC), which is a mixture of a polymer and liquid crystals. This is shown in Fig. 2.4. Due to the dispersed liquid crystals, the synthetic material has the property of becoming more transparent with increasing electric field intensity. The evanescent modes which propagates in the fibre cladding is affected by this change in refractive index and results in output intensity variations due to the surrounding E-field. A liquid solution of another synthetic compound, $\text{Fe}_4[\text{Fe}(\text{CN})_6]_3$, dissolved in water and surrounding a similar exposed-core fibre-optic configuration, has also been reported as a possible sensing element. Despite the apparent ease of manufacture, these types of optical sensors are reported to have low sensitivity and long response times which does not make it suitable for HF-measurements. In [4] an in-fibre E-field sensor is presented that makes use of a D-type optical fibre. The core of the fibre is microscopically etched using a chemical method and an EO-polymer material is spun into the cavity. The polymer is polled in the required orientation using an intense electric field. It then serves as an optical sensing element which alters light-propagation in the fibre-optic cable. Fig. 2.5 shows a picture of such a fibre sensor, placed on a printed circuit board (PCB) for measurements near electronic components. This sensor avoids sensitive fibre-to-device coupling but requires highly specialised equipment and practical expertise to manufacture.

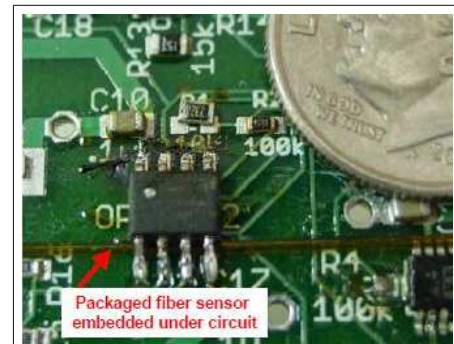
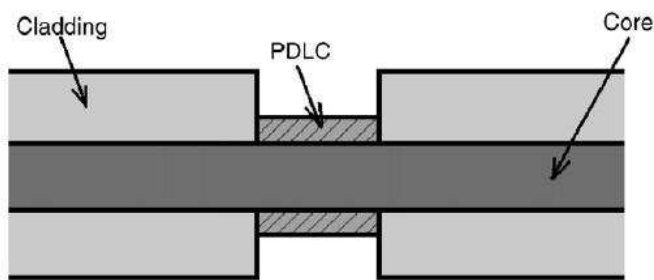


Figure 2.4: Exposed-core multimode fibre with PDLC coating form [3].

Figure 2.5: D-fibre sensor embedded under electronic circuit components from [4].

2.6.3 Integrated Optic E-field Sensors

Integrated optical E-field sensors make use of the optical equivalent of electrical integrated circuits. Optical waveguide paths and other functional elements are designed and fabricated in or on top of a suitable optical substrate instead of electrical paths. These lead to fibre-coupled ports which serve as inputs and outputs of the optical circuit. Most integrated optical E-field sensors make use of the basic Mach-Zehnder interferometer structure, illustrated in Fig. 2.6. It is used in a multitude of EO-devices and exploits the EO-effect of the waveguide material through interferometry, to provide modulated light output intensity as

a function of the applied electric field. A more detailed description of its operation is given in section 3.2.

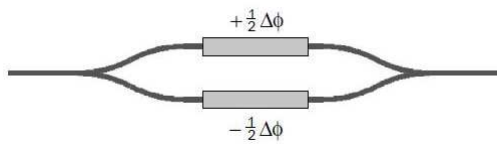


Figure 2.6: Mach-Zehnder interferometer structure from[5].

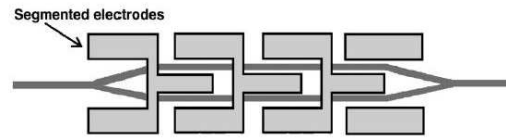


Figure 2.7: E-field sensor with segmented electrodes from[3].

In [22] an optical E-field sensor is successfully developed that makes use of a standard fibre-optic telecommunications modulator. These complex modulators are based on integrated Mach-Zehnder interferometer waveguide structures, fabricated by means of Titanium diffusion into LiNBO3 crystal. This material exhibits EO-properties which forms the core of the device. Micro-structured electrodes, represented by the two blocks in Fig. 2.6, are used to apply electrical data-signals, which cause amplitude-modulated output light signals on coupled telecommunications fibre for digital communication. For the sensor application, the electrical input is connected to a relatively small external disccone antenna which results in amplitude modulation as a function of the measured electric field. Input light is provided by a fibre-coupled laser diode and output power is measured with a fibre-coupled photodiode. The system is sensitive up to 0.1 mV/m and a dynamic range of 100 dB is achievable. The measurement band is limited by the antenna, but by using two separate antennas, the band stretches from 50 MHz to 18 GHz. The use of standard components make this sensor attractive, but to avoid electrical biasing the modulator must be passively biased at its quadrature point for small signal operation. This is difficult to obtain from manufacturers since it requires screening of the optical chips at the production line. These modulators are sealed in metallic enclosures, the sensor requires a metallic antenna and apart from the high cost of such modulators, the system is relatively bulky.

Fabrication of customised integrated optical E-field sensors based on LiNBO3 modulator technology was first reported in [20]. The Mach-Zehnder interferometer is designed to be passively biased at quadrature by making the Mach-Zehnder arms slightly asymmetric with a path length difference of a quarter optical wavelength. Since the sensitivity of the sensor is directly related to the interaction length between the measured electric field and the Mach-Zehnder arms, the sensor can be made longer for enhanced sensitivity. Early designs still make use of an external antenna, but the overall size of the system is much reduced. A sensitivity of up to 1.1 μ V (detection bandwidth of 3 kHz) for an applied voltage on the electrodes is reported and a dynamic range of 84 dB is achieved. Fabrication makes use of standard semiconductor methods and is described in detail.

In [23] an improved sensor, based on the same technology, is fabricated and tested. The usually external antenna is combined into an integrated, segmented electrode structure on

top of the Mach-Zehnder waveguide channels which is diffused into the LiNbO₃ substrate below. This is shown in Fig. 2.7, and allows total sensor size to achieve proportions of 30 mm × 3 mm × 2 mm. The frequency response of the device is reported to be flat up to 3 GHz and a peak sensitivity of 1 mV/m is achieved at a measurement bandwidth of 1 Hz. Thermal stability of the E-field probe is achieved by using indium tin oxide for electrodes and applying an additional layer of amorphous silicone on top. A sensor based on exactly the same design and fabrication process has been successfully implemented and reported in [24]. A further improvement which entails the use of a balanced detection scheme to reduce the limiting effect of laser diode noise in these systems have been proposed in [25]. More modern equivalents of these sensors, based on poled EO-polymers are described in, [4] and [3], but require access to advanced materials and sophisticated manufacturing techniques.

Of all the considered methods, integrated optical E-field sensors based on LiNbO₃ seems to be the best choice for an in-house fabricated sensor. The successfully tested sensors described in literature are sensitive, small and are fully dielectric apart from the metallic thin-film electrodes which will cause minimal field perturbations. This makes such a sensor ideal for the investigation of E-fields inside the shielded cavity of the coaxial probe. The extended range of LiNbO₃ applications, which include optical communication modulators and surface acoustic wave filters, make the technology widely established and properly documented.

2.7 Conclusion

In this literature study the flanged coaxial permittivity probe was introduced and such systems were placed into perspective. The general procedure, used to conduct permittivity measurements of solid materials, was presented and several aspects in the development of these systems were discussed. Thereafter, the background of the CM-issue and its significance was explained in detail. This established the motivation for this work and as a consequence, the need was identified to develop an optical E-field sensor to characterise sensitive fields around the coaxial probe. Several possible systems were identified and a LiNbO₃-based integrated optical sensor was chosen to be designed and manufactured. The design of this sensor follows in the next chapter.

Chapter 3

Mach-Zehnder Design and Simulation

This chapter documents the theory, design, simulation and mask layout of a LiNbO₃-based, Mach-Zehnder type optical waveguide interferometer with metallic electrodes. It forms the core sensing element for an optical E-field sensor. The aim is to use this sensor to probe sensitive electric fields around the coaxial probe with minimal field perturbation.

First the EO-effect in LiNbO₃ and the basic operating principle of a Mach-Zehnder interferometer is introduced. Thereafter the formation of optical waveguides in LiNbO₃, through thermal Titanium diffusion is explained. This flows into a description of general considerations and the introduction of the Mach-Zehnder waveguide parameters. The following subsections cover the waveguide design and includes the use of C2V simulation software, in which the final Mach-Zehnder is simulated. Focus then shifts to the layout of the top electrodes: one for device testing and the other for field measurements. This concludes the design phase of the sensor. Thereafter, the use of a mask layout tool in the same software suit, as well as practical considerations for the final mask layout, is discussed. A detailed description of the components that make up the whole sensing system is given, and finally, a device test strategy is introduced.

3.1 Linear Electro-Optic Effect in LiNbO₃ Crystal

To explain the detailed working of a Mach-Zehnder interferometer, based on Titanium-diffused Lithium Niobate (Ti:LiNbO₃), the EO properties of LiNbO₃ crystal must be introduced. LiNbO₃ is a widely used synthetic crystal that contains Niobium, Lithium, and Oxygen, bound in a trigonal crystal lattice which lacks inversion symmetry. It exhibits numerous advantageous optical properties such as Ferroelectricity, the Pockels effect, Piezoelectric effects, Photoelasticity and others. Of primary interest for application in optical modulators, using the Mach-Zehnder waveguide architecture, is the Pockels effect. This was first studied and documented by F.Pockels in 1893, [26], and describes the ability of certain optical materials to alter their refractive index in linear proportion to an applied electric field. LiNbO₃ is one of a limited number of photonic crystals that possess this trait and exhibits large EO-coefficients. When an E-field is applied, the charge distribution within the crystal lattice

changes and even the structure of the lattice might undergo slight distortion. The following equations are taken from [26]. The charge distribution inside the crystal is related to its optical impermeability tensor, defined as:

$$\Delta\eta = \frac{\epsilon_0}{\epsilon} \quad (3.1)$$

where ϵ is the dielectric tensor. The EO-effect is mathematically described by

$$\Delta\eta_{ij} = \eta(\mathbf{E}) - \eta(\mathbf{0}) \equiv \Delta\left(\frac{1}{n^2}\right)_{ij} \equiv r_{ij}E_k \quad (3.2)$$

where \mathbf{E} is the applied electric field, E_k is the k component ($k = x, y, z$) of the electric field, and the summation over repeated indices is assumed. Higher order terms are ignored in equation 3.2 and the r_{ij} constants are the linear EO-coefficients of the crystal. For LiNbO3 this is given by

$$r_{ij} = \begin{bmatrix} 0 & 5.4 & 9.6 \\ 0 & 5.4 & 9.6 \\ 0 & 0 & 30.9 \\ 0 & 32.6 & 0 \\ 32.6 & 0 & 0 \\ -3.1 & 0 & 0 \end{bmatrix} \quad (3.3)$$

For Mach-Zehnder interferometer waveguide devices, based on LiNbO3, specific use is made of the high r_{33} EO-coefficient, which is aligned with the Z-axis of the crystal. The EO-effect is also active in the X and Y-axis of the crystal but is smaller and less useful.

3.2 Mach-Zehnder Theory

With the EO-effect in LiNbO3 described, the working of a Mach-Zehnder interferometer, which exploits this effect, can be introduced. In Fig. 3.1 a) and Fig. 3.1 b), two top-view illustrations explain its basic operating principle. In both cases, continuous light, entering the waveguide on the left, is represented by an optical wave. The wave propagates down the channel and a 3 dB split occurs at the first Y-branch. The two resulting wavelets propagate down the arms of the interferometer until they reach the straight sections where pairs of electrodes straddle the waveguides. At this point the waves in Fig. 3.1 a) and Fig. 3.1 b) are the same. In the case of Fig. 3.1 a), no voltage is applied across the electrodes and hence no electric fields cut through the Ti:LiNbO3 channels. The two waves propagate at the same velocity and combine in phase at the output Y-branch. In contrast, for Fig. 3.1 b), two equal but opposite voltages are applied across the upper and lower electrode pairs. The EO-effect in LiNbO3 causes one channel to have a slightly lower refractive index and the other a slightly higher index. As a result, the two waves propagate at different velocities and combine with a phase difference which is proportional to the applied electrode voltages.

The output of the Mach-Zehnder interferometer thus provides modulated light intensity as a function of the electrode voltages. In the case of Fig. 3.1 b), the applied voltages causes total phase cancellation. This distorts the output light-wave to the extent that it cannot be guided by the optical channel. Most energy departs the system in the form of scattered light, leaving little to exit the output channel. LiNbO₃-based, fibre-optic communication modulators use the two extreme cases, described here, to form 1's and 0's respectively. For the E-field sensor, an integrated electrode configuration, introduced in section 3.6, allows exterior E-fields to produce the potentials between the electrode gaps. The linear, small-signal change in output light-intensity is then used as a measure of the external E-field.

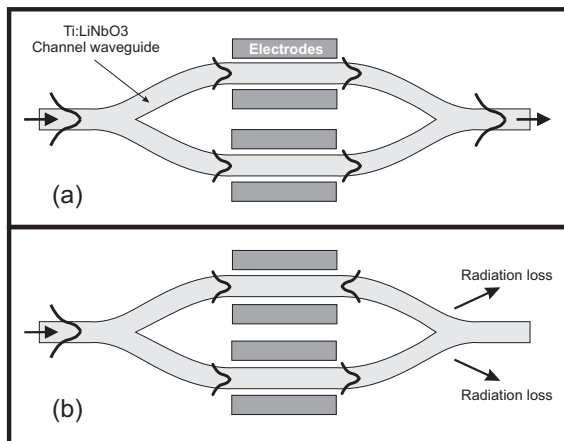


Figure 3.1: Basic Mach-Zehnder operation: a) Zero voltage across electrodes: output is in-phase and b) Voltage applied: output phase-cancellation.

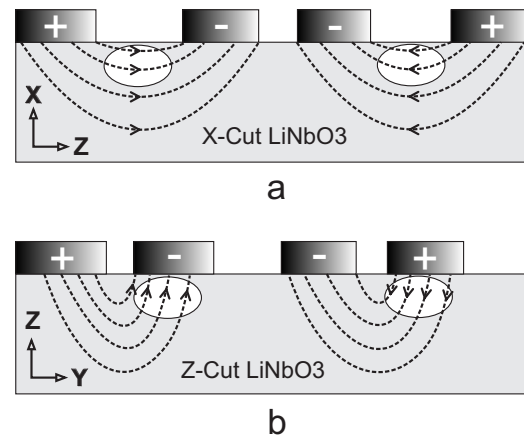


Figure 3.2: Electrode configurations for two LiNbO₃ crystal cuts: a) X-cut: horizontal field and; b) Z-cut: vertical field.

In Fig.3.2 a) and Fig. 3.2 b) cross-sections of the Mach-Zehnder interferometer, based on two different LiNbO₃ crystal cuts are given. The white, oval sections are the Titanium-diffused optical waveguide channels of the Mach-Zehnder, which lies just below the surface of the bulk LiNbO₃ substrate. The dark structures on top are the metallic, thin-film electrodes. The cross-sections are taken at the straight-arm section of the Mach-Zehnder. As described in section 3.1, use is made of the large EO-coefficient of LiNbO₃ which is aligned to the crystal's Z-axis. Depending on the cut of the crystal, this axis is either horizontally aligned, Fig. 3.2 a) for an X-cut crystal, or vertically aligned, 3.2 b) for a Z-cut crystal. In accordance, different electrode layouts, situated on top of the LiNbO₃ substrate, are used to orient E-fields in the Z direction. For the X-cut case, electrodes are spaced adjacent to each Ti:LiNbO₃ channel, which aligns E-fields horizontally through it. For the Z-cut case, electrodes are spaced to align E-fields vertically through the channels. Since the Z-cut electrodes lie directly above the waveguide, an optical buffer layer, eg SiO₂, is required to prevent scattering-loss. From the diagrams it is evident that the electrode spacing and the effective fields, cutting the Ti:LiNbO₃ waveguide sections, are of interest. Smaller electrode spacings are desired for increased field strength and proper electrode placement, relative to the

waveguide channels, is required to ensure maximum field coupling. Both factors influence the sensitivity of the sensor.

The transfer function of a Ti:LiNbO₃-based, Mach-Zehnder interferometer is widely published [20], [26], [25] and is given by:

$$T = \frac{1}{2} \left[1 + \cos\left(\Gamma_0 + \frac{\pi}{V_\pi} v_m\right) \right] \quad (3.4)$$

where Γ_0 is the intrinsic interferometer phase bias, and V_π is the half-wave voltage required to drive the modulator into full destructive interference, as in Fig.3.2 b). The transfer function is dependant on the electrode voltage, v_m , with its cosine form, depicted in Fig. 3.3.

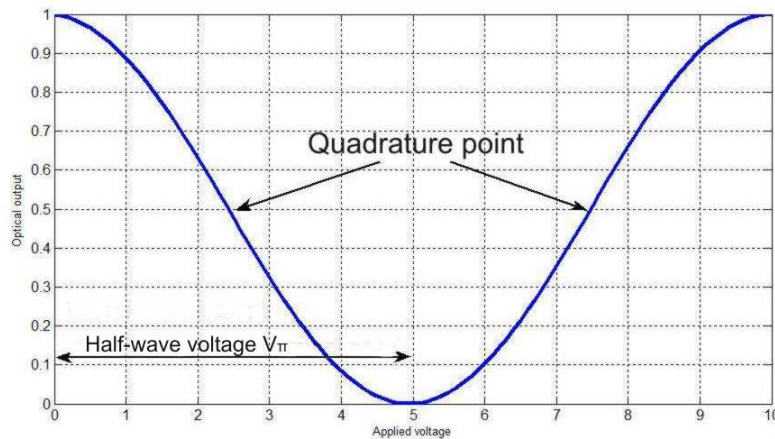


Figure 3.3: Mach-Zehnder transfer-function.

For small signal operation, $V_m \ll V_\pi$, and the Mach-Zehnder must be passively biased at the linear regions, surrounding one of the quadrature points, for maximum sensitivity. This is normally achieved by designing the interferometer arms to be slightly asymmetric with an effective path-length difference of $\lambda/4$, giving $\Gamma_0 = \frac{V_\pi}{2}$. The small signal transfer function is then given by:

$$T(v_m) = \frac{1}{2} \left[1 - \sin\left(\frac{\pi}{V_\pi} v_m\right) \right] \quad (3.5)$$

The half-wave voltage, incorporating the EO-effect in LiNbO₃ is given by

$$V_\pi = \frac{\lambda g}{2\delta n_e^3 r_{33} L} \quad (3.6)$$

where δ is the electrode efficiency, which is a measure of the electrode field coupling with the waveguide channels, and n_e is the extraordinary refractive index of LiNbO₃. The electrode length and gap-width between them are given by L and g respectively and the EO-coefficient is given by r_{33} .

3.3 Titanium Diffusion in LiNbO₃

Thermal diffusion of Titanium thin-film structures on LiNbO₃ are used to fabricate optical waveguide channels just below the surface. The Mach-Zehnder structure for the sensor is just one example of such an application. Under specific processing conditions the patterned LiNbO₃ substrate is heated in a furnace over an extended period. The Titanium particles migrate into the LiNbO₃ crystal lattice and cause a localised change in the bulk optical refractive index. The degree of this change is dependent on the concentration of Titanium particles in the diffusion area. For carefully chosen diffusion parameters, which include temperature, duration, initial Titanium strip width and film thickness, an elliptical distribution of Titanium particles with a peak central concentration can be formed. This two-dimensional profile, (in cross-section), supports the transmission of optical waves, and are usually designed for single-mode propagation. Fig. 3.4 shows a C2V simulation result of the localised change in optical refractive index for a diffused Titanium strip. The lower graphic is a three-dimensional plot of the two-dimensional refractive index distribution, shown at the top. Concentration of the refractive index in the centre is evident.

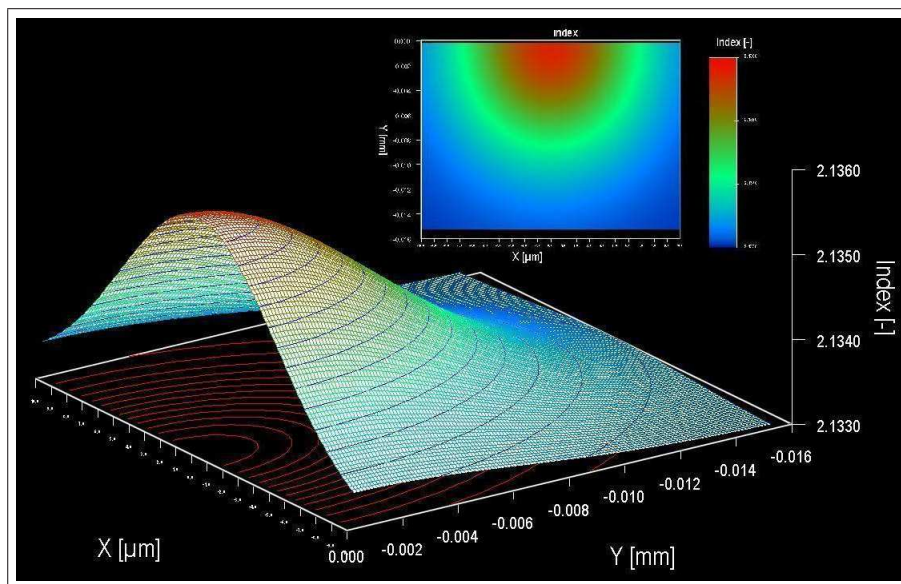


Figure 3.4: Change in local refractive index after Titanium diffusion in LiNbO₃.

Since the 1980's, various articles on Titanium diffusion in LiNbO₃ have been published, including [27], [28] and [29]. The research was particularly driven by the development of LiNbO₃-based communication modulators. A few key features relating to Ti:LiNbO₃ profiles of are worth noting: 1) The source of the diffused particles is actually TiO₂, which is formed through of the interaction of Ti with LiNbO or LiNb₃O₈ at high temperatures; 2) Mode-confinement, which influences propagation loss, is dependant on the difference in refractive index between the guiding region and the bulk substrate ($\Delta n = n_g - n_s$); 3) Good dimensional mode matching between fibre and waveguide channels substantially reduce

coupling loss and; 4) Non-diffused TiO_2 film on the substrate surface increases scattering loss. These issues become important in the design stage of the E-field sensor which follows.

3.4 Design Considerations

In keeping with the chief objective of developing a practical sensor for E-field measurements around the coaxial probe, an expedient design strategy is followed. Well-documented parameters for device fabrication are used, which in some reported cases, differ from optimal theoretical values. A trial version of an optics simulation package, from Concept to Volume (C2V), allows an iterative design strategy to be followed. The aim is to create a photolithography mask layout in GDS2 file-format which can be sent to a mask manufacturer. The sensor design can be split into two main parts: that of the Mach-Zehnder waveguide and that of the electrode structure on top. Each has functional aspects to consider.

An important issue is the fabrication limits imposed by the available laboratory equipment. To appreciate these limits, an initial period was spent in the semiconductor laboratory to learn the chief processing steps. These hours proved to be well-worthwhile since several fabrication issues, that influenced the final designs, were discovered. The size of the LiNbO_3 substrate (and thus the maximum sensor length and related sensitivity) is limited to a maximum of 20 mm \times 20 mm, due to the uniform coating area of the thin-film sputter coater. The minimum spacing between the top electrodes is constrained by the achievable lithography resolution and the accuracy of optical mask re-alignment. The length of the straight sections on either end of the Mach Zehnder are made longer. This is to accommodate shortening of the substrate due to optical end-face polishing and for ease in solving problems with lithography edge-bead. The savings in time and cost through such foresight highlights the value of practical experience in any design process.

3.5 Mach-Zehnder Waveguide Design

The Mach-Zehnder's seemingly elementary shape can be deceiving. An initial design approach involved using a series of straight lines to form simple Y-structures, as described in [20]. When the C2V package was sourced to ease the laborious process of manual mask layout, it was noted that standard Mach-Zehnder shapes make use of S-shaped arms. Further investigation revealed a more extended set of published design considerations and now the key diffusion issues mentioned at the end of section 3.3 come into play. An efficient, wavelength-specific design, entails choosing suitable dimensional and diffusion parameters to optimise a trade-off between mode confinement and mean-mode size. By increasing the diffusion temperature and duration, Titanium particles diffuse-in more which result in a greater mode size but weaker concentration (mode confinement). By making the initial Titanium film thicker, confinement is improved, but mode size is reduced. Varying the initial Titanium strip width results in weaker mode confinement and increased mode size for

smaller widths and for larger widths, *vice versa*.

It could be argued that an effective solution would be to use a thin initial strip width and large film thickness and to choose a high temperature and a short diffusion time, but practical limitations exist. It is important that all the initial Titanium on surface of the LiNbO₃ diffuse in properly to avoid induced scattering loss. Furthermore, thermal diffusion is an active process in which the Titanium is oxidised and changes in shape and structure. This means a thick and very narrow strip might simply spread out during the process. The diffusion temperature is also limited by the Curie temperature of LiNbO₃ (1140°C) where structural degradation sets in. Fortunately these parameters have been the subject of many published investigations, including [28], [29] and [30], which make finding suitable values easier.

3.5.1 Crystal Cut and Wavelength

Of the two crystal cuts presented in section 3.2, the Z-cut is chosen. The reason is that a slightly larger change in refractive index results from Titanium diffusion in this orientation. The disadvantage of a Z-cut device is that it requires an optically transparent buffer-layer below the electrodes, as explained in section 3.2. Before any design parameters can be finalised, the device's optical wavelength has to be chosen. Since different wavelengths require different mode sizes for single-mode propagation, the choice of wavelength directly influences the dimensional and diffusion parameters of the waveguide. Earlier work on such sensors focused on shorter available wavelengths such as 610 nm and 835 nm. This resulted in problems due to optical damage in LiNbO₃ which has a stated threshold of 200 mW/cm². With the widespread use of the 1.310 μm wavelength in telecommunications, later work on E-field sensors settled on this wavelength. Making use of a standard wavelength also has the advantage of lower component cost and availability. The wavelength for this sensor is chosen not only for these reasons but also due to the fact that optimised LiNbO₃ diffusion parameters are published for the 1.310 μm wavelength.

3.5.2 Initial Titanium Strip Width

Due to different laboratory conditions and the number of diffusion variables, various optimum diffusion parameters have been published by authors. Despite these differences it becomes apparent that a well-informed choice of parameters, executed within certain limits, would result in a workable waveguide. In literature, initial Titanium waveguide strips range from about 4 μm to 10 μm wide. Thermal diffusion takes place between 900 and 1050 °C for 6 to 12 hours and initial Titanium film thicknesses vary between 300 to 1000 Angstrom. For this sensor, an initial strip-width of 6 μm is chosen as a starting point for determining the other diffusion parameters. This value is more common amongst published parameters and supports good mode confinement. This size also represents the minimum acceptable size for in-house fabrication. The Mach-Zehnder structure has a large length-to-width aspect ratio (20000:6), which makes the structure fragile to photolithography processing. The final

physical and diffusion parameters are subject to the design of the waveguide bends of the Mach-Zehnder.

3.5.3 Waveguide Bends

In optical integrated circuits with multiple separating waveguide branches for fibre coupling, the obtainable density of the circuit depends to a large extent on the transition length which can be tolerated for acceptable bend losses. In the case of this sensor, a similar limitation exists. The bend transition of the input and output Y-branches occupies valuable space on the LiNbO₃ substrate, limiting the straight-arm interaction length. Ideally, the length of the Y-branches should be minimised while maintaining acceptable bend losses. So, apart from fibre-to-guide mode-matching and mode-confinement, this is a further requirement for a good waveguide design. In [28], Ti:LiNbO₃ waveguide bend-loss is studied for the 1.310 μm wavelength and the results are useful.

In their investigation, bend-loss is determined as a function of: 1) bend length with a fixed horizontal offset; 2) mode-confinement, by varying initial Titanium film thickness and; 3) the dependence on bend shape. For their bends, use was made of an optimised S-shaped curve, based on a Sine function given by:

$$y(x) = \frac{h}{l}x - \frac{h}{2\pi} \sin\left(\frac{2\pi}{l}x\right) \quad (3.7)$$

where the curve k , given by:

$$k = \frac{2\pi h}{l^2} \sin\left(\frac{2\pi x}{l}\right) \quad (3.8)$$

is an approximation used to analytically solve an integral equation for bend-loss. In these equations, h is the horizontal bend offset length and l is the bend transition length. Through de-convolution of a bend-loss function for slab waveguides and empirical data-fitting to obtain the necessary constants, an integral solution, applicable to Ti:LiNbO₃ waveguide bends of the stated curve function, was derived and is given by:

$$\alpha(\text{dB}) \approx \frac{10}{\ln 10} 2\sqrt{2}\pi \frac{h}{l} \frac{C_1}{C_2} e^{-\gamma} \left[1 - e^{-\gamma/2}\right] \quad (3.9)$$

with

$$\gamma = \frac{C_2 l^2}{2\pi h} \quad (3.10)$$

The constants C_1 and C_2 are functions of the guiding characteristics of the waveguide. C_1 is strongly diffusion-model dependant and C_2 is an increasing function of Δn , and thus mode confinement. It is reported that transition curves without discontinuities in the first and second derivatives are desirable. From Fig. 3.5, valuable insight concerning Ti:LiNbO₃ waveguide bend-loss can be gleaned. The graph shows three curves generated by equation 3.9. The X-axis indicates bend transition length in mm and the logarithmically scaled

Y-axis states the predicted bend loss in dB. The horizontal bend offset is kept constant at $27\mu\text{m}$, which is the larger offset of the final, asymmetric Mach-Zehnder layout. The bend offsets determine the mid-channel separation and must accommodate the top electrode design. Each plot corresponds to a different level of mode-confinement, indicated by the initial Titanium film thickness in Angstrom. The guide mean-mode size for each curve is also stated. As expected, bend-loss is minimised for longer transition lengths and increasing mode-confinement, while the mean-mode size increases for decreasing mode-confinement. The remaining part of the investigation reveals that bend-loss is not particularly sensitive to small perturbations in waveguide shape.

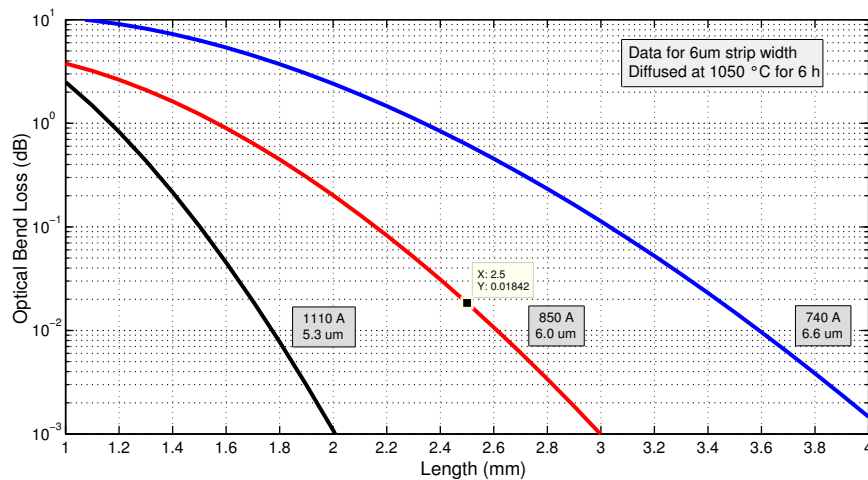


Figure 3.5: Calculated optical bend-loss in dB vs bend length for a fixed $27\mu\text{m}$ horizontal bend-offset. Three cases of initial Titanium film thickness, given in Angstrom are plotted. Constant diffusion parameters are stated above.

With this information, the final Mach-Zehnder diffusion conditions can be chosen with confidence. By choosing an initial film thickness of 850 \AA and tolerating a bend offset length of 2.5 mm on either side, the maximum approximate bend-loss can be limited to 0.018 dB . This requires a diffusion temperature of $1050\text{ }^\circ\text{C}$ for a duration of 6 hrs . These parameters strike an acceptable balance between mode-confinement and mean-mode size.

A C2V design-view of the chosen Mach-Zehnder bend-curve can be seen in Fig. 3.6. For clarity, the width-to-length aspect ratio is adjusted to ease the design process. In real proportions the curved bends are gradual and hardly noticeable. Multiple use is made of overlapping "Sin-bend" elements in the standard design-suite library to construct the Mach-Zehnder shape. Although the mathematical function of this curve is not published in C2V documentation, the shape is similar to that used in the investigation. The theoretical bend-loss results are thus assumed to be applicable. The central, yellow region represents the initial $6\mu\text{m}$ -wide Titanium strip prior to diffusion. The red region indicates a simulation boundary for implementing the diffusion conditions in simulations. With the basic bend-shape, transition length, horizontal offset and diffusion parameters obtained, the asymmetry

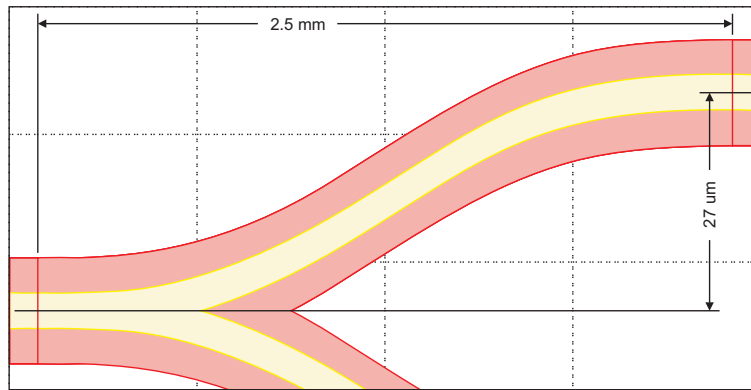


Figure 3.6: C2V design-view of Mach-Zehnder waveguide bend-curves. Shown with adapted width-to-length aspect ratio.

in the Y-structures, needed to passively bias the device at quadrature, can be determined. This is achieved through an iterative simulation process in the C2V OlympIOs design suite.

3.5.4 C2V Iterative Design

The C2V OlympIOs suite is an optical, multi-physics Micro-Electro-Mechanical-Systems (MEMS) specific package with an array of solvers for thermodynamic, mechanical stress, static E-field and optical wave-propagation problems. For the waveguide asymmetry design, use is made of its 2D-BPM solver which simulates optical wave-propagation in devices by means of the finite difference beam propagation method (FD-BPM). More information about the solver can be obtained in the C2V product documentation [31], which also contains LiNbO₃-specific application examples. Use is made of [32] and [33], regarding the simulation of Ti:LiNbO₃ waveguide profiles.

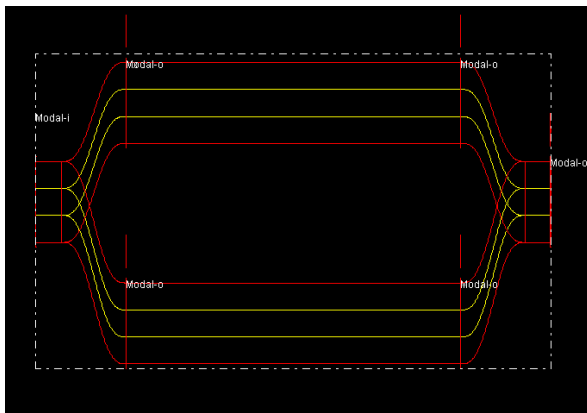


Figure 3.7: Complete Mach-Zehnder design with asymmetric waveguide bends.

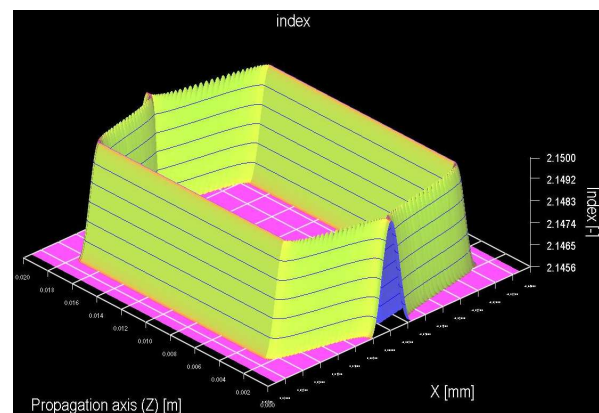


Figure 3.8: 3D-view of 1D effective index profile after Titanium diffusion.

Starting out, a symmetric Mach-Zehnder with the Sin-bends, shown in of Fig. 3.6, is parametrically implemented in the top view editor. This looks similar to the final asymmet-

ric layout, shown in Fig. 3.7. Separate variables are used for the top and bottom bend-offset with initial value of $19\mu\text{m}$. At the left input of the guide an optical simulation source is specified and at the start of the two straight sections, Modal-Overlap monitoring elements are defined. At the end of the waveguide on the far right a final Modal-Overlap element is added to capture the output. User-defined diffusion parameters are specified in a separate text file that is used for the simulation. When the simulation starts, OlympIOs calculates the 2D refractive index profile of the Ti:LiNbO₃ waveguide by using the specified diffusion parameters in the text file. It then converts this into an effective one-dimensional index profile, shown in Fig. 3.8. The 2D optical solver uses this information to compute optical wave propagation through the waveguide. By using the phase information from the first two Modal-Overlap elements, an iterative process is followed in which the bottom waveguide bend-offset is increased until a phase difference of 45 degrees is observed. With a 45 degree path-length-difference at both ends, the required 90 degree quadrature point is obtained. This results in a bottom bend-offset of $27\mu\text{m}$ and a mid channel separation of $43\mu\text{m}$. The straight in-and-output sections of the Mach-Zehnder are 1 mm long, leaving an effective straight-arm interaction length of 13 mm. Further simulation results of optical wave-propagation are presented in the following section.

3.5.5 Simulation Results

The top-view design-editor allows the definition of Manipulator elements which can simulate the effect of electrodes. A specified phase-constant, assigned to this element, is artificially added to the phase of the propagating wave. A manipulator is placed at the end of the top straight-arm section of the Mach-Zehnder and its phase value is adjusted to simulate three cases. The first denotes full positive interference and requires 90 degrees to account for the waveguide asymmetry. The second simulates the passive device at quadrature and requires zero phase. Finally, the third assumes full destructive interference and requires -90 degrees. Simulation results for the three cases are shown in Fig. 3.9, Fig. 3.10 and Fig. 3.11 respectively. For all cases, a) shows optical wave-propagation through the device and b) shows a comparison of the input (white trace) and output (red trace) optical fields. In the first case, the fields match closely, resulting in a loss of 0.117 dB. In the second case, the propagating wave is disturbed by the incoherent addition of the two waves. It still propagates in the output channel and a loss of 3.19 dB is observed. In the final case, the disturbed wave cannot be guided by the output channel and scatters, resulting in a 34.62 dB loss.

The simulation results is a positive indication that the Mach-Zehnder functions correctly and that it is passively biased at quadrature. A simulation of this design for X-cut crystal reveals that the waveguide still functions, but that the quadrature point is slightly shifted. As a result the waveguide design is generic and can be used to test both Z and-X-cut devices. With the waveguide design complete, focus shifts to the design of the top electrodes.

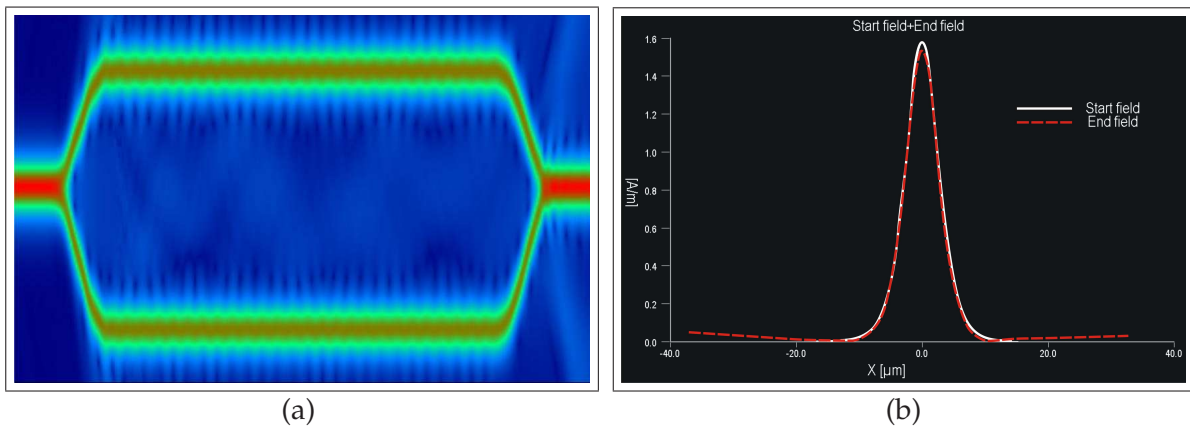


Figure 3.9: Mach-Zehnder with zero phase-shift: a) Optical wave-propagation; b) End-field comparison.

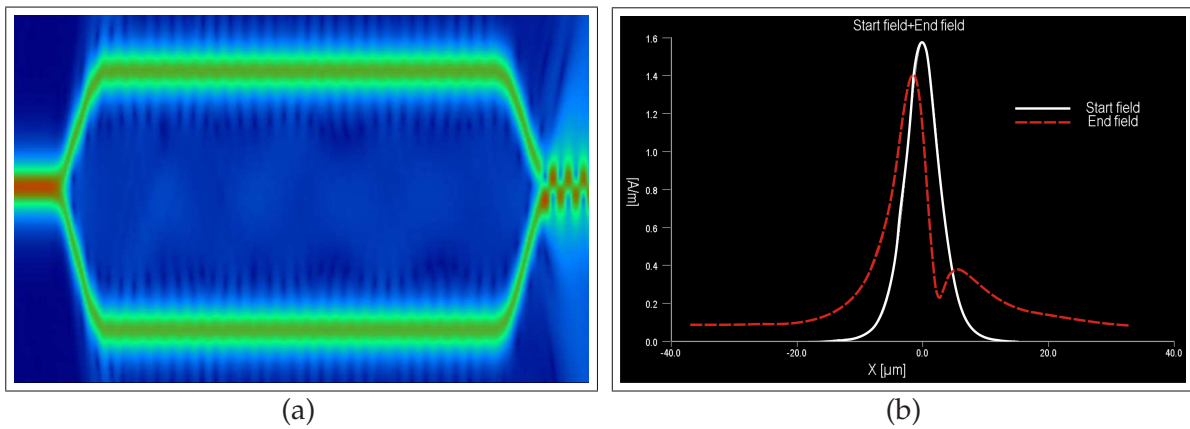


Figure 3.10: Mach-Zehnder with 90 degree phase-shift: a) Wave-propagation; b) End-field comparison.

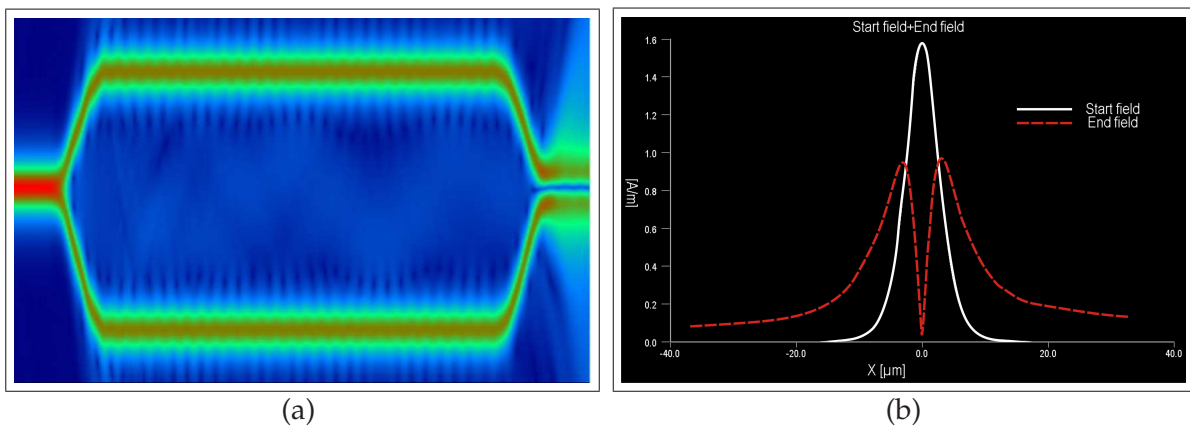


Figure 3.11: Mach-Zehnder with 90 degree phase-shift: a) Wave-propagation; b) End-field comparison.

3.6 Electrode Design

In section 3.2 and Fig. 3.2 the basic layout and function of Z and X-cut electrodes were explained. This must be understood to grasp the electrode designs of this section. Since the Mach-Zehnder waveguide is also usable for X-cut crystals, electrodes are designed for both cuts. In Fig. 3.12, the four different types of electrode designs are illustrated.

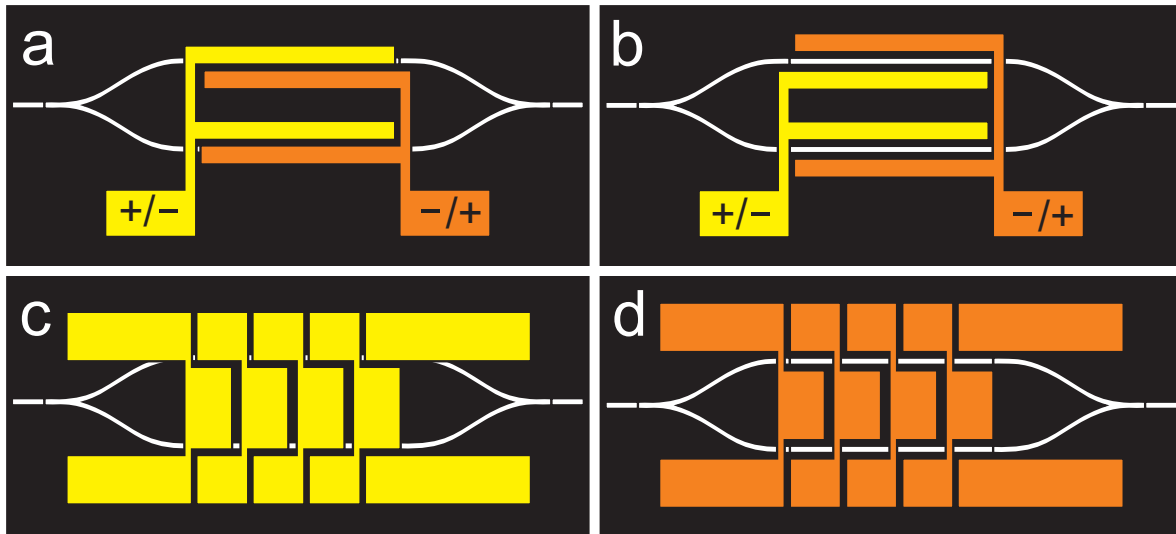


Figure 3.12: Electrode designs: a) Z-cut test electrodes; b) X-cut test electrodes; c) Z-cut, four-element, segmented electrodes; d) X-cut, four-element, segmented electrodes.

In Fig. 3.12 a) and Fig. 3.12 b), test electrodes similar to those used in [20], for Z and X-cut crystals respectively, are shown. The bottom pads allow wire-bonding to an external circuit which can provide a known excitation of DC and low frequency modulating voltages. In such a manner the device can be characterised. This includes determining the half-wave voltage, its actual quadrature point and establishing the electrode-to-channel coupling efficiency. In the designs, a minimum practical electrode gap of $2 \mu\text{m}$ is used. In Fig. 3.12 b), the gap between the waveguide edges and electrodes are $2 \mu\text{m}$, making the total gap for X-cut devices $10 \mu\text{m}$. The wider gap makes the electrode fields weaker, but a transparent buffer-layer is optional since the electrodes are not directly above the waveguide.

The segmented electrodes for field measurements, illustrated in 3.12 c) and Fig. 3.12 d), are based on a design first proposed in [23]. Traditionally an external dipole antenna is connected to the bare test-electrodes or to an RF-electrode with a coplanar structure. This has three main disadvantages: 1) the external antenna causes field perturbations; 2) a considerable mismatch normally exists between the electrode capacitance and dipole impedance and; 3) the device spatial resolution is increased. The segmented electrode design incorporates the antenna directly into a miniature electrode structure and splits up the long electrode length into shorter, matched sections. In [23], optimised segmentation is discussed at length. For a marginally longer waveguide length than considered here, 10 segments were

found to be theoretically optimum. This means that seven should be close to optimum, but we also include segmentations of 4, 10 and 20 on the lithography mask.

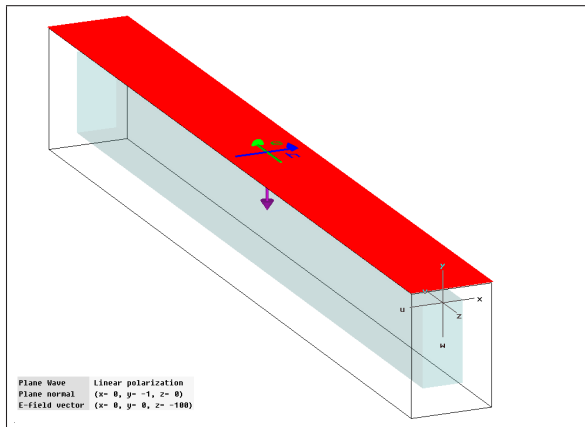


Figure 3.13: CST plane-wave excitation in simulation of segmented electrode.

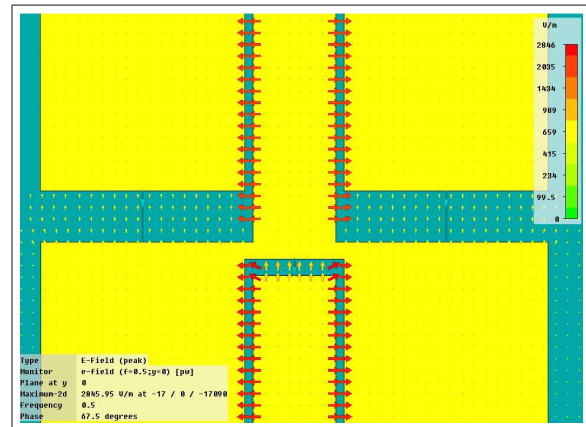


Figure 3.14: CST simulation results: electrode vector E-field distribution at 500 MHz.

A CST model of one segmented electrode structure on a bulk LiNbO₃-equivalent substrate and plane-wave excitation, (red), is shown in Fig. 3.13. The E-field orientation of the plane-wave is indicated by the green vector and its orthogonal H-field component by the blue vector. The direction of propagation is towards the electrode from an offset distance above and is indicated by the purple vector. An E-field result-plot at 500 MHz, after simulated wave-propagation, is shown in Fig. 3.14. It illustrates correctly-oriented field distributions between the electrode gaps and provides confidence in the design. With the functional parts of the sensor devised, the next step involves the layout of a lithography mask in C2V.

3.7 Mask layout

The integrated mask module in C2V complements the design suite and makes the package a handy tool for complete device development. It allows design sections to be imported as independent elements which can easily be duplicated and positioned. Mask elements such as alignment markers and component numbering can be added from a library before direct compilation to the industry standard GDS2 file format.

The final mask layout is shown in Fig. 3.15 and is characterised by practical considerations. The blue and white regions denote opaque parts and the black background is transparent. The usable mask area is limited by the photolithography mask aligner to 2"×2", which fits in four different 20 mm × 20 mm substrate-sized blocks. The bottom left-hand block is a generic Mach-Zehnder waveguide section and the rest are electrode sections. Of these, the top left-hand contains X-cut electrodes while the remaining two have Z-cut elec-

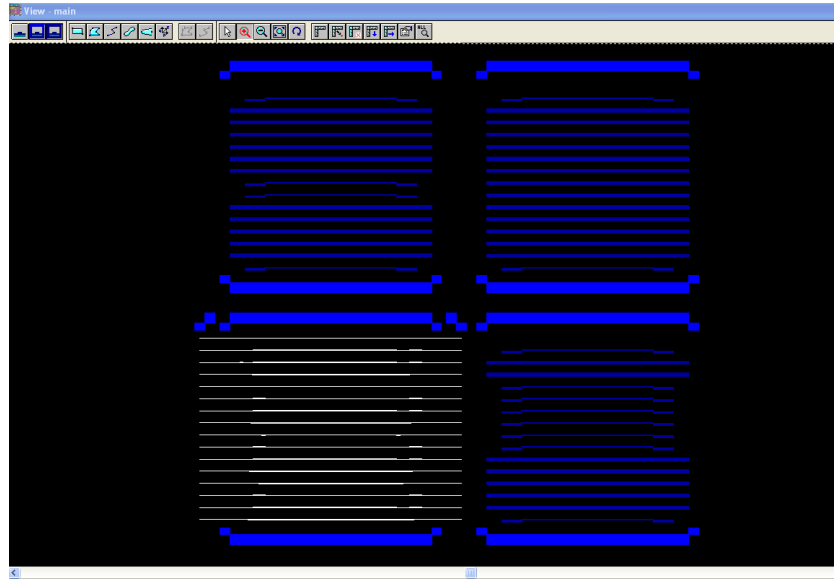


Figure 3.15: View of final mask layout in C2V. Bottom-left: generic waveguide patterns. Top-left: X-cut electrode patterns. Top-right and bottom-right: Z-cut electrode patterns.

trodes. The rectangular outlines at the top and bottom and additional blocks at the corners serve as alignment markers.

In the fabrication process the waveguide block is used to pattern the Titanium thin-film. After thermal diffusion and the application of a possible buffer-layer, one of the three electrode blocks are used to pattern the top electrodes. The waveguide block contains 16 separate waveguides, spaced 1.2 mm apart. Of these, 15 are the Mach-Zehnder design, but the top-most one is simply a 6 μm wide, straight-line waveguide. This will be used to compare propagation loss. The straight ends of the waveguides overlap the block boundaries to accommodate slightly miss-aligned substrates during photolithography alignment. The three electrode blocks are designed to be aligned on top of the generic waveguides by means of the alignment markers at the edges of the substrate. To accommodate the straight, test-waveguide, the top electrode position of all three electrode blocks are kept empty.

The order and block-distribution of the different electrodes are specific. Through practical experience it is known that the substrate centre is likely to provide the best results. This is due to edge-effects which are always present. Since emphasis is placed on creating a Z-cut device, two blocks are devoted to it. In the bottom right-hand block the primary focus is to get a working test electrode. For this reason, the central area has six repeated test electrodes and the remaining positions are a combination of the four different segmented electrodes and two more test electrodes. The top right-hand block is dedicated to Z-cut field electrodes and only has two test electrodes. The different segmentations are alternated to give an even spread with slight positional preference given to the 7-segmented electrode. By having all the designs on each block, the chances of success is maximised. For the single X-cut block, a suitable combination is used with at least two test electrodes in the centre. This completes the lithography mask layout which marks the last part of the design stage.

3.8 System Topology and Test Strategy

Fig. 3.16 shows a schematic diagram of the components for a practical optical E-field sensor. A pigtailed laser diode (LD) with single mode (SM), polarisation maintaining (PM) fibre, provides continuous input light to the integrated sensor. The output is connected to a pigtailed photodiode (PD) with SM-fibre. The laser diode is driven by a stabilised DC supply with feedback. A SA is needed to measure the output of the photodiode. The PM-fibre provides polarised light which is aligned to the correct crystal axis. This is not required for the output since only the intensity is measured. As an alternative to the photodiode and SA, an optical spectrum analyser (OSA), which directly connects to the SM output-fibre can be used.

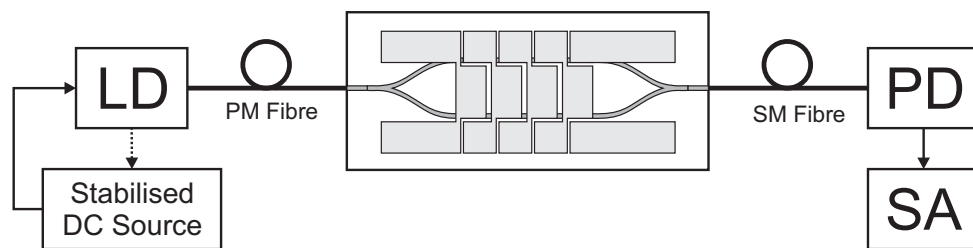


Figure 3.16: Independent, fibre-connected system with laser diode (LD) on the input and photodiode (PD) at the output. A stable DC supply feeds the LD and the PD connects to a spectrum analyser.

To reduce initial cost and risk, the waveguide will first be tested for light-propagation using available equipment. Fig. 3.17 shows the proposed test-setup. Light from a laser source, on the left, is guided via bulk optics on a bread-board into the waveguide. The output-light is collimated into a standard SM-fibre which is connected to an OSA.

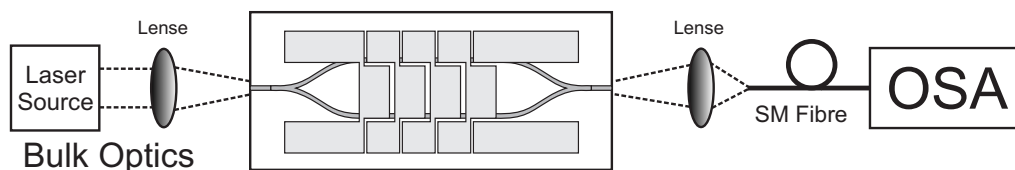


Figure 3.17: Preliminary test system using bulk optics and an optical spectrum analyser.

Once light-propagation is successfully tested, the full independent system of Fig. 3.16, can be considered. The system can then be calibrated for field measurements around the coaxial probe, using a known electric field. This can be generated in several ways, which includes a TEM-cell and parallel plates.

3.9 Conclusion

The LiNbO₃-based optical E-field sensor provides a new approach to solve the problem of characterising sensitive E-fields around the coaxial probe. This chapter presented the first stage in the development of such a sensor. To keep the focus on the coaxial probe problem, an expedient design strategy was followed. This was facilitated through making full use of the many sources of theoretical and practical information regarding Ti:LiNbO₃ waveguide interferometers. In this regard, C2V optical simulation software and its associated supporting documents played a significant role. It was found that optimum Mach-Zehnder waveguides make use of specific S-shaped bends and that aspects like fibre-to-guide mode-matching, mode-confinement and bend-loss are important to consider in the design. When diffusion parameters were finalised, use was made of C2V software to simulate optical wave-propagation and to iteratively establish the correct Mach-Zehnder asymmetry. This ensured that the interferometer was passively biased at its quadrature point. Further simulations provided confidence in the Mach-Zehnder design and also established that it was suitable for X and-Z-cut devices.

The next step involved the development of field electrodes to go on top of the diffused waveguides. An integrated segmented electrode design was chosen, which combines an external antenna into the electrode structure. This improves impedance matching and the spatial resolution of the sensor. Separate test electrodes were also designed for use in device characterisation. The last part in the design process was to combine the waveguide and electrode patterns into a practical layout for the external manufacture of a lithography mask. This was easily done in the C2V design suite, which allows the separate elements to be imported and duplicated in a mask layout interface. Finally a systems overview and test strategy for the sensor completed the chapter.

By considering manufacturing issues early in the design-phase of the sensor, much time and costs were spared. This was only possible through prior lab experience, which highlights the value of having some practical background in a design environment. With the design complete and the lithography mask received from the manufacturer, fabrication can commence. This is discussed in the following chapter.

Chapter 4

Mach-Zehnder Manufacture

Chapter 4 reports on an in-house attempt at manufacturing the optical E-field sensor, designed in Chapter 3. Although the sensor itself is interesting, the primary focus remains the characterisation of CM-current on the exterior of the coaxial probe. Despite good initial progress, we elected to stop work on the sensor because of manufacturing difficulties with concomitant time constraints. Attention shifted to an alternative approach for solving the coaxial probe problem and this is presented in chapter 5. Since interest in such a sensor might prompt future developments, documenting this work is important. What follows in this chapter is a brief but detailed description of the manufacturing progress that was made and the problems that were solved. The first section gives a quick overview of the whole fabrication process. Thereafter, each of the completed fabrication steps are briefly discussed according to its procedure, the specific parameters that were used, and solutions that were found to problems. Finally, the chapter conclusion brings all the elements into perspective.

4.1 Fabrication Process Overview

Standard semi-conductor techniques and equipment are needed to fabricate the sensor. Fig. 4.1 shows a cross-section illustration of the process. The evolution of the LiNbO₃ substrate into a sensing element can be seen through the progression of ten main processing steps. The process can be split into two phases: that of the waveguide, on the left of the figure and that of the electrodes on the right. The first step involves the application of a uniform photoresist coating on a bare LiNbO₃ substrate. Photolithography is then used to pattern this coating into a negative of the waveguide mask. At this point the substrate is ready for Titanium thin-film deposition. The Titanium deposits on the exposed parts of the LiNbO₃ and on the patterned resist. A lift-off process is then used to remove all photoresist, leaving the required Titanium waveguide pattern on the LiNbO₃ substrate. Thermal diffusion in a high temperature furnace marks completion of the waveguide phase. In Fig. 4.1, the diffused channels are indicated by the red regions below the LiNbO₃ surface.

For the electrodes, a SiO₂ thin-film buffer-layer is first deposited on top of the Ti:LiNbO₃ waveguides. This step is optional for X-cut devices as explained in Chapter 3. The pho-

tolithography, deposition and lift-off process is repeated, using one of the three electrode masks to pattern the gold electrodes. The only difference is that a thin (few nm thick) chromium layer is deposited prior to the gold, for adhesion to the SiO_2 . After semiconductor processing, the product is shown at the bottom right of Fig. 4.1. The only remaining step in the completion of the sensing element, is optical end-face polishing of the LiNbO_3 substrate. This allows light from a fibre-optic cable to be coupled into the waveguide.

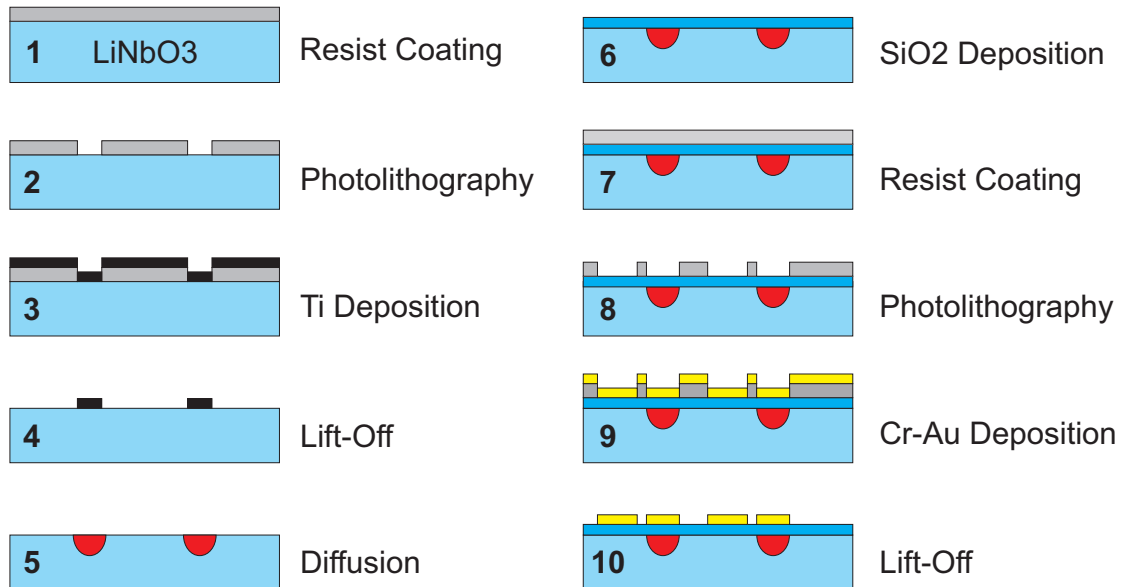


Figure 4.1: Illustration of the required fabrication process to manufacture the optical E-field sensor.

A reader less familiar to semiconductor processing might view the process as trivial, but the above description cannot convey the full extent of the effort it represents. Work on the sensor eventually stopped at the diffusion stage of the waveguide. Each of the preceding steps are successfully implemented and presents their own specific problems and solutions. This is discussed in the following sections.

4.2 Lithography

4.2.1 Facilities

Fabrication of micro-structures through semiconductor processing generally requires a proper clean room. The primary available facility is an unmaintained class 100 clean room that is in a long term process of restoration. It contains a mixture of old and new semiconductor equipment, some of which date to the 1980's. The photolithography equipment consists of an ultrasonic bath, spin-coater, heat plate and a Carl Suss mask aligner. The lab infrastructure includes UV-filtered lighting, deionised water, an integrated network of gas, vacuum, water, compressed air and electrical outlet points and dedicated gas storage facilities. For analysis of photolithography patterns, a high quality optical microscope and an Atomic

Force Microscope (AFM) are available. The latter allows 3D scans of lithography and other thin-film patterns and is an essential tool.

4.2.2 Procedure

Standard lithography procedure dictates thorough sample cleaning as a first step. This is achieved by placing the substrate in an ultrasonic bath containing acetone followed by ethanol. An alternative method is to use an oxygen or ozone plasma cleaner. It was found that the virgin LiNbO₃ substrates are acceptably clean in the received packaging and that any attempt at cleaning them in the available facility results in contamination. The crystals are carefully opened and immediately placed on the spin-coater. The spin-coater is briefly activated and the substrate is manually dusted with a nitrogen hose. Negative-tone photoresist, ma-N 1420 from Micro Resist Technologies, is dripped onto the substrate covering the whole surface. Through centrifugal force the substrate is coated with a thin layer of photoresist at 13 000 rpm for three seconds. Vacuum from below holds the substrate in place. To partially cure the resist, the substrate is then placed face-up on a hotplate for 2 minutes and 10 seconds at 100 °C. This is called pre-bake and prevents the substrate from sticking to the lithography mask in the next step, which is UV-exposure. The substrate is placed close to its final position in the mask aligner, almost touching the mask above. Prior to mask contact, alignment is achieved through micro-adjustment of the substrate holder and the use of the aligner's microscope. Uniform UV-exposure is applied for 30 seconds which activates the exposed parts of the resist. The substrate is then placed in ma-D 533/S developer, for 45 seconds and is finally rinsed in deionised water. Development strips away unexposed resist, leaving a negative of the mask design and completing the lithography process. An optical microscope view, Fig. 4.2, and an AFM scan, Fig. 4.3, is shown of the final result.

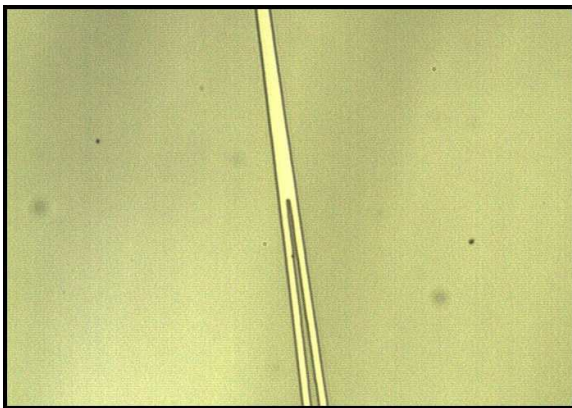


Figure 4.2: Microscope view of lithography.

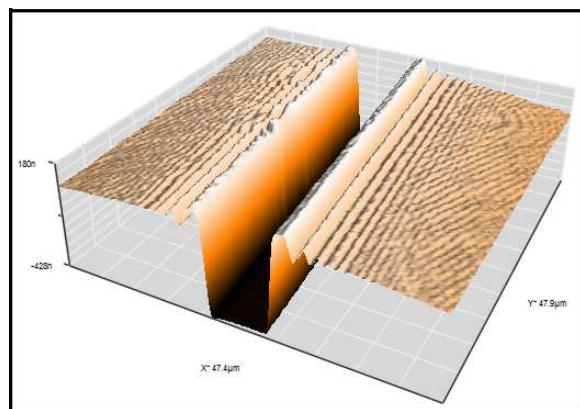


Figure 4.3: AFM scan of lithography.

4.2.3 Notes, Problems and Solutions

To obtain optimum photolithography parameters, some experimentation is required. Although recommended parameters are provided in photoresist data sheets, they serve as a rough guide only. Values have to be adjusted according to the specific conditions, e.g. the 2 mm thick LiNbO₃ substrates requires a longer pre-bake time to allow for adequate heat distribution. Results also deviate due to variations in laboratory conditions. With experience, symptoms can readily be identified under a microscope and ratified through suitable compensation of parameters. A well-established technique to enhance lift-off is the creation of undercut edges, illustrated in Fig. 4.4. By prolonging development, the edges of the exposed resist are eroded from the base and forms an undercut. The reason this is desired is explained in section 4.4, which deals with lift-off.

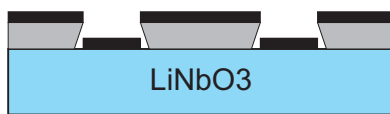


Figure 4.4: Undercut edges achieved through prolonged development.

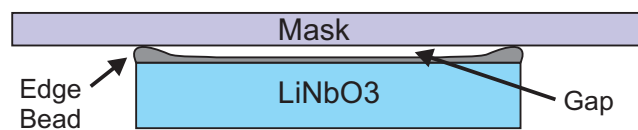


Figure 4.5: Illustration of photoresist edge-bead and induced mask offset which influences UV-exposure.

Fig. 4.5 illustrates one of the more persistent lithography problems that is encountered. It is known as "edge bead" and is caused by the accumulation of photoresist at the edges of a spin-coated substrate. This is a natural phenomenon, related to the substrate surface-tension and the resist viscosity. The thick coating at the edges requires greater UV-exposure, causing either over-exposure in the centre or under-exposure at the edges. Fig. 4.6 clearly shows the edge bead on the left and narrowing of the waveguide channel due to under-exposure.

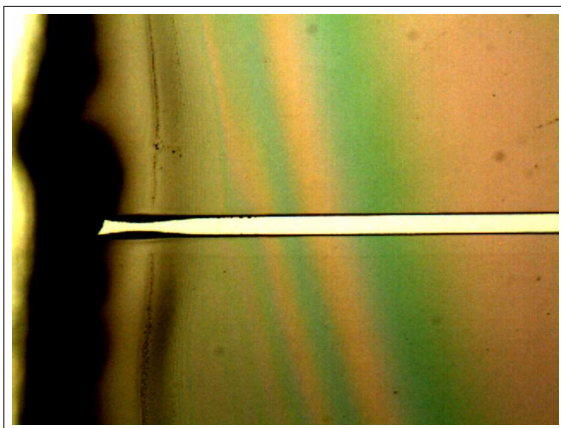


Figure 4.6: Under-exposure due to edge bead.

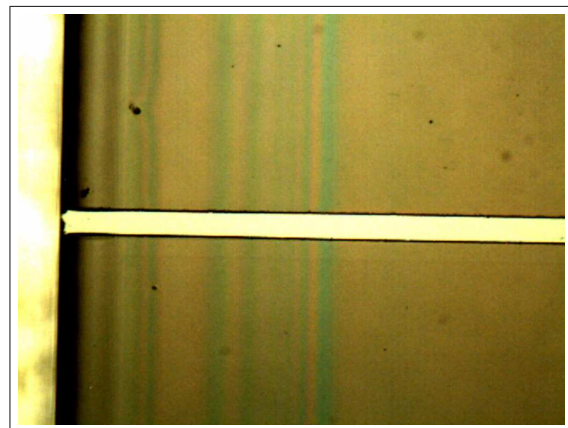


Figure 4.7: Successful channel after experimentation.

In addition, the small air-gap between the substrate and mask reduces resolution due to refraction. Normally edge bead is resolved by chemically or mechanically removing it

from the edges of a wafer and then dicing that into the required pieces. Unfortunately we have no means to dice LiNbO_3 and thus substrates are ordered in final size. The edge bead now presents a challenging problem. To beat the bead we experiment with different spin rates, spin times and UV-exposure. Spinning faster or longer, more resist gets thrown off, but more also spreads to the edges. It was found that a quick, fast spin sheds much excess resist while limiting migration to the edges. Fig. 4.6 demonstrates a successful channel after experimentation. Despite the success this is by no means an elegant solution. A narrow margin exists between over and under-exposure and especially at the top and bottom of a substrate, good results are not guaranteed.

4.3 Titanium Deposition

Following lithography, Titanium deposition is the third step in the fabrication process. Titanium is an industry-standard thin-film material which is often combined in reactive processes to form insulating Titanium oxides and hard Titanium nitride layers. Despite this, very little practical information is freely available on the internet about pure Titanium deposition. In the absence of standard deposition equipment we start out with little knowledge of the exact film characteristics and apply prior knowledge of superconductor thin films. The following sections explain four deposition techniques that are investigated, the problems faced and the results that finally lead to successful Titanium deposition.

4.3.1 Thermal Deposition

Thermal deposition is a well-known technique that entails melting a material, usually through electrical current, within a vacuum environment so that an energetic vapour of that material coats the inside of a chamber. Since the melting point of Titanium is $1600\text{ }^\circ\text{C}$ this technique is not usually suitable. However, a standard thermal evaporator is available and we hope that Titanium powder can be thermally evaporated due to the increased surface area and enhanced heat transfer from the tungsten boat. We set the supply transformer to maximum, but not enough heat is generated to melt the particles and the method had to be abandoned. Unfortunately, after successful deposition was achieved by another method, it was discovered that thermal deposition of Titanium powder is possible. This can be achieved by increasing the tungsten boat resistance through suitable modification, as shown in Fig. 4.9. The standard boat is shown in Fig. 4.8. Note: eye protection is required for viewing such high-energy thermal deposition.



Figure 4.8: Standard Tungsten boat with low resistance and insufficient temperature.

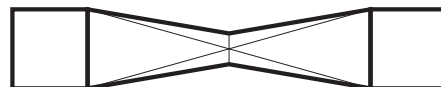


Figure 4.9: Modified, narrower Tungsten boat with increased resistance and higher temperature.

4.3.2 Pulsed Laser Deposition

With the failed attempt at thermal evaporation, an established technique, used in high temperature superconductor research, is investigated. This method is called pulsed laser deposition (PLD). A high-energy, pulsed laser is focused onto a rotating Titanium target within an argon environment in a vacuum chamber. Due to the concentrated energy, target material is vaporised into a plasmic plume of energetic particles. The substrate is positioned within this plume and is coated with a uniform layer.

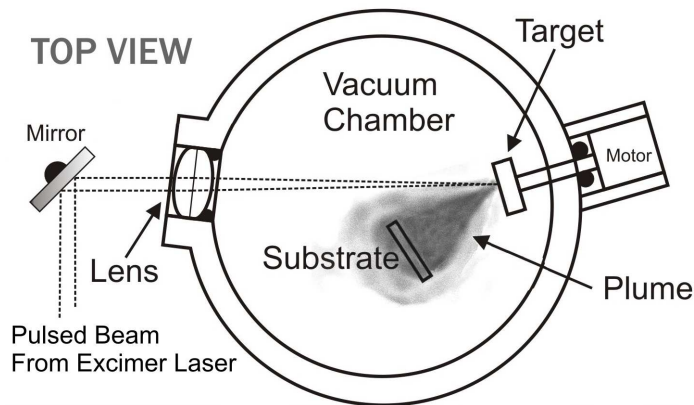


Figure 4.10: Pulsed Laser Deposition (PLD).

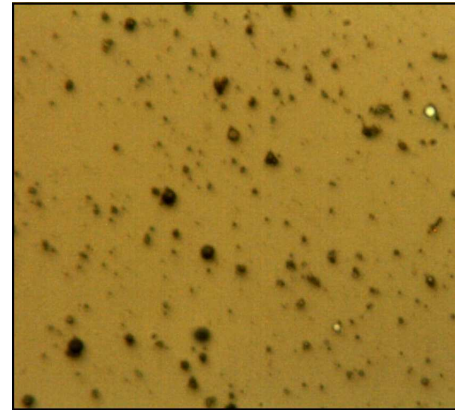


Figure 4.11: Poor Titanium film by PLD.

Fig. 4.10 shows a top view illustration of a PLD system. The advantage of this method for superconductor research is control over film structure. This is not important here since the Titanium will be diffused. We test deposition at a working argon pressure of $5.0\text{E-}3$ mBar after pumping to a base vacuum of $1\text{E-}4$ mBar. The 308 nm Excimer laser is driven at 22 kV and provides a pulse energy of 0.24 Joule at 5.3 Hz. The substrate is placed between 35 mm and 60 mm from the target. Unfortunately, after varying these parameters in repeated tests, results stay disappointing. Fig. 4.11 shows the reason: films are scattered with large Titanium particles. During deposition the laser starts eroding the target and a micro trench is formed. The uneven energy distribution then cause larger, unvaporised Titanium chunks in the plume, spoiling the film. With the softer superconducting materials this is not such a problem. Even using a strong, permanent magnetic field to generate a Lorentz force to deflect smaller ionised particles onto a displaced substrate, as described in [34], proved ineffective. The last in-house option for Titanium deposition is a self-built Inverse Cylindrical Magnetron (ICM) sputtering unit which is also used for superconductor research.

4.3.3 Inverse Cylindrical Magnetron Sputtering

Fig. 4.12 shows a cross-section of an ICM and illustrates its principle of operation. Note, the figure is an object of revolution. This removable head seals on top of a vacuum chamber with connected pumps. After obtaining the desired base vacuum, controlled argon is bled in

from the top. The gas flows through a strong, DC-induced E-field between two electrodes: the positive jet at the top and the negative target. This ionises the argon atoms and a plasma is formed as shown in Fig. 4.13. The charged particles move down into the sputter region and are trapped against the target by strong H-fields from permanent magnets. The H-fields cause these charged particles to spin around the inside of the target in the "race track" region, and through energetic collisions with the target, Titanium atoms are knocked free and deposit on the substrate below.

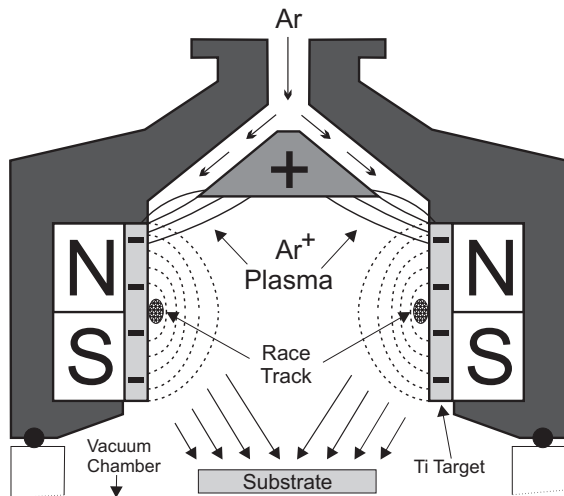


Figure 4.12: Cross-section illustration of Inverse Cylindrical Magnetron (ICM).

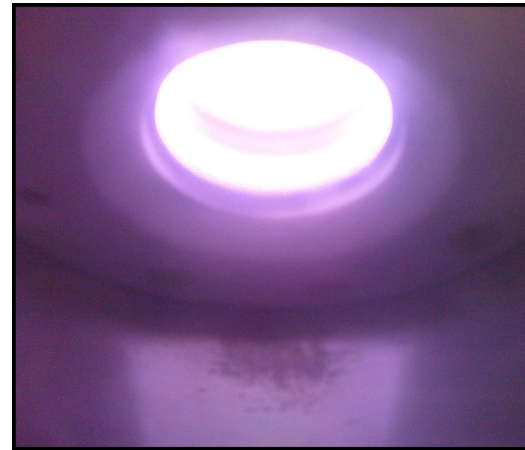


Figure 4.13: ICM plasma during deposition, seen through viewing glass.

With this system we achieve quality films with the same blue, metallic shade that was achieved in the PLD process on silicon test substrates. We use a $1\text{E-}4$ mBar base pressure, and limit argon flow for a working pressure of $2.4\text{E-}1$ mBar. The current-controlled DC supply is operated at a maximum of 400mA, delivering about 160 Watts. Deposition rate is established by coating lithography-patterned, silicon test substrates, doing lift-off and then measuring film thickness with the AFM. Problems with non-uniformity are solved by placing the substrate off-centre on a rotating holder. Overheating of the resist is resolved by allowing cool-down periods. With the process established we coat the first LiNbO_3 substrate, but find that the film is transparent and non-conductive. Further investigation reveals the films to be oxidised Titanium, which is transparent. The opaque silicon test substrates causes the blue colouration. Leak detection on the system reveals a few tiny leaks and the same is suspected for the PLD system. We now realise the complexity of this simple task without the proper equipment and resort to external facilities at iThemba Labs.

4.3.4 E-beam Sputtering

At iThemba Labs an e-beam evaporation system, shown in Fig. 4.14, is routinely used for Titanium deposition. This method is similar to thermal deposition, but the energy needed

to melt the Titanium is provided by a focused electron beam. This is a high vacuum system which uses a fore-pump, turbo-pump, ion-pumps and liquid nitrogen cooled cryogenic trap.



Figure 4.14: Cryo-cooled, high-vacuum e-Beam evaporator at iThemba labs.

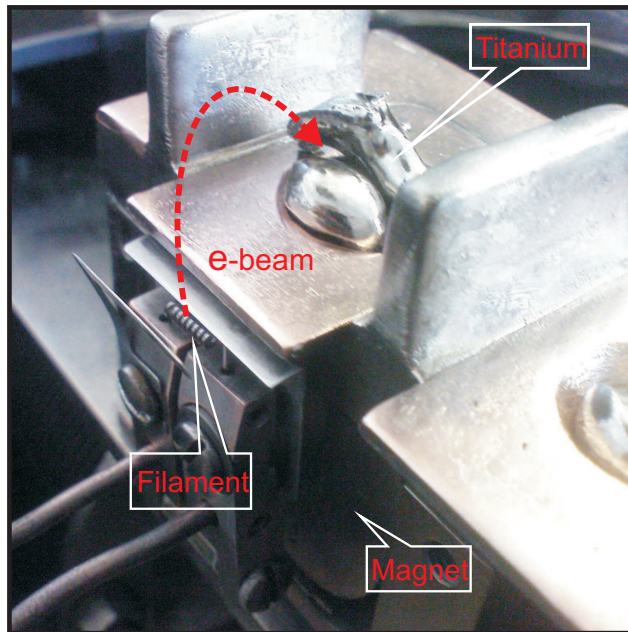


Figure 4.15: Inside the chamber: Copper crucible with filament, large U-magnet and Titanium evaporant.

Fig. 4.15 shows a picture of the e-beam apparatus on the inside of the chamber. Its operation is similar to a cathode ray tube. A high-voltage source drives a tungsten filament which generates electrons in the high-vacuum environment. Two accelerator plates, adjacent to the filament, create an intense electron beam which is directed by a permanent magnetic field onto the evaporant. This is placed in a copper, water-cooled crucible on top. The vaporised material then uniformly coats the substrates which are placed facing down on holders above the crucible. The system is equipped with a deposition rate sensor which is calibrated for Titanium and gives an accurate indication of film growth. High quality, 850 Å thick films are obtained within a few minutes and no uniformity or heating problems are experienced. The films have a shiny appearance, similar to aluminium but not as bright.

4.3.5 Lessons learnt

Much was learnt about Titanium deposition and thin-film growth in general. Titanium is known as an "oxygen getter" and is even used in wire form as a method to obtain higher vacuums. After deposition the e-beam chamber is left under high vacuum to cool down for two hours to prevent oxidation. The need for this precaution was not known previously. Extensive practical knowledge is hard to come by but is important. Results should always be approached with a healthy degree of scepticism and established techniques for film analysis

are invaluable. With proper Titanium deposition finally achieved, the next phase in the fabrication process entails lift-off.

4.4 Lift-off

Lift-off simply implies the process of chemically removing a lithography base layer below a thin film and leaving behind a desired pattern consisting of only the parts that were deposited directly onto the substrate. This is clearly illustrated in Fig. 4.1. The chemical has to be such that it dissolves the photoresist without interacting with the substrate or film. Either a dedicated photoresist remover or acetone can be used. We use Acetone since it is affordable and is proven to be as effective. In Fig. 4.16 lift-off is underway in a Pyrex beaker.

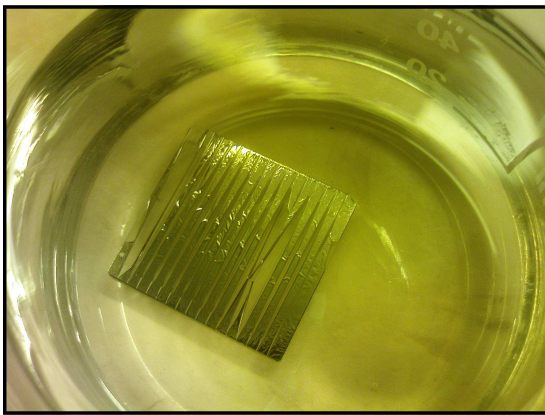


Figure 4.16: Lift-off in Acetone taking place in a Pyrex beaker.

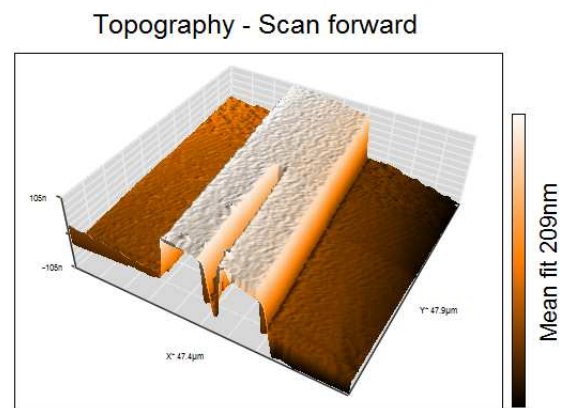


Figure 4.17: AFM scan of a Mach-Zehnder structure after clean Titanium lift-off.

With good quality lithography and film, visible de-lamination of the Titanium occurs spontaneously within a few minutes. To remove smaller, more stubborn parts, for instance between the waveguide arms, an ultrasonic bath is required for up to a minute. An AFM scan of a Titanium waveguide structure after clean lift-off is shown in Fig. 4.17. The lithography edge undercut, mentioned and illustrated in section 4.2.3, plays an important role. Excess parts of the film have to tear loose from the remaining film and with the undercut's overhang, this boundary is made weaker. Good film adhesion to the substrate is as important, especially for the long, thin waveguide structures. Due to the lithography difficulties, discussed in section 4.2.3, clean lift-off is not frequently obtained. In most cases the ultrasonic bath causes damage to the fragile waveguide structures while other parts do not separate. An attempt at using an accurate laser to correct some of the structures by ablation showed some promise, but due to availability and time constraints the exercise could not be completed. This underpins the value of having repeated structures on the same substrate and ensuring quality lithography before proceeding to deposition. Despite the challenges, some complete Titanium waveguide structures are achieved on the LiNbO₃ substrates and the fabrication process can continue to the diffusion stage.

4.5 Diffusion

Titanium diffusion was introduced in section 3.3 and specific parameters were chosen. Attention now shifts to the practical implementation of these parameters. Diffusion requires more than just a high temperature furnace. The LiNbO_3 crystal has to be heated in a "wet" Oxygen environment to prevent Li_2O out-diffusion and the formation of Niobium rich LiNb_3O_8 , inducing optical losses [29]. This is achieved using a setup shown in Fig. 4.18.

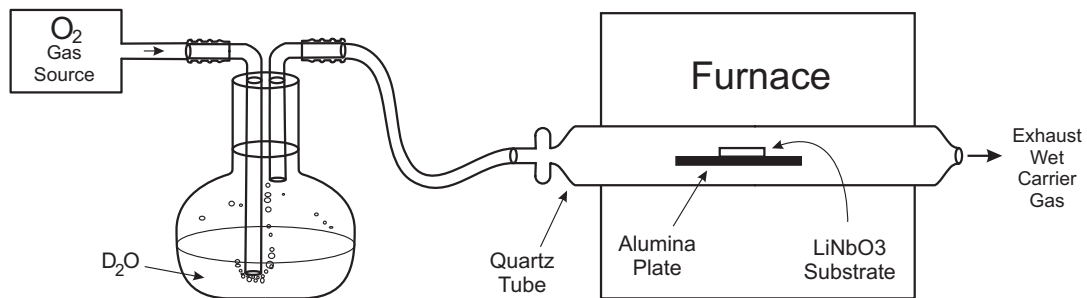


Figure 4.18: Illustration of furnace setup for Titanium diffusion after [6].

A controlled flow of oxygen carrier gas, is bubbled through Deuterium Oxide (D_2O) in a glass vessel and the product, a moist gas mixture, is fed from the top into a quartz tube. The tube, containing one or more patterned LiNbO_3 substrates on an alumina plate, is placed in a high temperature furnace and has an exhaust opening at the end. D_2O is an isotope of water and is better known as Heavy Water. Traditionally, deionised water is used since it decomposes into H^+ and OH^- and inhibits the formation of LiNb_3O_8 . D_2O still performs this function but, due to the extra neutron in the hydrogen nucleus, it prevents problems associated with the migration of resident protons (H^+) that affect modulator bias stability [6]. Temperature is slowly ramped to $1050\text{ }^\circ\text{C}$ at a rate of $10\text{ }^\circ\text{C}$ per minute and maintained for the required period. Thereafter the same rate is used to ramp down. Throughout the process an oxygen gas-flow rate of 1.2 standard cubic feet per hour is used. Fig. 4.19 and Fig. 4.20 shows photographs of the diffusion setup.

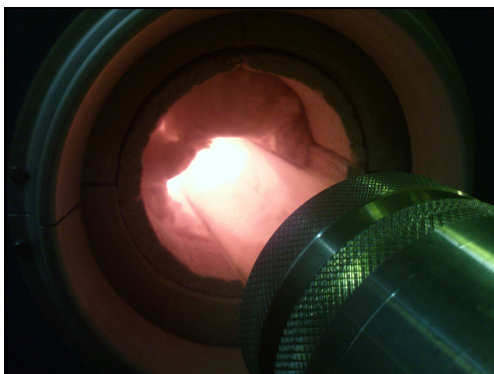


Figure 4.19: Quartz tube at furnace entrance.

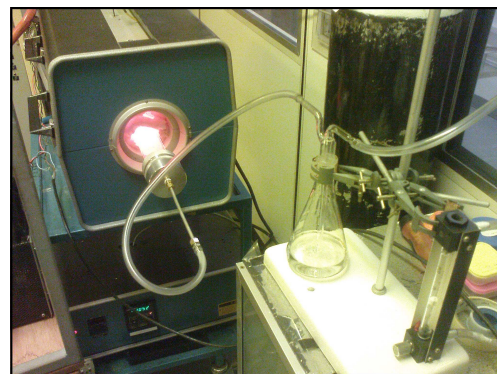


Figure 4.20: Diffusion setup, as shown in Fig. 4.18.

Initial diffusion tests are performed on X-cut substrates before including Z-cut samples. Despite all efforts to conform to published requirements, diffusion results are disappointing. Fig. 4.21 b) - Fig. 4.21 d) shows three AFM results out of a number of diffusion trials. These can be compared to the pre-diffusion state in Fig. 4.21 a). Complete Titanium diffusion is expected, but this is clearly not the case.

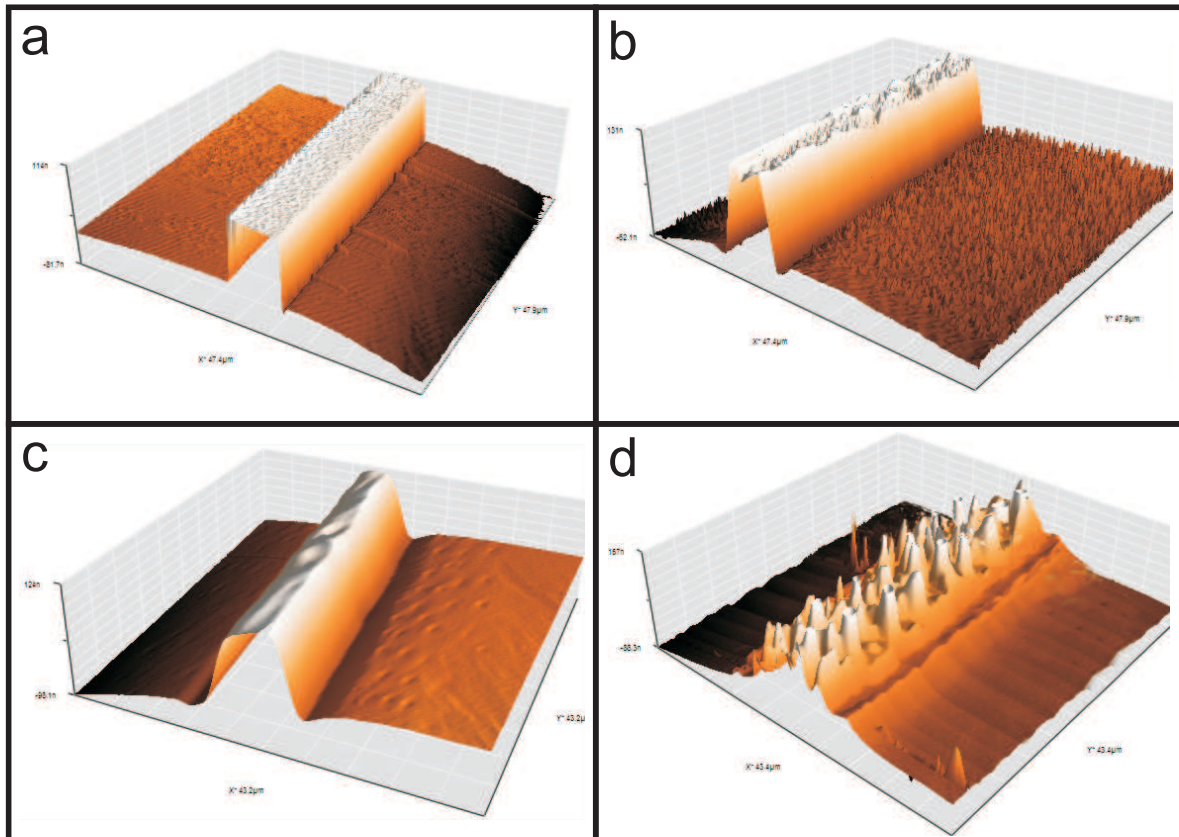


Figure 4.21: AFM scans of diffusion results with: a) Titanium structure before diffusion; b) X-cut for 6 hrs at 1050 °C ; c) X-cut for 9 hrs at 1050 °C; and d) Z-cut for 6 Hrs at 1050°C.

For the X-cut crystals, Fig. 4.21 b) and Fig. 4.21 c), the initial structure, Fig. 4.21 a), loses its sharp edges and becomes more rounded at the top with slight deformations. Strangely, the structures are taller after diffusion. This suggests that the oxidation process causes expansion rather than diffusion. The visible trenches adjacent to the structure in Fig. 4.21 c), for the longer diffusion time, hint at the start of some diffusion activity. Unfortunately longer diffusion times or a higher temperature have little effect. Z-cut results appear slightly more encouraging. Fig. 4.21 d) shows obvious LiNbO₃ surface deformation and what appears to be partial diffusion. However, expansion is still prevalent and like the X-cut cases, further tests prove fruitless. These results are contrary to practical information in literature which generally allude to the simplicity of the diffusion process. Therefore, some less-obvious cause, like contamination of some sorts is suspected to be the culprit. Finding this problem demands practical expertise and proper equipment which was not available. Due to the

time already afforded to fabrication and the long turn-around time for producing diffuse-able samples, we decided not to pursue this problem any further and to cease all practical activity on the sensor.

4.6 Conclusion

The intent of this chapter is made clear in the introduction: it serves as an abbreviated account of the practical work that was done on the optical E-field sensor for future reference. After the fabrication process is introduced in broad terms, only essential information about each step is provided in the sections that follow. These steps include lithography, Titanium deposition, lift-off and finally diffusion. Thereafter, practical work was discontinued. Particular attention is focussed on the problems that were faced and the solutions that were found. The optical sensor is merely an interesting means to solve a specific problem: that of sensitive E-field measurements around the coaxial probe. It is unfortunate that a stage was reached where fabrication efforts became counter-productive to this. It can be argued that if the time permitted diffusion difficulties to be overcome, the rest of the process could quite realistically be achieved. Despite the apparent failure of this attempt, valuable problem-solving skills were learnt and the world of micro-fabrication and vacuum technology was introduced to the author. The following chapter presents an alternative approach to solve the coaxial probe problem.

Chapter 5

Exterior Field Analysis

Due to the unsuccessful manufacturing of a sensitive optical E-field sensor for measurement inside the shield cavity of the coaxial probe, the extended centre conductor E-field probing technique, described in section 2.5 is re-considered. This chapter describes the implementation of this method as a means to validate CST simulation models, which allows E-fields and CM-current to be inspected by use of an extended range of field monitoring options. As a result, EM field distributions can be visualised for different probe environments. This provides insight into the physics and behaviour of CM-current on the exterior of coaxial probe systems and finally allows comment on the effectiveness of different shielding methods to isolate the coaxial probe from VNA feed cabling.

5.1 The Coaxial Probe

In this investigation the same SMA coaxial probe system that J. Badenhurst used for the initial field probing studies, discussed in section 2.5, is used. A cut-plane view illustration is shown in Fig. 5.1 and a 3D model view is shown in Fig. 5.2. The probe is based on a 200mm long, 3.6mm outer diameter, copper semi-ridged cable with PTFE bead. A standard male SMA connector is fitted at the top which connects to a modified SMA panel mount connector. This serves as a removable, flanged probe-face. At the bottom, a threaded female SMA connector fits through a thick Aluminium disc which forms the base for a removable shielding cylinder. The shield is fashioned from standard 3.5 inch outer diameter Aluminium pipe with a 5mm wall thickness.

The most relevant model dimensions are that of the inner shield cavity and the probe flange. The cavity inner height is 206.3 mm and the inner diameter is 79 mm. The flange is square with side length of 12.7 mm and has four symmetrically spaced 2.5 mm holes. The exact dimensions of all the standard components can be found in [8]. The semi-ridged cable assembly is secured onto the Aluminium base with a standard Brass nut on the female connector thread. The shield can be securely screwed onto the base from the bottom using eight 2.5 mm threaded screws. Another important feature is the recess in the outer rim of the base, shown in Fig. 5.1 and Fig. 5.2, which allows an extended galvanic contact area

between the base and the snugly fitting shield. This prevents current from escaping through "leaky seams" and making the cylinder less effective as a shielding element.

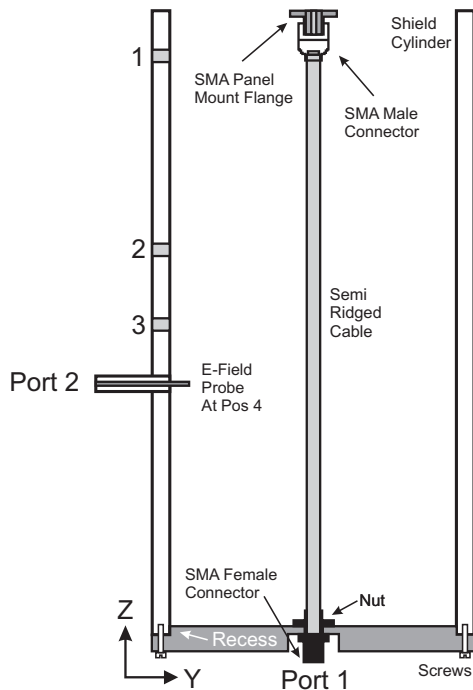


Figure 5.1: Cut-plane illustration of coaxial probe with surrounding shield and side E-field probe.

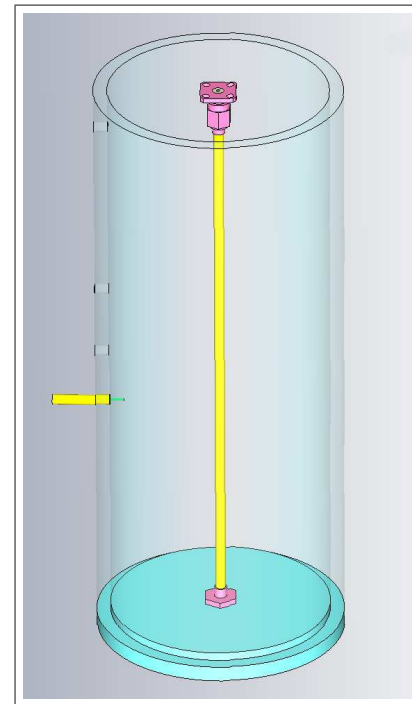


Figure 5.2: 3D view of coaxial probe with semi-transparent shield and E-field probe on the left.

On the left hand side of Fig. 5.1 the E-field probe is shown leading through the shield wall into the cavity at position four. The centre height is spaced 125 mm from the top of the shield. Three other field-probing positions are also marked in the figure and are spaced 15 mm, 80 mm and 105 mm from the top of the shield in ascending order of annotation. Port one of the VNA feeds the coaxial probe from the bottom female connector while port two is connected to the E-field probe which also terminates into a standard SMA female connector.

5.2 CST Simulation

The finite volume time domain (FVTD) commercial simulation software package, CST Microwave Studio is used to simulate the coaxial probe, including the shield and outer environment. The following subsections discuss different elements of the modelling process. Simulation results are deferred to section 5.3.3 where it is compared to VNA measured results.

5.2.1 The Simulation Model

Since the aim is to study external E-fields and the behaviour of CM-current on the exterior of the coaxial probe, accurate modelling of the inner functional parts of the probe, as well

as the outer geometries of the different components is important. Data sheet information for standard SMA components is used as far as possible to obtain precise dimensions. For manufactured components such as the shield and base, accurate physical measurements are used.

Some elements of standard connector inner design are proprietary and are not published. This makes accurate modelling of the inner probe impossible and as a result, suitable simplifications are made; 1) The semi-ridged to female connector transition at the bottom is ignored by having the semi-ridged coaxial dimensions continue down to the lower port. This is shown in Fig. 5.3; 2) the upper transition from semi-ridged to SMA in the male connector is approximated from assembly information and is shown in Fig. 5.4.

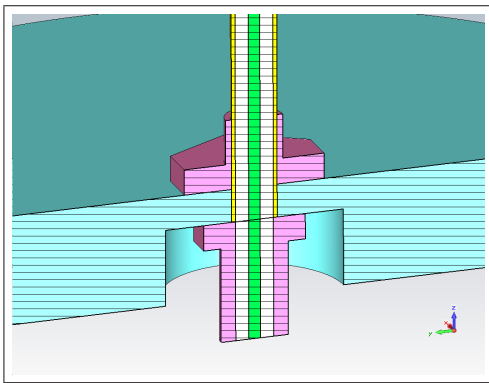


Figure 5.3: Semi-ridged cable dimension is maintained through the female connector.

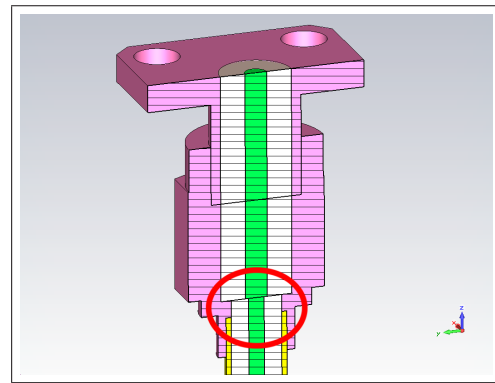


Figure 5.4: Simplification of interior transition from semi-ridged to male connector at the top.

Since manufacturers design these connectors to match the characteristic impedance for dimensional transitions, the first simplification is seen as an acceptable compromise. The larger coaxial dimensions of the top flange and male connector could not simply be used internally for the semi-ridged cable since it does not fit in. Also, extending the outer diameter of the semi-ridged cable to accommodate this would invalidate the model outer geometry. Other elements of physical inaccuracy include gaps between components that vary due to torquing and manufacturing tolerances.

Component materials are chosen from the CST material library and where possible, include material loss. The probe flange and standard SMA connectors are defined as Brass since the actual alloy from which they are manufactured is not available in the library. The semi-ridged cable bead is defined as PTFE(lossy), the centre conductor as Silver and the outer conductor as Copper. The same is used for the E-field probe. Single mode waveguide ports are defined at the bottom face of the female connector, port one, and the end of the E-field probe, as port two. The positions of these ports are indicated in Fig. 5.1

5.2.2 Meshing

The use of CST for modelling coaxial probes is reported in literature, [2], and in some cases implementations are documented in detail [11]. These simulations usually model only the local region of the probe face and MUT interface and make use of fine mesh distributions. What makes this specific application more challenging is the fact that the small internal coaxial geometries of both the coaxial probe and the E-field probe are combined with a comparatively large outer environment in an extended simulation domain. This is accentuated by the need for equating sensitive field distributions and as a result significantly increases meshing requirements for accurate simulations.

With the default option, "Automatic mesh generation" selected, CST computes a suitable mesh (3D discretisation of the model) according to an "expert system" and a vast range of user definable options. For this investigation the transient solver is used, which makes use of a Hexahedral mesh arrangement. There are three principal global parameters for mesh density control. The first is called: "Lines per wavelength", and applies a specified mesh line spacing limit according to the shortest wavelength in the simulated band. The second option, named: "Lower mesh limit", governs the lowest allowable mesh step with respect to a minimum domain dimension and is applied irrespective of the first setting. The final parameter can either be specified as: "Mesh line ratio limit" or "Smallest mesh step" and provides a measure of control over the ratio between the largest and smallest mesh steps in the domain. These settings strongly contribute to the accuracy of the simulation with a trade-off to computation time. According to CST documentation [35], not only the total number of mesh elements increase computation time, but also the degree of spatial concentration. As the mesh elements get closer, the required simulation time steps become smaller, increasing the computational overhead.

With this in mind, it becomes apparent that specifying global mesh parameters to sufficiently mesh the smaller structures would result in a large number of unnecessary mesh elements. To solve this problem a coarser mesh is specified globally and for smaller structures, component specific mesh parameters are set. Fig. 5.7 shows a cut-plane CST view of the total mesh structure.

Table 5.1: Global mesh settings.

Parameter	Value
Lines per wavelength	27
Lower mesh limit	24
Smallest mesh step	0.3

Two local mesh regions, magnified in Fig. 5.5 and 5.6, for the semi-rigid cable assembly and the E-field probe, respectively. The final global mesh parameters are specified in table

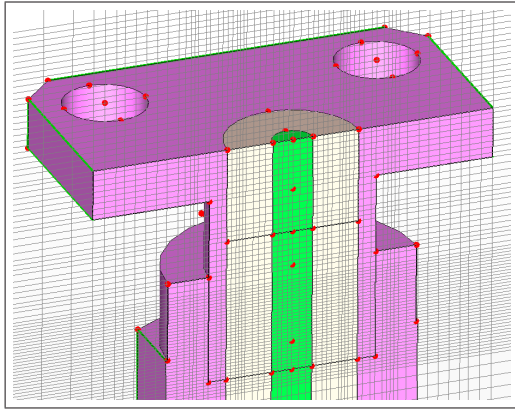


Figure 5.5: Local meshing at coaxial probe flange.

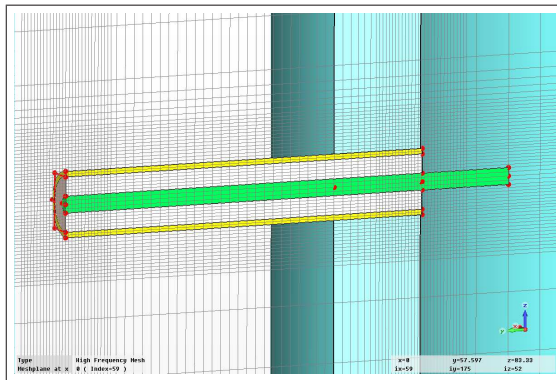


Figure 5.6: Local meshing at E-field probe.

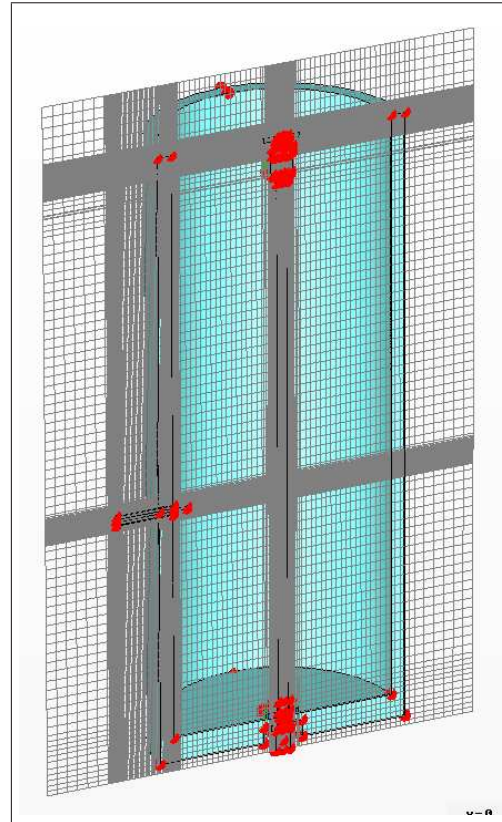


Figure 5.7: CST cut-plane mesh-view of coaxial probe, showing global and localised meshing.

5.1. Only the dielectric bead in the coaxial probe flange needs to be defined locally. The X and Y mesh spacings here, are applied for the whole Z-range of the simulation domain, covering the rest of the central semi-ridged structure, as seen in Fig. 5.7. For the flange bead, X, Y and Z mesh steps are set to 0.1 mm. The global Z-mesh spacing is sufficient for the rest of the semi-ridged structure. For the Y-directed E-field probe, X and Y mesh steps are set to 0.5 mm and the Z-spacing to 0.2 mm. These custom mesh parameters are manually tweaked to achieve S21 result convergence and leads to an absolute mesh cell count of 5.5 million.

5.2.3 Domain and Solver Settings

With the geometry modelled and the mesh parameters set, the two remaining aspects of the modelling process are the domain definition and solver settings. The domain is specified by setting boundary conditions, symmetry planes, background material properties and frequency span. Use is made of the "open add space" boundary definition for all except the lower boundary. This automatically adds a suitable amount of background material between the model and the domain boundary and employs a perfect boundary approximation algorithm to approximate an open space surrounding the coaxial probe. The lower boundary is defined as "Electric" and makes galvanic contact with the outer of the bottom female connector. This is necessary to simulate the connection to the grounded VNA port

via the outside of the VNA feed cable, which is present in the physical system. With an open boundary defined here, this path to ground, which supports the existence of CM-current, is not represented. The background material is specified as Air with permittivity of 1.000589. The model geometry allows the use of symmetry which effectively halves the total amount of mesh elements to 2.8 Million. The frequency span is set from 0 to 3 GHz.

The transient solver uses a time domain (TD) based, FVTD code for solving Maxwell's equations in the simulation domain. A pulse of electromagnetic energy is simulated, entering the domain through one of the ports and the energy levels inside the domain is monitored. When the energy levels inside the domain decay to the user defined accuracy setting, which is the current energy level compared to the original inserted energy level in dB, the solver is stopped and the results are stored. For multiple ports this may be repeated for each port depending on the required results. A multitude of different results can be generated and may include field data at pre-defined frequencies, such as E-fields, H-fields and surface current, or S-parameter and field probe data which spans the simulated band. The solver energy criteria setting influences the accuracy but also the calculation time of the simulation. For the final simulation, an energy criteria accuracy of -50dB is set and the maximum number of pulses setting is increased to 100. This specifies the maximum allowable simulation time in multiples of excitation pulse duration. The aim is for the solver to meet the specified energy criteria level prior to reaching this maximum time limit. Due to the shield cavity, which represents a high Q environment, the energy in the system takes a long time to decay and requires many pulse widths. Most of the other settings are left on default values. The adaptive meshing option is not used, due to the extremely long simulation times involved and the inability of this option to vary locally meshed parts for result convergence. The total simulation time of the final run without symmetry amounts to 47 hrs and with symmetry to about 25 hrs. The simulations are run on an Intel Q6600 quad-core 2.4 GHz machine with 8 GB of random access memory (RAM).

5.3 VNA Field Probing Measurements

5.3.1 Measurement Setup

Fig. 5.8 shows a picture of one of the VNA setups for field probing measurements. In the background the test set of an Agilent 8510 network analyser is visible. Here, S12 is recorded with port two on the right connected to the coaxial probe feed cable below the jig, and port one connected to the E-field probe. Alternatively the ports may be switched and S21 can be recorded for an identical measurement. Two high quality VNA cables are used. Specific care is taken not to exceed cable bending radius and to prevent further mechanical stress, the field probing cable is supported with stacked polystyrene blocks. A jig holding the coaxial probe is clamped to the work bench and provides mechanical stability. Cables, connectors and calibration standards are cleaned according to standard lab practice and suitable torquing is applied to connect components.

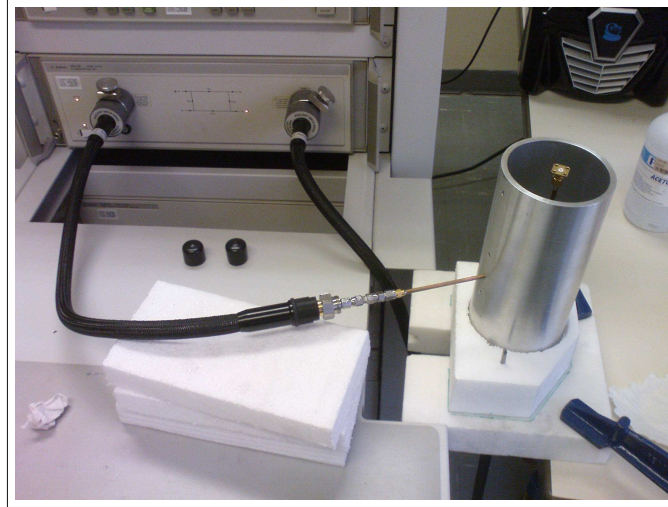


Figure 5.8: VNA field probing: port one feeds the E-field probe and port two the coaxial probe.

Since low E-field levels are probed inside the shield cavity, a high dynamic range measurement strategy is required. Apart from the Agilent 8510 in the figure, a more modern Rhodes and Schwartz model ZVB network analyser is used for verification, and is preferred. It provides a slightly larger dynamic range, due to improved internal isolation between the ports, and has a selectable intermediate frequency (IF) bandwidth. Nonetheless, the obtained S21 data agrees and provides further confidence in results. For the final measurement an IF bandwidth of 10 Hz is selected, averaging is set to 32 and the power level is left on the default value of 10 dBm. For every 10 times reduction in IF bandwidth the VNA noise floor is effectively reduced by 10dB and for averaging a square root dependant noise floor reduction is gained. The VNA is used in "step" mode, which means that it phase-locks onto each frequency point for data acquisition, rather than ramping quickly through the frequency band. This improves frequency accuracy and repeatability, at the expense of measurement time. To reduce measurement time, 32 key frequency points, identified with the aid of simulation results, are entered in a user defined list. To avoid repetition, some measured results are deferred to section 5.3.3 where it is compared to simulation results.

5.3.2 Calibration

For this measurement, a carefully conducted 2-port, Short-Open-Load-Thru (SOLT) calibration is required to remove systematic errors. This is achieved using an Agilent SMA precision calibration kit. For a full two-port calibration, 12 vector error coefficients must be uniquely determined, six for each of the two paths. Fig. 5.9 shows an error-model diagram for the forward path, with the six different errors labeled.

Many published documents, including [36],[37] and [38], provide extensive information about these errors, their effect and removal through calibration. The isolation error is of particular interest in this case. This refers to an error caused by cross-talk between VNA ports, which in the ideal case, would be perfectly isolated. To remove the error the normal

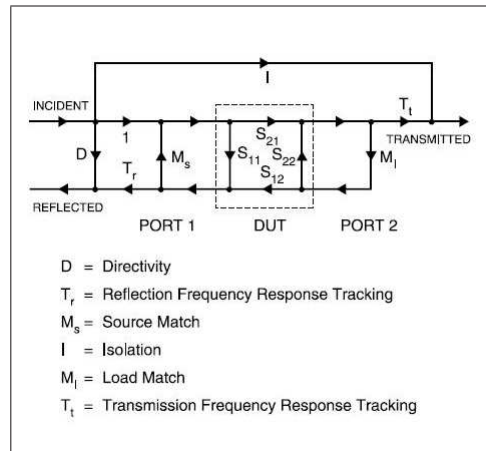


Figure 5.9: Error-model for forward path of full two-port calibration from [7].

method requires two high quality matched loads to be fitted at the calibration planes and the isolation measured. Frequently, the isolation calibration measurement is ignored for less demanding measurement applications, primarily due to the risk of degrading the calibration if the matched loads are not of a suitable quality. Due to the dynamic range requirement for this measurement, the Isolation calibration is implemented and contributes to an overall achieved dynamic range of 100 dB. This is verified to levels of at least -80dB, through the use of a high quality Agilent variable attenuator, connected between the two ports. By having the E-field probe outside the cavity, the noise floor can be seen on the VNA at around -110 dB.

Care is taken to connect the artefact Short-Open-Load (SOL) reflection standards to the VNA cables in a position as close as possible to that when field probing measurements are made. For the case of the thru standard, moving the cables from these positions cannot be avoided and is expected to influence phase results the most. Luckily, phase information is not important for this measurement. All cables and calibration standards are handled minimally and in such a fashion as to avoid transferring hand heat. To minimise drift errors, the VNA is switched on at least an hour prior to measurements and allowed to stabilise. The ambient temperature in the room is fairly stable. As a further precaution, measurements are conducted immediately after calibration and in quick succession.

5.3.3 Measurement

The field investigation of the coaxial probe involves two different measurements. The first probes the spatial distribution of electric fields inside the shield cavity and the second inspects the change in field values with the application of different solid test samples on the coaxial probe. As part of establishing the measurement process and to ensure thoroughness in the approach, a measurement investigation is conducted on the system prior to these measurements. This is presented last. Its aim is to inspect whether low levels of electromagnetic energy can possibly leak through the field-probing ports between the outside of the E-field

probe and the shield wall. Such energy could possibly excite CM-current on the outside of the E-field probe and connected VNA cabling, which can cause measurement inaccuracies.

5.3.3.1 Spatial E-field Probing

After conducting the described two-port SOLT calibration, port one of the VNA is connected to the bottom feed and port two to the side E-field probe. For the first measurement sequence, the E-field probe is inserted at position one and a measurement sweep is initiated. Thereafter this process is repeated for the remaining three positions. Attention is paid to avoid touching and deforming the cables as far as possible. The measurements go fairly quickly due to the limited number of frequency points and take about 3 minutes per field-probing position. Fig. 5.10 and Fig. 5.11 shows a comparison between measured and simulated S_{21} results for field-probing position one and three, respectively. In the figures, the VNA results are shown in red with round markers and the simulated CST results are shown in blue. It is apparent that simulated and measured results match almost perfectly over the band for both positions. A similar agreement is achieved for field position two and four which can be seen in Appendix A.

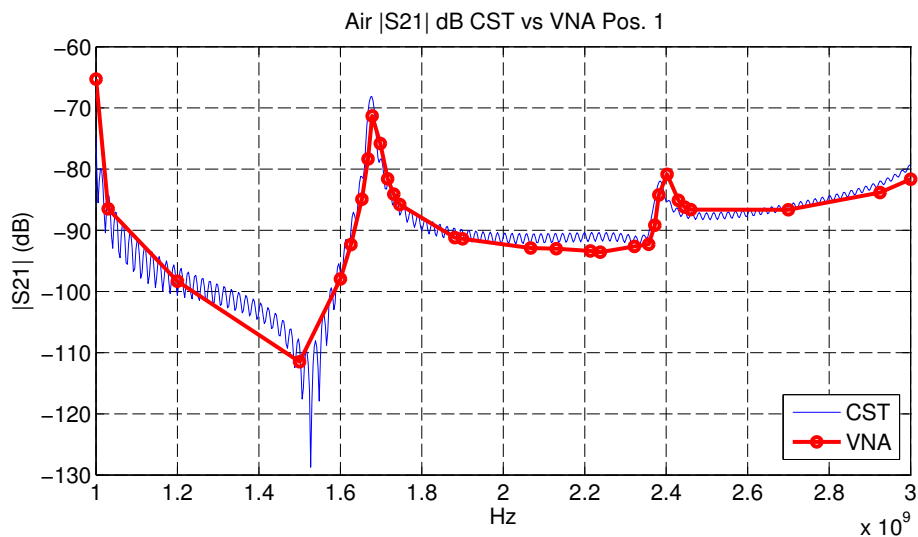


Figure 5.10: CST and VNA comparison of $|S_{21}|$ field results in dB, for position one.

The low S_{21} levels across the band attest to the need for a carefully calibrated, high dynamic range measurement system and justifies the meticulous care taken in the measurement process. The same can be said for the effort in obtaining an accurate CST simulation model. In the results, three resonant peaks occur in the band. The first is just visible at 1 GHz and the second and third occur at 1.67 GHz and 2.38 GHz respectively. The slight ripples in the CST results are due to numeric noise which can be attributed to a finite simulation time and the high Q of the shield structure. With less stringent accuracy settings and a poorly chosen lower domain boundary, this effect is highly amplified. With a sufficient match in

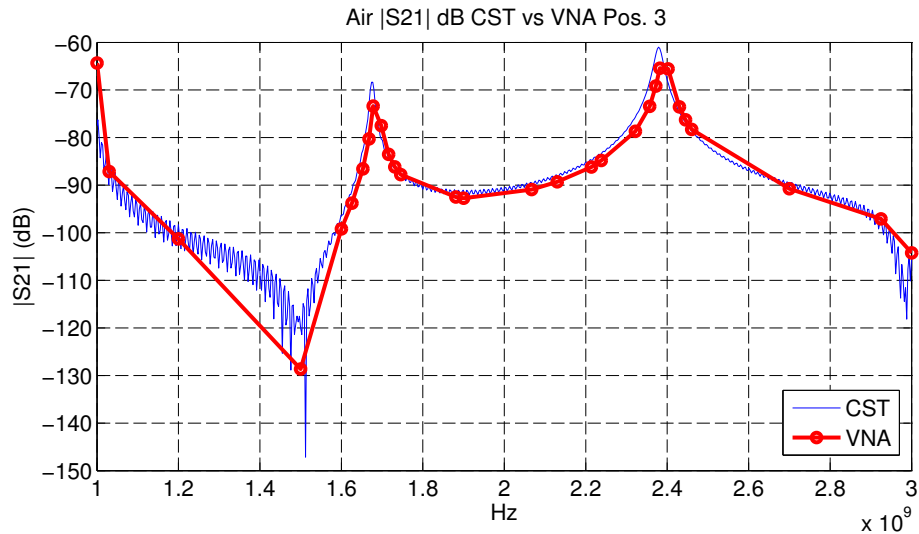


Figure 5.11: CST and VNA comparison of $|S_{21}|$ field results in dB, for position three.

results obtained, the CST simulation model is validated and will be independently used for further investigations of fields and CM-current in the following sections.

5.3.3.2 Effect Of Material Sample On Fields

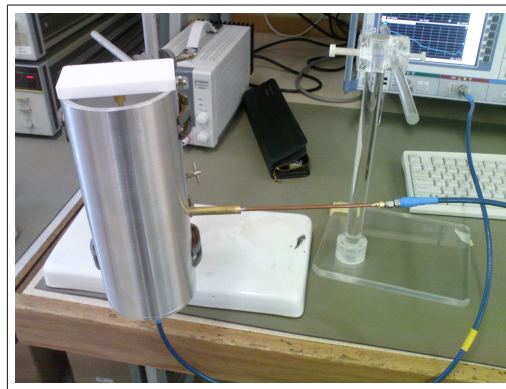


Figure 5.12: Field-probing measurement with Teflon on the coaxial probe face.

Fig. 5.12 shows the measurement setup for the second investigation. A Teflon sample is visible on the coaxial probe face. The E-field probe is kept at a single field-probing position. In this case, position 4, the last position of the previous measurement sequence. Two different solid test samples (Teflon and Rexolite) are placed on the coaxial probe flange and the response measured in turn. Results will indicate whether the presence of a test sample on the probe significantly influences field levels inside of the shielded environment. It is expected that the probed field levels will increase as the permittivity of the test materials increases. This is due to the fact that E-fields are less able to escape through the top probe aperture and are effectively forced below the MUT, into the cavity. A comparison of S_{21}

results for these measurements in dB, are shown in Fig. 5.13. The red plot with markers, which is the same as that in Fig. 5.11, is the response for Air. The solid blue and black, dashed plots represent Teflon and Rexolite respectively.

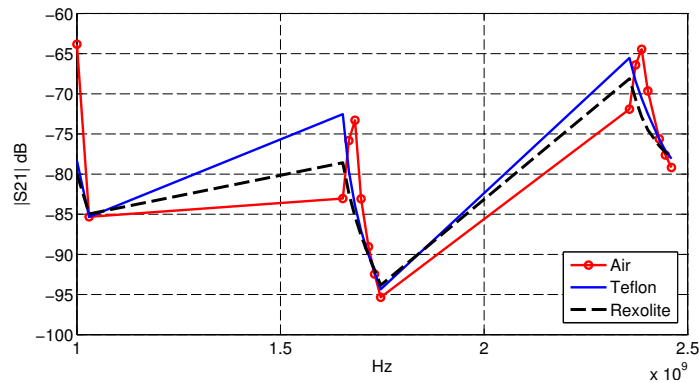


Figure 5.13: Comparison of probed $|S_{21}|$ results in dB for Air, Teflon and Rexolite samples, placed on the coaxial probe.

The probed values for Air are generally the weakest over the measured band. This confirms one part of the original expectation: placing a test material on the probe face definitely influences the field levels inside the cavity. As expected, an increase is seen. However, since Rexolite has a slightly greater permittivity (2.53), compared to Teflon (2.08), the expectation that field values will increase for a sample with higher permittivity seems unfounded. Unfortunately the measured samples are of unequal physical size and do not extend completely over the top shield aperture. Since the greatest difference in field values for the two materials is seen around the two major resonant peaks, this strongly suggests that the physical size of the samples plays a role. For this test to be conducted conclusively, samples of equal size are required. Despite this limitation, the measurement served to establish a greater feeling for the shielded system and confirms an intuitive suspicion regarding field behaviour with a MUT present.

5.3.3.3 System Integrity Check

Initial field-probing measurements, conducted by J. Badenhorst [8], employed an extended centre conductor E-field probe with an added feature. Quarter-wave, Bazooka-type baluns were used to suppress anticipated energy leakage through small gaps that form between the 5 mm shield-wall probing hole and the coaxial outer of the field probe. Such energy could cause unwanted CM-currents to flow on the outside of the E-field probe and connected VNA cabling. Fig. 5.14 shows a bare field probe below one with a Bazooka-type balun. The balun simply comprises a quarter-wave length of open brass pipe with the rear end closed off and soldered onto the copper outer of a semi-ridged E-field probe.

When a probe with balun is inserted, the open end of the balun sits up close to the outer shield wall, but should not make galvanic contact with it. To ensure this, non-conductive



Figure 5.14: E-field probe with and without a Bazooka balun.

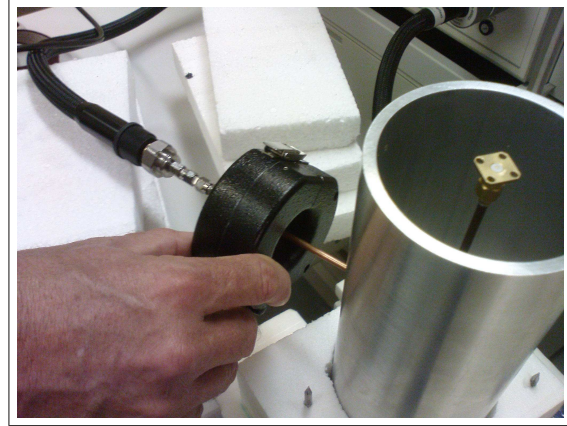


Figure 5.15: EMCO current-probe placed around E-field probe to test for expected CM-current.

tape is placed around the probing holes on the outer face of the shield. According to conventional theory, the balun inner quarter-wave-length structure presents a high impedance path for possible escaping CM energy, preventing it from leaking through the port. The balun is expected to be effective in a narrow band around the designed centre frequency. Whether a balun is really necessary, or effective, was not reported on in [8]. For these sensitive measurements and proper validation of CST models, clarity is desired regarding this issue. Initially, an attempt is made to measure CM-current on the outside of a bare E-field probe in one of the probing positions. This is shown in Fig. 5.15. An EMCO CM-current probe is fitted around the E-field probe and connected to a battery-driven SA. (The use of a non-mains-connected device is important as unwanted pickup loops may be formed.) To address synchronisation problems, the VNA is set to its continuous-wave mode - a single frequency within the band of interest at the declared power of 10 dBm. A small signal is detected on the SA, but after further investigation it is found that this value persists even with the EMCO probe removed. It was later established that energy from the open coaxial probe couples to the outer CM probe exterior and connecting cable. This acts as a monopole to the battery driven SA and the energy enters through the window of its digital display interface.

The only remaining option to evaluate the Bazooka-type balun is to conduct E-field probing measurements, with and without the baluns, to inspect whether any significant change in results can be seen. The two shield resonant frequencies at 1.67 and 2.38 GHz, are chosen as centre frequencies for two respective balun designs. Fields inside the shield peak at these frequencies and any significant leakage should be readily detectable here. For these two frequencies, a quarter wavelength in air is calculated to be 44 mm and 31 mm, respectively.

Fig. 5.16 shows the test results. It is apparent that the baluns do not make any significant difference. No specific changes are seen in the active band of each balun and only a small variation is visible between the plots for the two balun sizes. We attribute this to repeatability in the measurement process. This shows that galvanic contact between the E-field

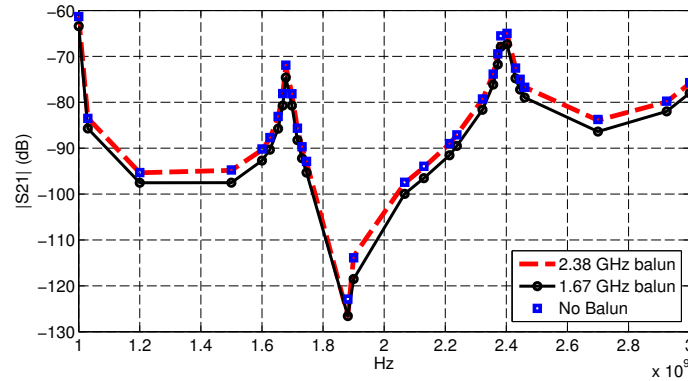


Figure 5.16: Comparison of probed $|S_{21}|$ results at position 4, with and without a balun.

probe and the 5 mm shield wall is sufficient to avoid escaping CM energy on the outside of the E-field probe. Despite not being able to address the interesting issue of whether the Bazooka baluns are effective here, this test addresses the initial concern of the anticipated energy leakage around the field probe.

5.4 Field Discussion

With the CST simulation model verified, use can be made of the extended range of tools in CST for viewing E-fields, H-fields and surface current. Features of the S_{21} E-field probing results can now be better understood in terms of the physics involved. In Fig. 5.17 and Fig. 5.18 two different CST cut-plane views of E-field distributions in and around the shield cavity are shown at 3 GHz. The first shows absolute field strength and is useful to determine where fields are concentrated and what levels escape the system. The second shows vector distributions and helps visualise specific field patterns. It should be noted that both these field plots are shown with the scale clamped to 20 V/m. This makes the low field values inside the cavity visible.

From the two figures, the field distribution seems to follow that of a coaxial structure with a short circuit at one end. The shield inner wall forms the outer conductor and the probe outer acts as inner conductor. Similar field plots at higher and lower frequencies show different coaxial variations. In Fig. 5.18, E-fields within the interior region of the shield are radially directed between the outside of the semi-ridged cable and the inside of the shield wall. Varying the modelled cylinder radius by $\pm 10\%$ does not influence the field patterns significantly, but changing the shield length increases or decreases the number of Z-dependent variations. The three resonant peaks in the probed S_{21} results, described in section 5.3.3.1, shift in frequency as the shield length is altered.

Field probes of four different simulations are super-imposed on the image in Fig. 5.17. By looking at the field magnitude and the positions of the E-field probes, it is evident that probe three is in a region of low field strength compared to others. Accordingly, S_{21} results at 3 GHz for position three should be lower compared to that of position one. Looking back

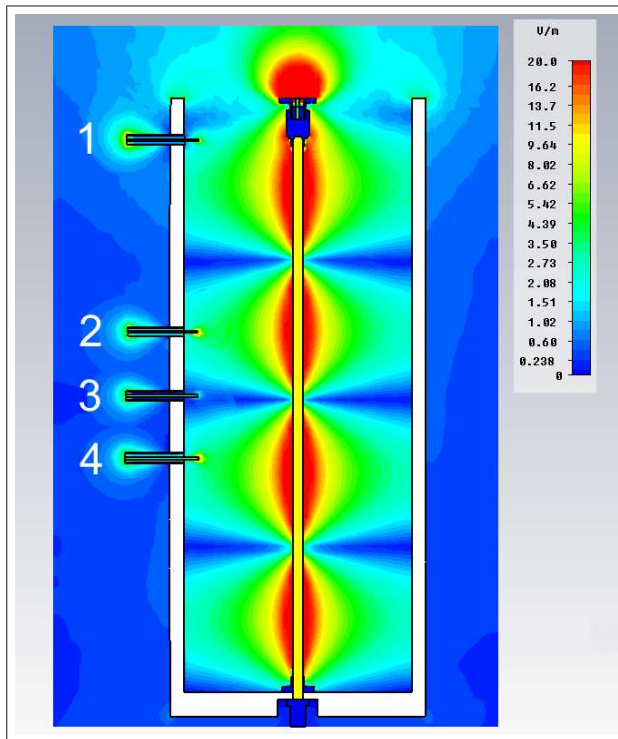


Figure 5.17: Scale-clamped E-field magnitude plot at 3 GHz with four E-field probes superimposed.

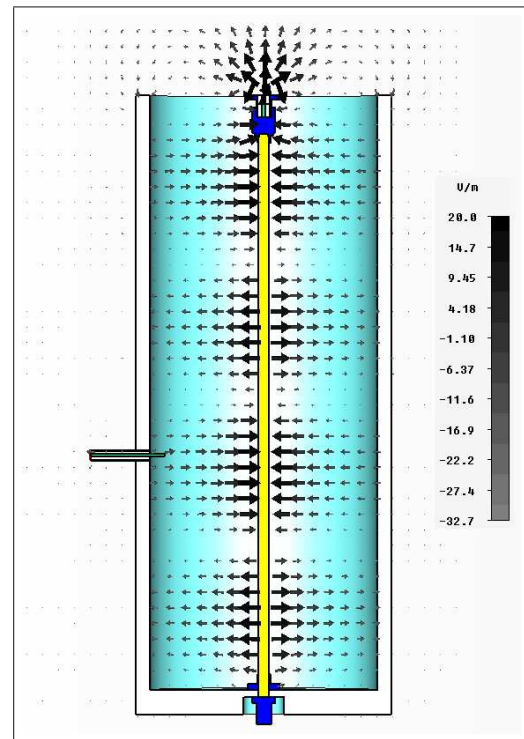


Figure 5.18: Scale-clamped vector E-field plot at 3 GHz with an E-field probe at position 4.

at Fig. 5.10 and Fig. 5.11 this is indeed the case. Position one shows values of -80 dB while position three is somewhat lower at -105 dB. Judging by the vector E-field distributions at the top shield aperture in Fig. 5.18, one could easily be fooled to think that escaping E-fields, terminating on the top and outside of the shield, are of the same order as those retained within the interior fields. This illusion is supported by the clamped scale which is used here for clarity in field visualisation. However, as evident in Fig. 5.17, the stronger fields at the probe face largely contribute towards energy leaving the system in the form of radiation, which is expected. Considering the fields that do terminate on the exterior of the shield and the low field levels around the exterior of the bottom feed port, it is clear that the shield should provide effective isolation at 3 GHz.

5.5 Coaxial Probe Environments

The efforts put into careful measurement and simulation have yielded an in-depth understanding of field behaviour in and around the shielded coaxial probe. This must now be put to good use to contribute towards the improvement of coaxial permittivity measurement systems. The effectiveness of the shield in preventing CM-current on VNA cabling can now be placed into perspective through simulation of unshielded and weakly shielded coaxial probes, using the proven CST modelling technique.

5.5.1 CST models

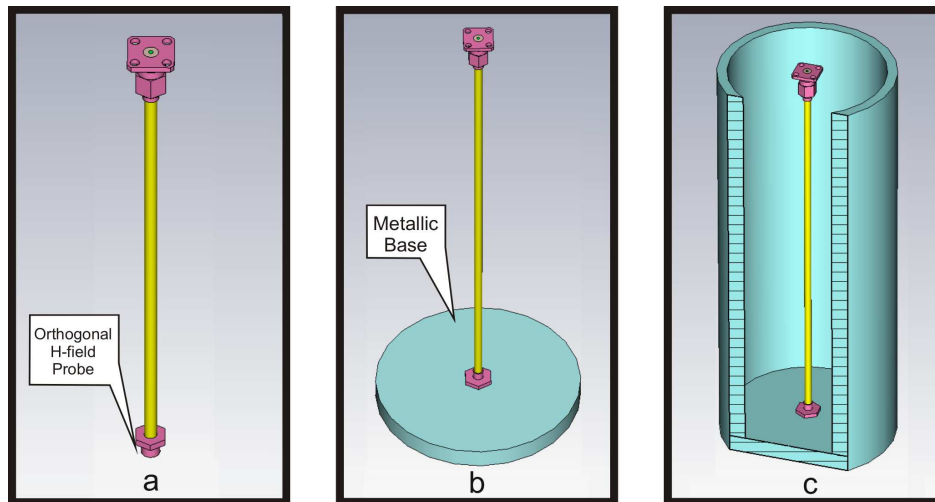


Figure 5.19: Three levels of defined probe environment: a) bare probe: undefined environment; b) probe with shield base only: loosely defined and c) cut-plane view of fully-shielded probe: well defined. a) also shows the placement of the H-field probe for all three cases.

In Fig. 5.19, three probe environments are presented for comparison. The bare flanged probe, shown in Fig. 5.19 a), represents an undefined measurement environment. This specific description alludes to the fact that no mechanism is present to isolate the coaxial probe from arbitrary feed cable lengths. This makes the system vulnerable to unpredictable CM-effects, described in [1]. The same probe with No Shield and just the metallic shield Base, referred to as the NSB case, Fig. 5.19 b), typifies a loosely defined environment. Finally, the fully-shielded case, referred to as the Shield case and shown in Fig. 5.19 c), constitutes a well-defined environment. To compare the effectiveness of these systems in preventing CM-current on the outside of feed cabling, a means of measuring CM-current in the simulations is necessary. CST allows this through the definition of vector H-field probes at point positions. CM-current adheres to Ampere's law and is directly proportional to the strength of orthogonal H-fields close to the conducting structure of interest. In these cases the bottom female connector is used. The position of the H-field probe for all three cases is roughly indicated in Fig. 5.19 a) and lies below the shielding elements of the NSB and Shield models.

5.5.2 Simulation Results and Discussion

Fig. 5.20 shows plots of simulated H-field strength which are used in lieu of CM-current to compare the different environments. As expected, the bare coaxial probe incurs the highest level of CM-current. Its result, plotted in red, shows H-field levels of -30 dBA/m. The loosely defined NSB case, in blue, shows 10 dB lower coupling and the fully shielded case, in black, shows levels of -60 dBA/m or better, apart from resonant features. At these resonant data points the shield is ineffective and CM-current can reach the same levels as the

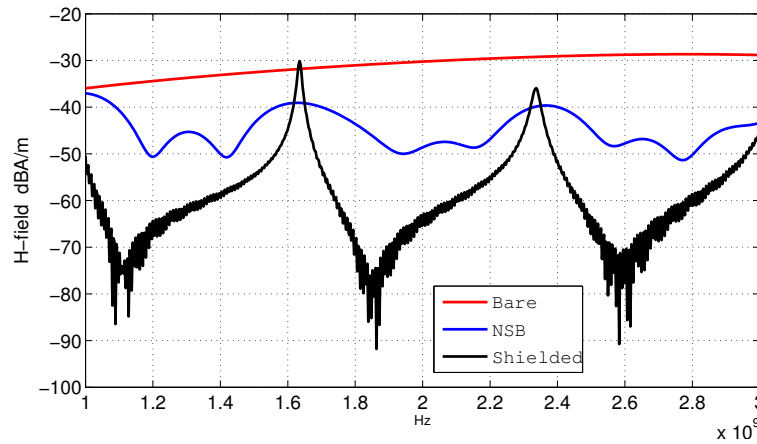


Figure 5.20: Simulated H-field strength (dBA/m) versus frequency for the H-field probe in the three environments, depicted in Fig. 5.19.

bare case. The H-field plot for the shielded case follows a similar trend as the probed S21 results with resonant peaks at the same distinct frequencies. This suggests that CM-current on the outside of the shield is directly coupled to the coaxial field behaviour on its inside. The result comparison indicates that CM-currents, propagating on the feed cable, can be significantly reduced by placing shielding environments around the coaxial probe. Even the simple metallic base of Fig. 5.19 b) improves the situation. The full cylindrical shield has not eliminated the currents at 1.67 GHz and 2.38 GHz, but they are reduced by more than 20 dB across much of the 1 - 3 GHz band. Interestingly, the H-field response for the NSB case shows three weaker, lower-Q, data resonances at the same frequencies as for the Shield case.

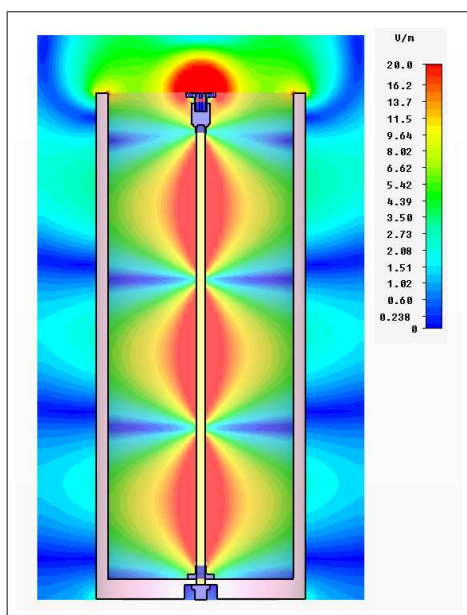


Figure 5.21: Scale-clamped E-field magnitude plot without field probes at 1.67 GHz.

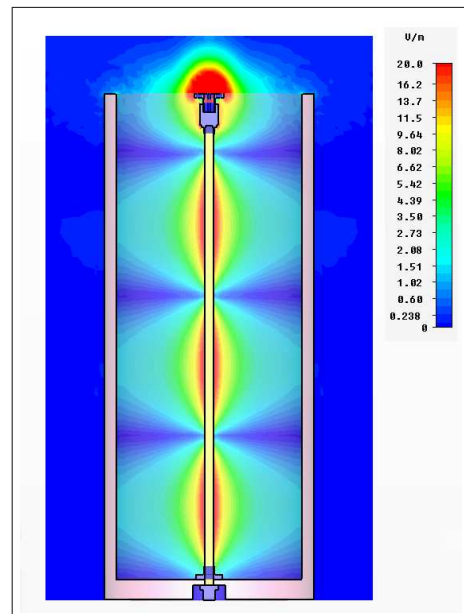


Figure 5.22: Scale-clamped E-field magnitude plot without field probes at 2.5 GHz.

The particular effect of the shield warrants a more specific look at E-fields around data resonant and anti-resonant frequencies in the H-field plot. In Fig. 5.21 and Fig. 5.22 E-field magnitude plots with the same clamped scale as in Fig. 5.17 are shown at resonance, 1.67 GHz and anti-resonance, 2.5 GHz, respectively. These plots, together with the result shown in Fig. 5.20, explain a "balun-like" behaviour of the shield in greatly reducing the problematic CM currents.

5.6 Conclusion

The use of the extended centre-conductor E-field probing technique, in combination with CST, proves to be successful in solving the problem of characterising escaping CM-currents and external fields. This is achieved through meticulous modelling in CST and carefully conducted VNA measurements. In CST particular attention is focused on customised meshing, which, in combination with the domain and solver settings, are used to ensure result convergence. A high-dynamic-range VNA measurement strategy is employed due to the low field levels that are probed. The spatial dependence of shield-cavity fields and the effect of placing a MUT on the coaxial probe is investigated. In addition, an issue with bazooka baluns is resolved. The matching VNA and CST results validate computational modelling and allows simulated field distributions to be trusted. A coaxial field distribution exists on the inside of the shield-cavity and containment of these fields across much of the 1 - 3 GHz band is evident. At resonance the shield proves ineffective at preventing energy leakage and the formation of CM-currents. To quantify the overall effectiveness of a shield to reduce these currents, CST is used exclusively to investigate three different probe environments. Apart from resonant regions the shield provides an improvement of up to 40 dB compared to the bare probe and the NSB case provides up to 20 dB reduction. This investigation provides valuable insight into the behaviour of external fields and escaping CM-current, which was previously unknown, and now begs the question of how this reduction will influence face-plane-calibrated permittivity measurements.

Chapter 6

Material Property Measurements

The study of field behaviour in the previous chapter successfully achieves the initial goal of this work. It characterises CM-current on the exterior of the coaxial probe and suggests viable mitigation methods. This now serves as a pre-cursor for the work presented in this chapter, which takes the investigation a step further. Two questions are asked: To what extent is actual permittivity data affected by the presence of the suggested shielding methods, and can the accuracy of results be improved through the reduction of CM-current? In an attempt to answer these questions, we consider SOL-calibrated face-plane measurements of dielectric solids. In addition to the new knowledge of exterior field behaviour, this investigation is backed by a history of metrology experience with the coaxial probe system. If the effect of reducing CM-energy proves to be significant, it could point to a deficiency in permittivity extraction algorithms that assume an infinite flange radius and hence do not take the escaping CM-energy into account. If not, then the CM-effect can be reported as insignificant and the issue is resolved.

Face-plane simulations and measurements are conducted for the two "better defined" environments, introduced in the previous chapter. The effect of these shielding environments are studied on extracted permittivity results and the system as a whole is evaluated more carefully in terms of escaping energy. In the first section of this chapter the background of permittivity measurements with the current system is explained. Thereafter, the investigative approach is critically evaluated in terms of traceability, leading to a discussion of the strategy which is followed. The investigation starts with a detailed discussion of CST simulations. A new model, based on that for the field simulations, is introduced and modelling challenges are noted. Simulation results for Air are used to derive independent VNA open circuit (OC) calibration coefficients and simulated results for Teflon are deferred to section 6.5.2. A description of VNA measurements follows and covers all the relevant aspects such as the setup, calibration and measurement sequence. Thereafter, extraction of measured and simulated material property data, using two methods, is presented. A relative discussion of these results considers the effect of the shielding environments and a comparative discussion of the two methods considers the absolute accuracy of the system. The aim is to answer

the relevant questions that prompted the investigation. Finally, the chapter is ended in the conclusion.

6.1 System Background

This metrology study continues an ongoing collaboration with the National Institute of Standards and Technology (NIST) in the United States, on material property probes which has been reported in [1]. Measurements are based on established techniques and in this case, specifically make use of inherited calibration hardware and material property extraction software. We carry on using the same coaxial probe system that was used for the field analysis in Chapter 5, which is illustrated in Fig. 5.1. For permittivity measurements, only the bottom feed port remains connected to the VNA and no side E-field probes are used. The two better-defined probe environments, which were previously only simulated in CST for field analysis, are considered. The first is the well-defined, fully-shielded case and the second is the loosely-defined, NSB case. The Shield case is convertible into the NSB case by simply unscrewing the bottom screws shown in Fig. 5.1, and removing the shield. Instead of a two-port calibration with commercial standards, a customised one-port, face-plane calibration is used to establish the measurement reference at the face-plane of the coaxial probe. Permittivity data is extracted from measured results through one of two extraction techniques. The first, referred to as the NIST method, was developed by J Baker-Jarvis and M D Janezic at the NIST laboratories and is based on a full-wave solution of Maxwell's equations. The other is based on the use of CST models in an iterative fashion and is referred to as the CST method.

6.2 Traceability and Strategy

For the field analysis in chapter 5, traceability is easily established. The CST simulation results are validated by comparison to accurate VNA measurements. The VNA accuracy is related to calibration which in turn can be traced to the accuracy of the commercial calibration standards. For this investigation, traceability is not as straight forward and influences the strategy which is followed. To establish the effect of shielding on extracted permittivity is not such a problem since relative results are sufficient. However, commenting on the absolute measurement accuracy of the probe and the validity of the assumptions in the NIST method, is more difficult. This is particularly so since custom calibration standards are required for face-plane calibrations, and the definitions that describe them must be established. Since conclusions derived from this study might have interesting implications, the level of confidence in results must be determined and kept in mind. The previously established SOL calibration for these measurements is based on in-house-manufactured load and short circuit (SC) standards with the bare probe radiating into air for the OC. For the SC and load definitions, negligible inductance and a perfect 50 ohm impedance may be assumed

respectively. For the OC definition, the NIST full-wave solution for the probe geometry is traditionally used to generate S-parameters from which capacitance coefficients are derived. The problem now is that calibration is based on a code that assumes an infinite flange radius and cannot be used to generate results that would allow comment on this assumption. The proposed solution is to use CST to accurately model the whole probe geometry and to simulate the radiated fields for the OC, taking CM-energy into account. But, achieving accurate simulations in CST is challenging and is normally facilitated through carefully calibrated measurements, which brings us back to the original problem.

To progress in solving this problem, we consider what standards are available and how a strategy can be devised to ensure the best results. From experience it is known that current coaxial probe systems are quite accurate in measuring the real part of sample permittivity and that any improvement that might be derived from this work is expected to be small. Split-post resonator techniques provide the best obtainable accuracy for comparison and these are routinely conducted at NIST. It is thus not unreasonable to accept coaxial probe data-sets of ϵ' , measured at NIST or simulated by the NIST full-wave code, as a base to compare to CST results. If due diligence is applied to achieve convergence in CST and results compare well to the NIST data sets, then that provides the best acceptable starting point. In addition, we have trustworthy measurement samples from NIST, despite currently unavailable split-post resonator results. Therefore we can also work the argument backwards and compare inverted permittivity measurements to actual material data.

With these two aspects in mind, an overall strategy is proposed. We use CST to obtain new OC calibration coefficients for the two probe environments and then conduct measurements for the different material test samples, using both the old and new calibration sets. We then use the NIST inversion code and an iterative approach in CST to convert measured S-parameters into complex permittivity. The results can be compared to actual sample permittivity and in this fashion the two independent methods, CST and NIST, can be compared. For the relative comparison the NIST results suffices, but if CST agrees, the case is strengthened. This strategy depends much on the outcome of CST results and even if CST is successful, the argument is not water-tight without split-post resonator results. We conduct this investigation with this knowledge and agree that the available standards are good enough to warrant comment on the outcome, which will determine whether a more thorough investigation is needed.

6.3 CST Simulation

With a strategy devised, and the success of CST proven in the simulation of the coaxial probe for field analysis, the more challenging task of simulating face-plane calibrated material property measurements is undertaken. Since the aim is to include the effect of CM-current and the outer environment, the previous model serves as a base. The extended simulation domain is not truncated to a limited region around the probe-face and MUT interface, as is

common in published reports of these types of simulations [15]. The following subsections discuss different elements of the CST simulation process. The main simulation results are deferred to section 6.5.2 where it is used in the CST permittivity extraction process and compared to VNA measurements.

6.3.1 Simulation Models

The effort that was put into modelling the coaxial probe for field measurements is now put to further use as a base for simulating permittivity measurements. For the field analysis models, the simplifications to the internal structure of the semi-ridged cable, discussed in section 5.2.1, can be tolerated since the results are not phase sensitive. In contrast, for the intrinsically phase-sensitive permittivity measurements, these simplifications are found to be inadequate. This is discovered through initial attempts at obtaining equivalent face-plane calibrated results by applying numerical de-trending. This effectively shifts the bottom simulation port up to the face-plane of the probe. The de-trended port-one reflection coefficient, Γ_{det} , is given by:

$$\Gamma_{det} = \Gamma_{p1} \times e^{j2\beta\ell} \quad (6.1)$$

with β given by:

$$\beta = \frac{2\pi f \sqrt{\epsilon_r}}{c}$$

where Γ_{p1} is the simulated port one reflection coefficient. The relative permittivity of the semi-ridged PTFE bead is taken as, $\epsilon_r = 2.08$, and the exact internal propagation length, ℓ , of the total feed structure is considered. Insertion loss over this length is assumed insignificant.

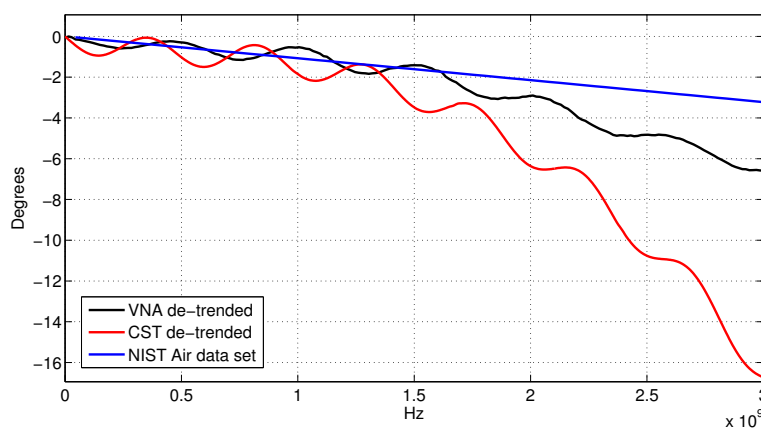


Figure 6.1: VNA and CST full-length de-trended results, both non-linear compared to the desired form of the NIST data set in blue. Dispersion in the semi-ridged bead is suspected to be the cause.

It was argued that the non-linear form of the de-trended CST phase result, shown as the red plot in Fig. 6.1, could be improved by avoiding the simplifications in the semi-ridged

feed structure and minimizing the propagation length. The port was thus synthetically embedded just below the face-plane of the probe within the coaxial structure and the propagation length suitably altered in the de-trending equation. This provided improved results but still did not meet the required phase accuracy. We were now intrigued by the failure of the de-trending technique. Looking back at the original, full-length de-trended results, we realise that the non-linear distortion might not principally be due to higher order modes at the internal simplifications, but due to dispersion in the dielectric bead. This could explain why shorter de-trended results appear to be linear while still not being accurate. We also test de-trending on VNA results from the physical model by calibrating to the bottom SMA port using commercial standards. The result, (black plot), is compared in Fig. 6.1 to the CST de-trended data and the desired NIST data-set for air, (blue plot). The similar, non-linear form supports the dispersion argument.

The use of a CST port function that allows its reference plane to be shifted by a user-specified distance, finally solved the problem. CST accurately de-embeds that section from simulated results according to actual field distributions.

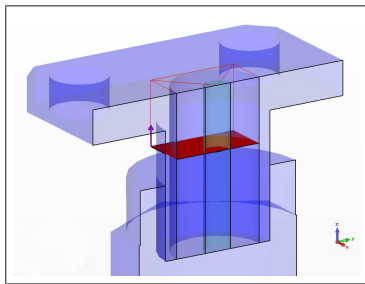


Figure 6.2: Coaxial probe face plane with port reference extension shown.

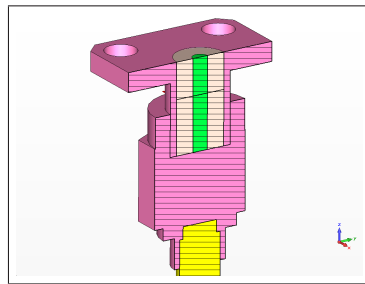


Figure 6.3: Simplification at top connector and semi-ridged cable.

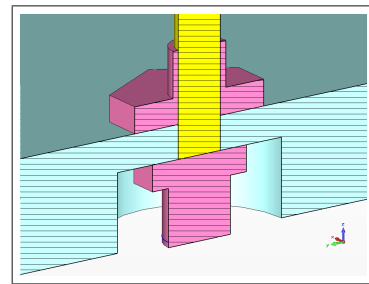


Figure 6.4: Simplification at bottom female connector.

The lessons learnt in the previous attempts of embedding the port close to the face plane are applied in conjunction with this function to obtain suitably accurate phase results. Fig. 6.2 shows the final position of the simulation port and a projection of the CST port reference-extension which is visible as a red outlined box. The port is embedded 3mm below the probe face, inside the coaxial structure of the standard SMA panel mount connector. This distance accommodates higher order TM_{0x} modes [15] that form inside the coaxial aperture at the discontinuity of the probe-MUT interface. The back of the port effectively cuts off the remainder of the coaxial structure below making only the outer geometry necessary. To reduce mesh cells, the top connector and bottom female connector is simplified into solid brass components and the semi-ridged cable into solid copper. This is shown in Fig. 6.3 and Fig. 6.4. The rest of the geometry for the fully shielded and the NSB case remains the same as in the field analysis models.

6.3.2 Meshing

Despite the use of the field analysis model as a base, mesh requirements for permittivity simulations are somewhat different. Fortunately, lessons previously learnt are applicable and ease the process of obtaining suitable mesh arrangements. The concept of localised meshing in key areas is employed and manual adjustment is used again to ensure result convergence. In Fig. 6.5 and Fig. 6.6 a cut-plane mesh-view is shown of the fully-shielded probe, radiating into air, and of the NSB case with a Teflon sample on the probe face, respectively.

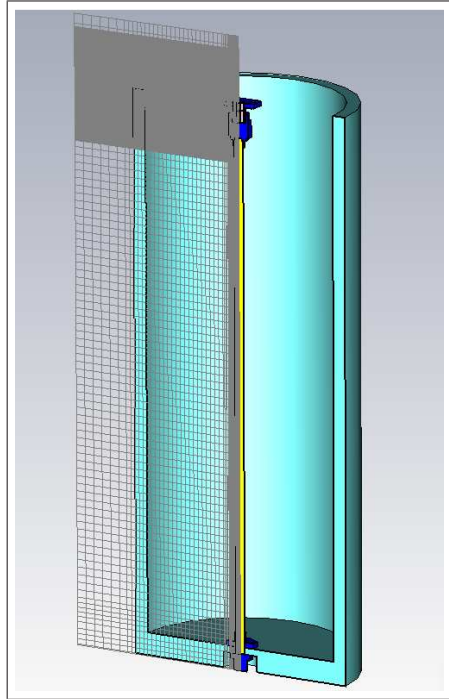


Figure 6.5: Cut-plane view of meshing for the fully-shielded case.

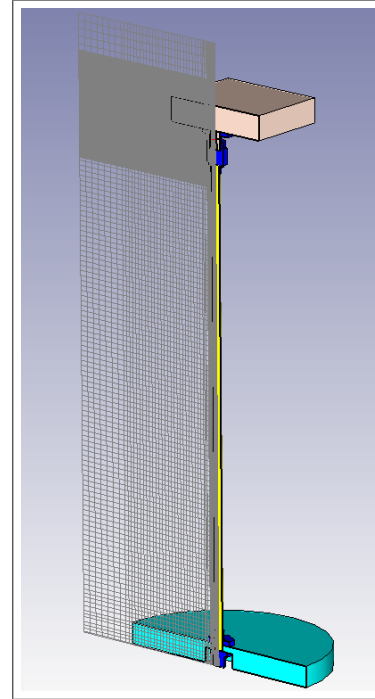


Figure 6.6: Cut-plane view of meshing for the NSB case.

From these macro perspectives it is evident that a finer model discretisation is required in the vicinity of the probe face and that the mesh is divided into two main parts. The coarse part is specified in the global mesh parameters and the finer mesh area is specified through local meshing of the port offset region. This region comprises the upper part of the divided coaxial interior, shown in Fig. 6.7. Initially, a finer mesh was defined here to satisfy CST port requirements, but it was later discovered that the area surrounding the probe face also requires finer meshing. To achieve this, use is made of the option to extend the local meshing parameters beyond the component boundaries. For the localised meshing the Z-range extension, as well as the X, Y and Z mesh spacing is specified.

In Fig. 6.7 the red markers on the mesh denote primary mesh points that are automatically identified by CST. Despite this feature it is still necessary to inspect the mesh and ensure that elements exist at boundaries between components. Should this not be the case, meshing parameters have to be modified. Due to the individual computational demands,

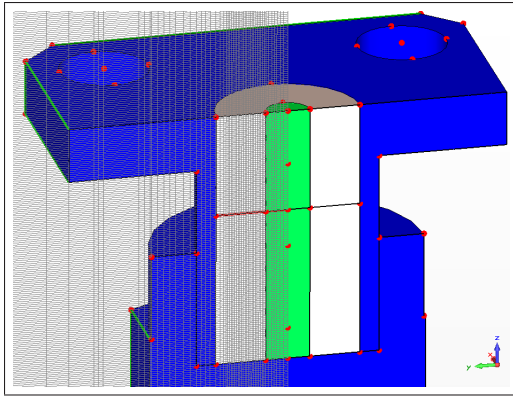


Figure 6.7: Simplification at top connector and semi-ridged cable.

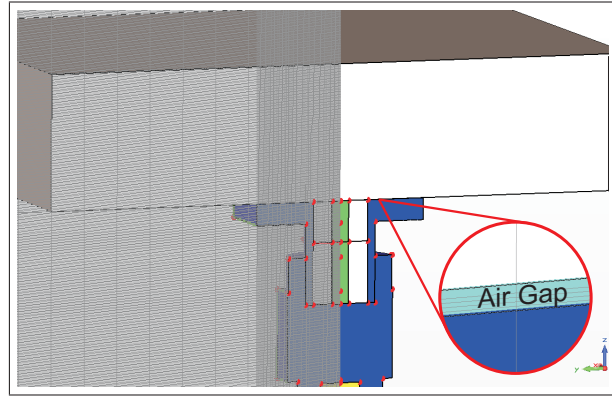


Figure 6.8: Coaxial probe face plane with port reference extension shown.

slightly altered versions of the general mesh layout is used for different probe configurations. To simulate material samples other than air, such as the Teflon sample in Fig. 6.6, a finer and slightly extended local mesh region is required. For the resonant, fully-shielded cases, meshing has to be applied more sparsely due to rapidly increasing computation times. As the investigation progresses, the effect of material sample lift-off becomes of interest. To simulate this, the uneven air gaps are approximated by a uniform air offset of a few micrometres between the probe and the material sample. This is illustrated in Fig. 6.8. The small gap presents some meshing challenges and requires its own, even finer, local mesh to solve these difficulties.

Result convergence is manually obtained due to the long computation times and the ineffectiveness of the automated system in this case. Not surprisingly, global mesh parameters are much less influential than the local mesh parameters. The approach is to increase the total mesh count, using the local parameters, until practical limitations determine the level of result convergence that can be obtained. Two main issues inhibit obtaining further accuracy with the available hardware. The first is the rapidly increasing computation time and the second is the ratio between the smallest and largest mesh element which becomes problematic as the local mesh spacing is reduced. Results that are presented mark the best accuracy that could be obtained.

6.3.3 Domain and Solver settings

In conjunction with meshing, the domain and solver settings determine the accuracy of simulation results. The importance of proper boundary conditions was highlighted for the field analysis simulations in Chapter 5 and here these proven settings remain unchanged. Likewise, the simulated frequency range remains from 1 to 3 GHz and provision is made to simulate for multiple pulse widths. With the absence of a side E-field probe, the model becomes circularly symmetric about the Z-axis and thus quarter symmetry can be considered. This greatly reduces the total number of mesh elements and pays dividends through reduced simulation times. To inspect the integrity of quarter-symmetry boundary condi-

tions, tests are conducted to compare simulated results to that of the same model without symmetry. The outcome confirms that quarter symmetry causes no loss in accuracy while reducing simulation times by up to 75%. It is found that an energy criteria setting of -50 dB is sufficient for all model variations. Tests with values of up to -80dB show insignificant differences. For the resonant, shielded case, accuracy values approaching -40dB start showing numeric noise. In the solver settings dialog box the adaptive meshing option is disabled in concurrence with the customised meshing strategy. Although less significant here, E and H-field monitors, inherited from the field analysis model, remain for analytic purposes.

6.3.4 Open Circuit Coefficients

The first real test of the CST simulation models come with the generation of new open circuit coefficients to support face-plane calibrated VNA measurements. For the OC, the respective models have to simulate the coaxial probe radiating into air. The goal is to achieve simulation result convergence such that the phase values of these S11-parameters are in realistic agreement with those from NIST data. Should this be the case, the CST results are placed on a surer footing and can be used to derive OC coefficients as the first step in the investigation.

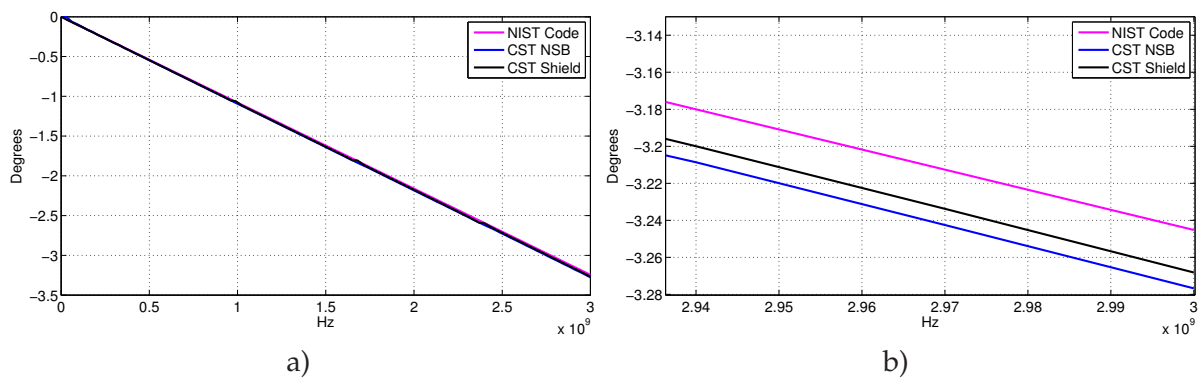


Figure 6.9: a) Comparison of computed OC phase-results and b) Zoomed-in view at 3 GHz. Computed results are from: NIST full-wave code; CST-NSB; and, CST-Shield models.

In Fig. 6.9 a), computed OC phase-results, generated by the full-wave NIST code, the CST-NSB model and CST-Shield model are compared. The small differences are hard to distinguished and in Fig. 6.9 b) a zoomed-in view is shown at 3 GHz. It is clear from the graphs that the CST results compare well to the NIST code and can be used to derive OC coefficients. The coefficients are derived using a technique described in [38], with the effective capacitance of the fringing fields, $C_{\text{eff}}(f)$, given by:

$$C_{\text{eff}}(f) = \frac{\tan\left(\frac{\Delta\phi(f)}{2}\right)}{2\pi f Z_0} \quad (6.2)$$

where $\Delta\phi$ is the simulated phase result for air at each frequency and $Z_0 = 50\Omega$. The Matlab polyfit function is used to generate OC coefficients from a 3rd order polynomial fit of the effective fringing capacitance. The final set of coefficients are shown in Appendix B.

6.4 Face-Plane-Calibrated Measurements

The successfully derived CST OC coefficients and the established NIST coefficients allow face-plane calibrated VNA measurements to commence. In view of the in-house history of face-plane calibrated measurements and the available literature, discussed in section 2.4, these measurements are rigorously conducted with a sense of assurance and a healthy measure of scepticism in scrutinising results.

6.4.1 Measurement Setup

Although face-plane calibrated permittivity measurements do not require the same extended dynamic range as the field measurements, emphasis now shifts to phase sensitivity. Therefore, the majority of measurement considerations centre around this theme. The jig securing the coaxial probe is the same as that used for the field measurements, but mechanical stability is more important. All efforts are made to ensure minimal disturbance to the probe structure and VNA cable during measurements. Flexing and hand warming tests, discussed in [1], are used to inspect the phase stability of various available precision cables. We choose to use an Agilent 8510 VNA, fitted with our best 2.4 mm precision cables, that are both mechanically and thermally phase-stable. Despite the air-conditioned measurement facility, we observe significant VNA phase drift and eventually realise that it occurs in sync with the cycling of the air conditioner. We therefore choose to conduct these measurements without air conditioning, preferably on overcast days or in the early evening when the ambient temperature is more stable.



Figure 6.10: Polishing machine, used to flatten and polish the probe face.

One aspect in the preparation of the probe, not particularly related to phase sensitivity and mentioned in section 2.4.1, is unevenness of the probe face. In this case the centre conductor and bead is slightly retracted from the face-plane level. To solve this problem, the probe face is polished by hand with a polishing machine, shown in Fig. 6.10. (This machine was initially used to test optical end-face polishing techniques on LiNbO₃ crystals.) In-house fabricated discs, covered with silicon carbide paper, is used in decreasing order of grit size until the result is a smooth, even surface. This greatly reduces the effect of sample lift-off which generally plagues solid sample measurements with coaxial probes. Although not formally investigated, the effect of microscopic mechanical flaws due to polishing burr, does not seem to be as significant as suggested in [15]. It is speculated that this polishing technique might limit such flaws.

In preparation for the actual measurements, the VNA is switched on an hour beforehand with cables, connectors and calibration standards cleaned according to standard lab procedure. Material samples are quickly cleaned with ethanol and air-dried to prevent absorption. The correct torque is applied when mating connectors and those more permanently connected are checked. Pre-entered cal-kits are loaded from a stiffy-disk onto the VNA memory and the OC coefficient numbers are spot-checked to make sure. For the final measurement, averaging is set to 128, a band of 1 to 3 GHz is selected and the power level is left on the default value of 10dBm. The VNA is again used in the "step" mode and 51 points are measured.

6.4.2 Calibration

To obtain a reference plane of zero phase and known impedance at the face-plane of the coaxial probe, a face-plane calibration is required. We use a one-port SOL calibration, as introduced in section 6.2 above. Fig. 6.11 shows the load and SC standards.

During calibration these standards were traditionally secured onto the probe face with four 2.5 mm threaded screws, tightened from below the flange into the threaded holes of the brass pieces. This has several disadvantages: 1) when tightening, mechanical knocking is unavoidable; 2) repeatability is difficult; 3) fitting standards takes a long time, increasing phase drift and; 4) the shield obstructs the process. To address this problem we fabricate a clamp, shown in Fig. 6.12, that is similar to one described in [16]. The clamp hooks over the probe face and screw-tightens the standards from the top in a repeatable fashion. The standards are modified with protruding screws that serve as location pins. This can be seen in Fig. 6.12. To improve contact repeatability for the SC standard a thin foam backing and brass foil is used.

It was found that a specific calibration sequence ensures the best results. The 50 Ω matched load is connected first. To ensure a proper connection, its magnitude response is matched to that of a previously established good connection that was saved in the VNA memory using the Data-to-Memory function. This particular response can be seen on the VNA display in the background of Fig. 6.12. The OC is measured next and the SC is mea-

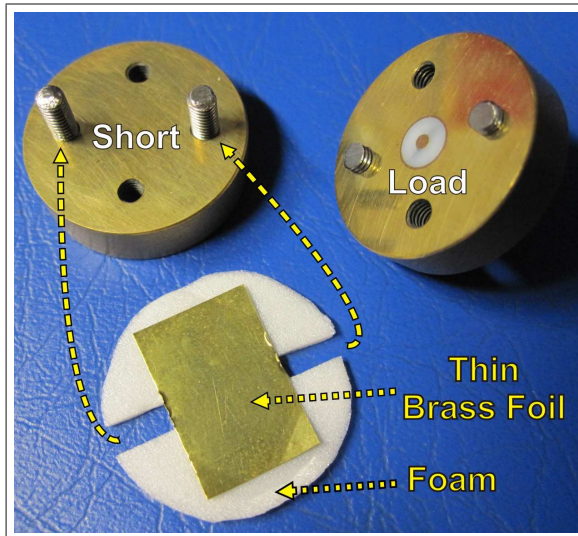


Figure 6.11: Short Circuit with separate foam backing and brass contact foil on the left and Load calibration standard on the back right.

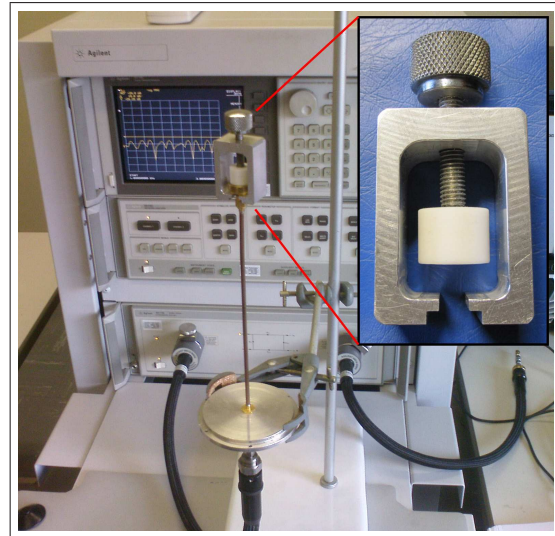


Figure 6.12: Measurement setup with clamp securing Load calibration standard. Data to memory comparison visible on VNA screen.

sured last. This allows the SC connection to be tested directly after calibration by slightly loosening the clamp and re-tightening it to the previous pressure without removing the standard.

6.4.3 Measurement

We measure permittivity samples with three different sets of OC coefficients: 1) the NSB environment with the NIST computed coefficients, hence referred to as the NIST case; 2) the NSB environment with CST coefficients, hence referred to as the NSB case and; 3) the shield environment with CST coefficients, referred to as the Shield case. Measurements are conducted directly after calibration and in quick succession to avoid temperature drift. After the SC standard is removed, a measurement of air is immediately recorded. Samples including Teflon, Rexolite and Perspex are then placed on the probe face and measured in rapid succession while taking care to minimise mechanical probe disturbance. To further limit the effect of lift-off, a 300 g weight is placed on top of the samples. Each sample takes about 2 minutes and S-parameter results are stored on a PC. The session is ended with a final measurement of air, which can be compared to the first to determine phase drift during the sequence. Table 6.1 lists measured phase-drift for the three coaxial probe setups.

Table 6.1: Final measurement phase drift at 3 GHz.

Measurement	Initial air phase	Final air phase	Phase drift
NIST	-3.244°	-3.279°	0.035°
NSB	-3.266°	-3.287°	0.021°
Shield	-3.226°	-3.25°	0.024°

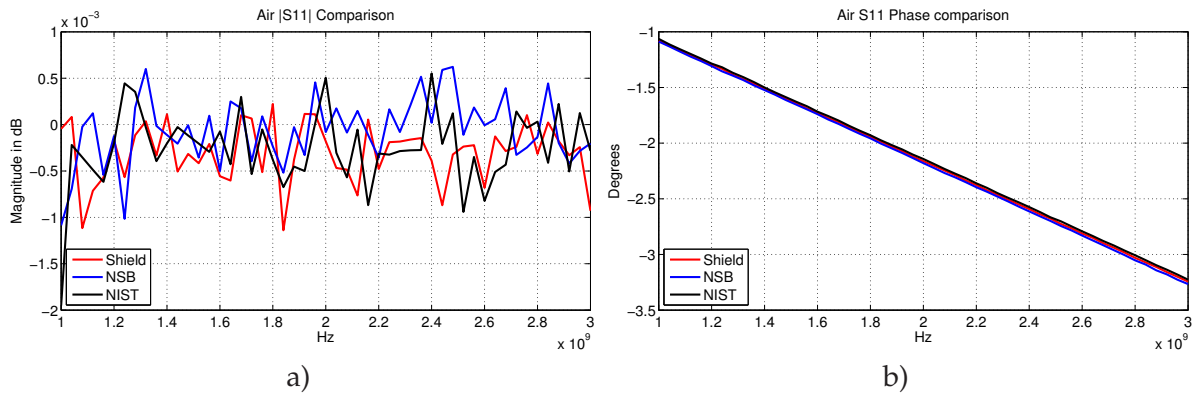


Figure 6.13: a) Measured $|S_{11}|$ in dB and b) S_{11} phase in degrees for Air. Result comparison for: Shield, NSB and NIST probe environments.

Fig. 6.13 a) and Fig. 6.13 b) shows Air magnitude and phase results for the three respective probe configurations. An indication of a good calibration is an Air magnitude result that stays negative. Due to the small numbers involved this is difficult to obtain, but most of these numbers are close with some peak excursions slightly above zero. The linear phase results show little difference between the probe configurations on this scale.

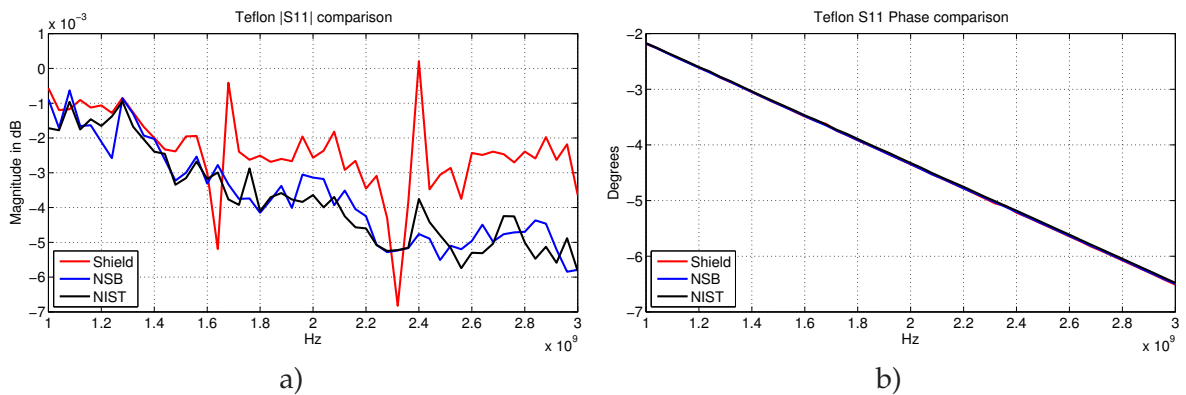


Figure 6.14: a) Measured $|S_{11}|$ in dB and b) S_{11} phase in degrees for Teflon. Result comparison for: Shield, NSB and NIST probe environments.

Fig. 6.14 a) and Fig. 6.14 b) shows a similar magnitude and phase comparison for one material sample, Teflon. A few interesting traits are apparent. In the magnitude result the

red plot for the Shield case shows two distinct resonances at 1.67 and 2.38 GHz and on average, a higher reflection coefficient. The other results, NSB and NIST, lie close together. As with Air, the phase results do not show much differences on this scale but, when zooming in on the same two resonant frequencies, small deviations are visible for the Shield case. Compared to the measurements for Air, we see a greater loss in the magnitude response and an increased phase offset. This concurs with the higher dielectric loss and permittivity, respectively, of Teflon compared to Air. Measured S-parameter results for the other test samples are similar. A presentation of extracted permittivity results and comparisons are provided in section 6.5.1. Here, these results suffice to illustrate the form of the raw VNA data, prior to material property extraction.

6.5 Material Property Extraction

The next step in the proposed strategy involves extraction of complex permittivity data from measured S-parameter results of the dielectric samples. Two methods are considered: the established, full-wave NIST extraction algorithm, described in [1], and an iterative approach in CST. We are interested to see the relative effect of the shielding environments on extracted permittivity and to compare the accuracy of the two methods. This would allow commentary on the NIST extraction code that does not take escaping CM-energy into account as CST does.

6.5.1 NIST Extraction

The NIST full-wave extraction algorithm computes complex permittivity results at discrete frequency points. While assuming an infinite flange radius, the code allows specification of the probe geometry by defining its centre conductor radius, outer conductor inner radius and complex bead permittivity. In addition, sample thickness, surrounding air permittivity and the number of higher order modes that will be considered in the computation must be entered into a text file. Table 6.2 lists the parameters that are used for this investigation.

Table 6.2: Parameters used for the NIST inversion code.

Parameter	Value
Centre conductor Radius	0.640 mm
Outer Conductor Inner Radius	2.086 mm
Air Gap	0 μ m
Sample Thickness	various
Bead Permittivity	2.08 - j0.0008
Air Permittivity	1.000589 - j0.0001
Number of Higer Order Modes	10

Extraction of 100 frequency points with an accuracy of ten higher order modes takes about half an hour on the same PC used for the CST simulations. Of the various solid dielectric samples that were measured, including Perspex, Macor engineering ceramic and compressed Polystyrene, the Teflon and Rexolite samples originating from NIST, provide the best reference. Extracted permittivity results are thus presented for these two materials. Fig. 6.15 and Fig. 6.16 shows extracted real and imaginary permittivity results for Teflon and Rexolite respectively. Each figure compares results for the NSB, NIST and Shield cases.

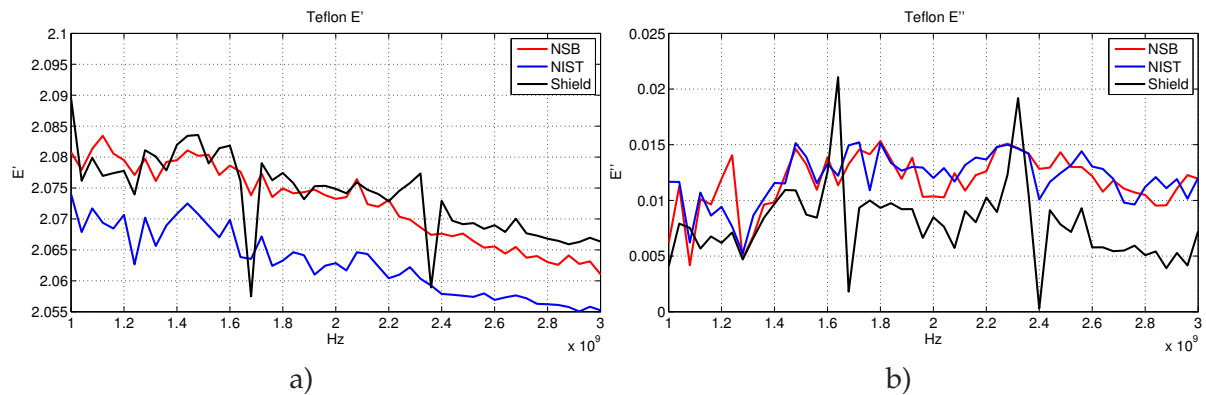


Figure 6.15: a) ϵ' and b) ϵ'' for Teflon from: NSB data with CST-derived OC coefficients for VNA calibration; NSB data with NIST-coefficients; and, Shield data with CST-coefficients.

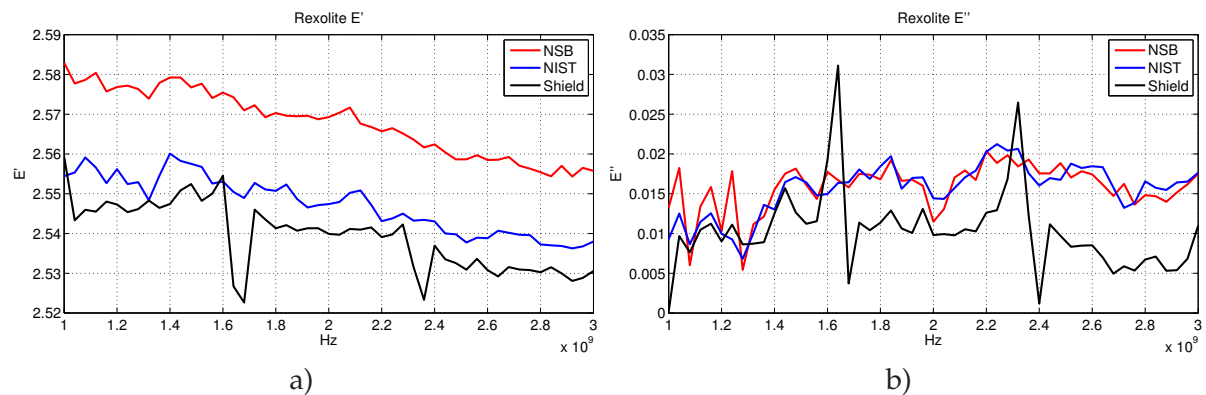


Figure 6.16: a) ϵ' and b) ϵ'' for Rexolite from: NSB data with CST-coefficients; NSB data with NIST-coefficients; and, Shield data with CST-coefficients.

Both ϵ' and ϵ'' show distinct resonances for the Shield case. These relate in frequency to the characteristic peaks of the measured S-parameters, shown in 6.14 a) and the resonant peaks of the S21 field-analysis results in Chapter 5. On this amplified scale, the ϵ' NIST traces for both materials are slightly lower than the NSB traces, whilst the shield result is higher in one case and lower in the other. We conclude that for ϵ' , the experimental repeatability and MUT-probe contact explains these slight differences. The accuracy of ϵ' after polishing the probe is much improved compared to earlier work. Results for the Teflon sample were

previously closer to 1.9, which implied a lift-off of approximately $50 \mu\text{m}$. With the flatter flanged-probe-surface and more detailed calibration schemes, the mid-band permittivity seen here is between 2.06 and 2.075. This is close to the often-quoted number of 2.08. The frequency slope is also less pronounced. Similar comments hold for Rexolite which has reported ϵ' values of around 2.53.

For ϵ'' the shielded case consistently shows lower levels compared to the unshielded NSB and NIST cases. Despite the value being closer to the expected ϵ'' of around 0.0008 for materials like Teflon, there is still an order of magnitude difference. This is common for low-loss measurements with current reflection type systems that generally perform better for higher loss materials such as mineral ore samples, suitable for RF heating.

6.5.2 CST Extraction

Extracting measured permittivity results is possible in CST if an accurate simulation model is available. This can be achieved by sweeping the complex sample-material permittivity in the simulation until results match the measured S-parameter magnitude and phase. First, ϵ' can be varied to match the phase response, then ϵ'' can be varied to match the magnitude response. The initial success achieved in simulating air for the OC coefficients suggests accurate CST models and boded well for the simulation of material sample measurements. However, results for solid samples deviated significantly from measured results. This was found to be caused by sample lift-off during measurements and also explained the accuracy obtained for the OC results. Much time and effort were spent in CST to attempt simulation of the lift-off effect with some of the simulations for the shield case taking up to 65 Hrs. This proved to be futile, since lift-off gaps vary and cannot be measured, leaving two unknowns to match the phase in CST: the sample permittivity and the air-gap thickness. It seemed that the CST method would remain infeasible until the lift-off problem could be addressed.

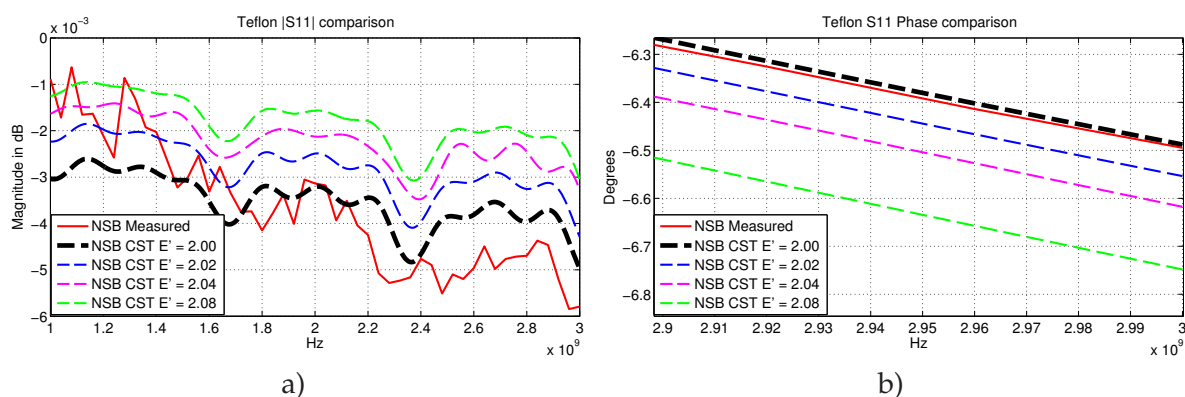


Figure 6.17: CST iterative matching a) ϵ' and b) ϵ'' for Teflon.

This was the case near the end of the investigation when the polishing technique, described in section 6.4.1, finally solved the lift-off problem and alleviated the need for air

gaps in simulations. Fig. 6.17 illustrates varying ϵ' in the CST-NSB simulation to match measured NSB results for the Teflon sample. Unfortunately, due to extended simulation times and time constraints, only one iterative simulation sequence could be conducted for inclusion in this thesis.

Since ϵ' is sensitive to phase, the results in Fig. 6.17 b) should be considered first. The solid red plot shows the measured phase result for Teflon and the dashed lines, starting with green, shows CST phase results converging to the measured result with ϵ' swept at 0.02 increments. At $\epsilon' = 2.00$, the phase result matches within 0.007° at 3 GHz. This number is placed into perspective when considering the 0.021° phase-drift that is stated in table. 6.1 for the NSB measurement. Interestingly, in Fig. 6.17 a), the magnitude result also changes despite being insensitive to ϵ' . This is because the loss tangent, $\tan \delta$ given by:

$$\tan \delta = \frac{\epsilon''}{\epsilon'} \quad (6.3)$$

is defined instead of ϵ'' for lossy materials in CST. Thus, with a fixed value of $\tan \delta$, both the magnitude and phase result should change when varying ϵ' . Reassuringly, the CST magnitude response immediately converges to the measured result without having to change the initial loss tangent of 0.0004. This value is chosen for the first iteration as it is defined for PTFE(lossy) in the CST library. With the S-parameter results closely matched, extracting ϵ' and ϵ'' is somewhat complicated by CST. The specified permittivity and loss tangent is not applied as a constant across the frequency band, but rather as a mid-band point in a "constant tan delta fit" of a Debye dispersion model [35]. This generates frequency-dependent complex permittivity values that are used for the sample in the simulation. In Fig. 6.18 a) and Fig. 6.18 b) the CST-fitted ϵ' and ϵ'' values for the matching results are given respectively. Considering the small scale, ϵ' can be viewed as constant at 2.00 and for the more sensitive ϵ'' , values range between 0.00064 and 0.0008.

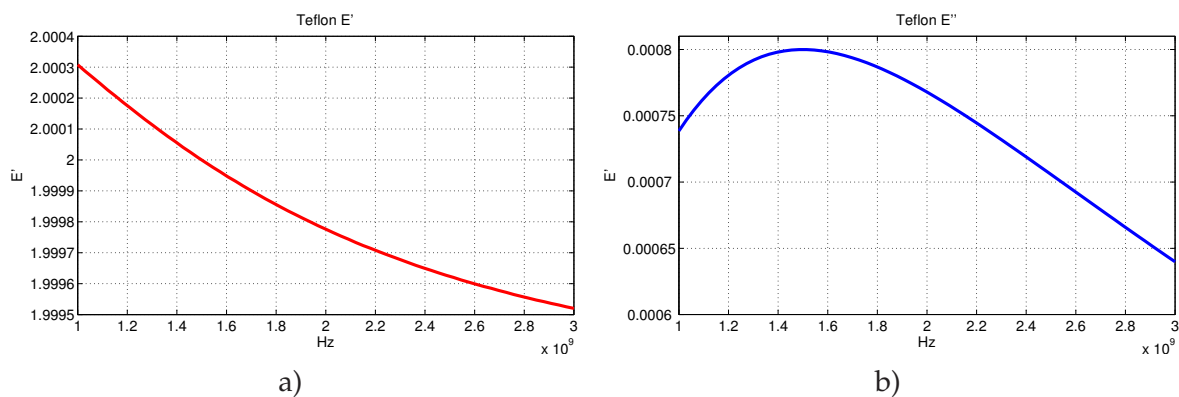


Figure 6.18: CST extracted permittivity for NSB-measured Teflon sample with: a) ϵ' and; b) ϵ'' .

Apart from the matching levels in the magnitude response of Fig. 6.17 a), we also notice a more subtle trait in the measured result that was previously missed. The clear resonances in the CST data exposes the same form in the measured result, which when seen in isolation,

are hidden by small variations on a similar scale. The resonances are similar to those for the NSB case in the external H-field results of the CST field analysis, shown in Fig. 5.20. It is clear that this late, but welcome, success of the CST method affords a more complete discussion of results, as was hoped for in the proposed strategy of section 6.2.

6.6 Discussion

The measured permittivity results, presented for the two extraction methods, finally warrants a discussion on the issues that motivated this investigation. The ensuing discussion centres around two related parts: a relative discussion of NIST and CST results to consider the effect of the probe environment on extracted permittivity, and a comparative discussion to comment on the accuracy of the NIST extraction algorithm that assumes an infinite flange radius.

6.6.1 Effect of Shielding on Permittivity

The fact that the coaxial probe environment influences extracted permittivity was reported in [1] and sparked the initial interest in the issue of escaping CM-energy. The small detected permittivity perturbations were random, due to exposed cable configurations in effectively "undefined" environments, covering the CM-issue in some uncertainty. A way was needed to reproduce CM-perturbations in an isolated metrology setting. This is what we aimed to achieve with the defined shielding environments, which as a bonus, inadvertently amplified the perturbations. This is seen in the NIST-extracted permittivity results of Fig. 6.15 and Fig. 6.16, where the strong resonant features in ϵ' and ϵ'' for the Shield case are due to shield-cavity modes. When the shield is removed to form the NSB case, these resonances seem to disappear in the NIST results, but, as revealed by the CST-NSB simulation data in Fig. 6.17, they are still present in the measured S-parameters. The disappearance of these resonances in the NIST results is attributed to the sensitivity of the NIST extraction to small data-variations, which overshadows more gradual traits like the NSB resonances. The insignificant effect of the shielding environments on the general level of ϵ' is underpinned by the fact that the NIST and CST-calibrated results for ϵ' match within experimental repeatability.

For ϵ'' , the Shield case consistently shows lower levels compared to the NSB and NIST cases. As ϵ'' is sensitive to the amplitude of the S11 data, this is attributed to the reduced energy loss in the well-defined Shield environment. In other words, this difference is a measure of the unaccounted energy that escapes the semi-defined NSB case, compared to the Shield case. What is more, we know that even the Shield case is not immune to some energy loss. It is thus apparent that the elusive CM-energy which is lost in the system, significantly affects extracted permittivity, and should be considered more carefully. With this in mind, a discussion of the differences between the NIST and CST-extracted results follows.

6.6.2 Comparison of Extraction Methods

The form of the NIST and CST-derived complex permittivity for the NSB-measured Teflon sample is somewhat different. Both methods employ the technique of iteratively matching the forward problem for the probe geometry to compute the complex permittivity. The NIST algorithm does this automatically for each discrete frequency of the measured S-parameters, which means that results reflect variations in the measured data. CST, on the other hand, produces a constant tan delta fit, as explained in section 6.5.2 for a manual match of the S-parameters. Notwithstanding this, a comparison of the two techniques can be made and is shown in Fig. 6.19 a) and Fig. 6.19 b) for ϵ' and ϵ'' respectively.

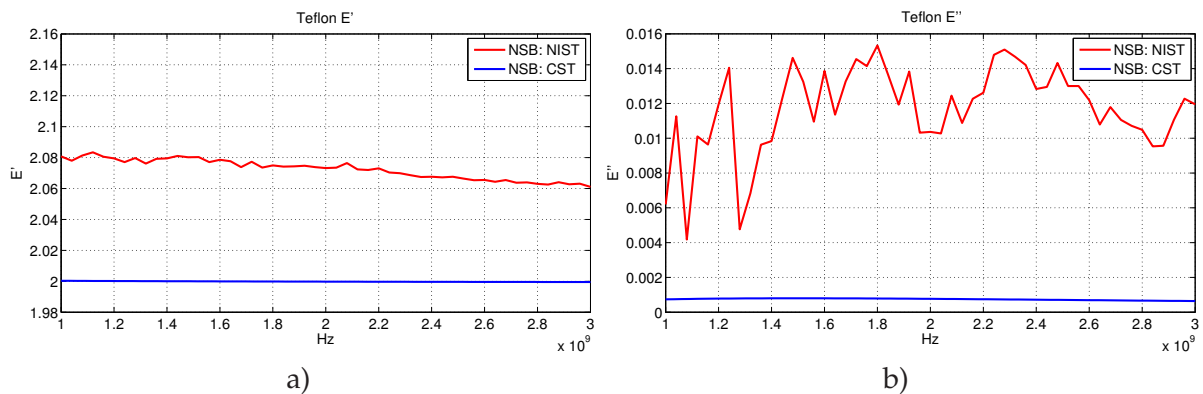


Figure 6.19: Comparison of NIST and CST permittivity extraction for NSB-measured Teflon sample: a) ϵ' and; b) ϵ'' .

For ϵ' , the NIST code predicts a value close to 2.08 while CST converges to a value of 2.00. Industry quotes the value for Teflon most often as 2.08, but 2.00 is not far off considering the unrefined CST extraction technique, employed under time constraints. From the relative discussion in the previous section, the comparison for ϵ'' should be quite interesting and this is indeed the case. The NIST algorithm reports values ranging from 0.005 to 0.015 across the band, while CST predicts values ranging from 0.00064 to 0.0008 which matches the correct value for Teflon at around 0.0008. This is simply the best ϵ'' accuracy that we have obtained for low-loss dielectric measurements with the coaxial probe system, and represents potentially significant metrology implications. The result proves the original suspicion that escaping CM-energy hinders the accuracy of the NIST algorithm in some way. Unsurprisingly, we now know for certain that it is ϵ'' that is most affected. With the unrefined CST result we already gauge the potential accuracy that can be achieved, but it is evident that more time should be spent to cement this matter.

6.7 Conclusion

The work in this chapter is started with the clear goal of taking the field analysis of Chapter 5 a step further, by addressing the CM-effect in face-plane calibrated permittivity measurements. We are specifically interested in the relative effect of the respective shielding environments, NSB and Shield, and the absolute accuracy of the coaxial probe system. Starting out, we face some traceability issues and have to consider the available standards to devise a workable strategy. CST is chosen as an independent extraction method to compare to the NIST method. The NIST method liberally assumes an infinite flange radius, and does not take escaping CM-energy into account. Work is done in CST to obtain accurate models and to derive new OC coefficients for an independent VNA calibration. The established calibration method and standards are critically evaluated and improved. Likewise, the probe face is flattened to significantly reduce sample lift-off. Accurate face-plane measurements of material samples then ensue and permittivity is extracted using both methods.

A relative result comparison indicates that the shielding environments directly influence extracted permittivity. Shield-cavity resonances and less prominent NSB resonances appears in ϵ' and ϵ'' data, but are predictable. By tolerating these known resonances, the situation of a completely exposed probe, where unpredictable resonances stem from exposed cabling, can be improved. With uncontrolled environments, unexpected features in the final material properties will certainly be present. Although ϵ'' is slightly lower for the Shield case, showing a 60 dB out-of-resonance reduction in external CM-current, some energy still escapes. It is apparent that no form of shielding can significantly enhance the accuracy of NIST-extracted results.

A comparison of NIST and CST-extracted permittivity for Teflon, finally allows formal commentary on the NIST method and its infinite-flange assumption. As expected, NIST results show accurate values for ϵ' , while ϵ'' is out by at least an order of magnitude. The unrefined CST results predict a realistic value for ϵ' , but more importantly, gives an accurate value for ϵ'' . This proves that the NIST assumption, which does not account for escaping CM-energy, is invalid for low-loss dielectric samples and that the issue should receive further attention.

Chapter 7

Conclusion

In this work, a rather peculiar path is taken to solve an elusive problem. The problem is that of characterising CM current-leakage and resulting perturbations in measured data sets of coaxial permittivity probes. A literature survey is conducted to gain perspective on this problem, but also to find out more about optical E-field probes. This is considered in a first approach to characterise external E-fields surrounding the coaxial probe. An integrated, Mach-Zehnder-type, optical E-field sensor, based on LiNbO₃ crystal as a sensing element, is chosen. After finalising a complete design in optical simulation software, work on manufacturing begins. This approach is eventually ceased when manufacturing difficulties start overshadowing the actual CM problem. Attention shifts to the use of a two-port probing technique which successfully validates CST modelling of the coaxial probe. Field monitors in CST are used to inspect field distributions and external CM currents for various simulated probe environments. It is found that exterior currents, getting onto VNA cabling, can be significantly reduced by placing a shielding environment around the probe.

With external E-field distributions and CM currents characterised, the investigation is extended to face-plane-calibrated permittivity measurements of dielectric solids. CST simulations are used to support calibration of independent VNA measurements for various probe configurations and permittivity is extracted using both CST and the established NIST extraction method. The behaviour of the shielding environments are seen as resonances in ϵ' and ϵ'' and it is found that no shielding method can significantly improve NIST-extracted results. Undefined measurement environments exposes VNA cabling to CM currents and unexpected features will appear in material properties. This situation can be improved by applying a shielding method and tolerating the known resonances. Concerning the NIST extraction algorithm, CST-extracted results prove that the assumption of an infinite flange radius is not applicable for low-loss dielectric measurements. Escaping CM energy should be considered more carefully for coaxial probes, which can potentially deliver very accurate broadband ϵ'' results. Despite difficulties that stemmed the development of an optical sensor, the goals of this investigation was met and taken a step further in the process. This was achieved through hard work, determination and contributions by many individuals.

7.1 Recommendations

Several general comments and recommendations are warranted by this work. The metallic shield around the measurement environment proved to be an affective tool. In this case, it isolated the experiment, facilitated the two-port probing technique and inadvertently amplified the effect of the external environment in a predictable fashion. This technique might be useful in future metrology studies on similar systems. Optical E-field sensors present several advantages to the field of HF engineering and might be a worthwhile investment when such devices become more affordable. For material property measurements with coaxial probes we definitely recommend a defined probe environment, like the NSB case, to prevent random cable effects. Due to time constraints, the CST-extracted results presented in this thesis were derived with a slightly coarser mesh setting. This influences ϵ' most and will probably account for the slightly less accurate value of 2.00 for Teflon. In addition, the S-parameter matching was manually achieved by visually comparing the plots. It is recommended that more time should be spent to run proper CST simulations, that a method should be developed to automatically match results within some accuracy threshold and that split-post resonator results should be obtained for the measured samples. Combined with a full uncertainty analysis, this would significantly improve the value of results and would make a formal recommendation to NIST possible. The successful use of CST as an extraction method also has other implications. Traditionally, institutions like NIST invested time and money in developing proprietary, full-wave extraction algorithms to deliver a service of conducting permittivity measurements to industry. Now it is proven that any institution with access to CST or similar software, can construct their own permittivity measurement system at minor cost, and achieve accurate results.

Appendices

Appendix A

Other S21 Field Results

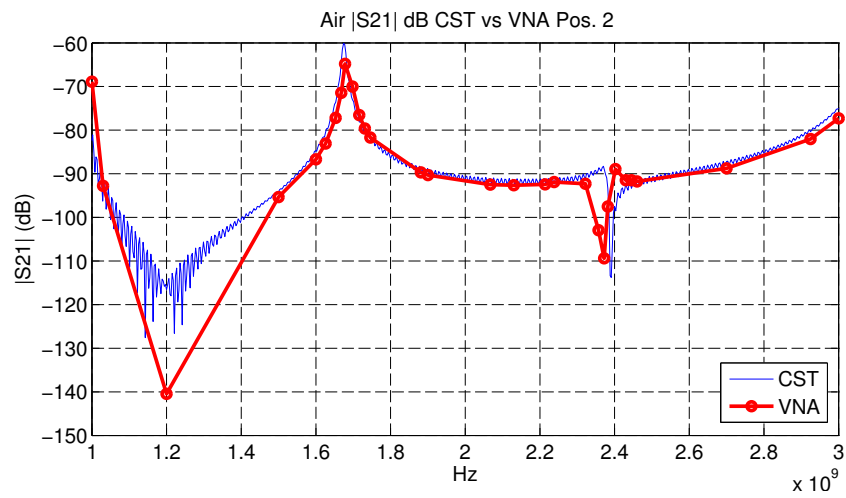


Figure A.1: CST and VNA comparison of $|S_{21}|$ field results in dB, for position two.

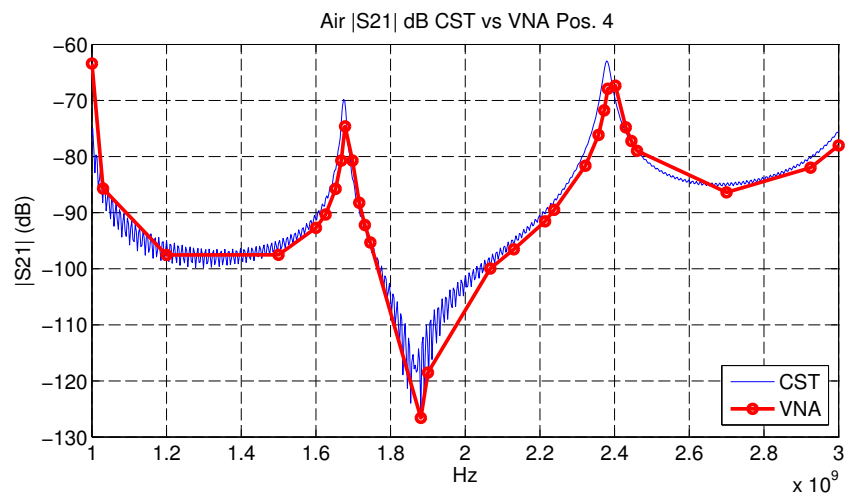


Figure A.2: CST and VNA comparison of $|S_{21}|$ field results in dB, for position four.

Appendix B

CST and NIST OC Coefficients

Calibration Coefficients (1-3 GHz) for final measurement

CST: AIR KDP shieldbase 0.05XY Z-range 20mm (No Shield only the base -80dB run)

C3 35.8330200378036e-45

C2 -197.790025656580e-36 Cal kit on disk : CK_SPNSB2

C1 314.636029906050e-27

C0 30.2041547983530e-15

CST: Air base KDP 4M cells (With Shield) run 50hrs

C3 26.2572443744218e-45

C2 -121.989178511654e-36 Cal kit on disk : CK_SPDS1.3

C1 143.763097829496e-27

C0 30.2063121515764e-15

NIST Computed (MDJ code run by DJR script, inputs CST E'' for bead property per freq)

C3 0.137661375640095e-45

C2 6.36954177253400e-36 Cal kit on disk : CK_SPRNI.13

C1 8.37727861107735e-27

C0 29.9699831656929e-15

Bibliography

- [1] Reader, H.C. and Janezic, M.D.: Coaxial probe dielectric measurements: Practical dotting i's and crossing t's. *ARFTG conference paper*, 2006.
- [2] Marais, J.I.F.: *A Permittivity Measurement System for High Frequency Laboratories*. Ph.D. thesis, University of Stellenbosch, 2006.
- [3] Passaro, V.M.N., Dell'Olio, F. and Leonardis, F.D.: Review electromagnetic field photonic sensors. *Elsevier Progress in Quantum Electronics*, vol. 30, pp. 45–73, 2006.
- [4] Forber, R., Wang, W.C., Zang, D., Schultz, S. and Selfridge, R.: Dielectric em field probes for hpm test & evaluation. Tech. Rep., IPITEK, 2006.
- [5] Hoekman, M.: High speed electro-optical modulators. *Concept to Volume*, 1998.
- [6] Burrows, L. and Bridges, W.B.: Apparatus for magnetic field pulsed laser deposition of thin films. *United States Patent*, vol. 2001, PCT US99 26731.
- [7] Jr, M.A.M.: Verifying the performance of vector network analysers. Tech. Rep., Maury Microwave Corporation, 2006.
- [8] Badenhorst, J.: *Metrology and Modelling of High Frequency Probes*. Master's thesis, University of Stellenbosch, 2008.
- [9] Boltzmann, L.: Wien. berichte 69. Part 2, p. 795, 1874.
- [10] Krupka, J.: Precise measurements of the complex permittivity of dielectric materials at microwave frequencies. *Elsevier: Materials Chemistry and Physics*, vol. 79, pp. 195–198, 2003.
- [11] McLaughlin, B.L. and Robertson, P.A.: Miniature open-ended coaxial probes for dielectric spectroscopy applications. *Journal of Physics D: Applied Physics*, vol. 40, pp. 45–53, 2006.
- [12] Popovic, D., McCartney, L., Beasley, C., Lazebnik, M., Okoniewski, M., Hagness, S.C. and Booske, J.H.: Precision open-ended coaxial probes for in vivo and ex vivo dielectric spectroscopy of biological tissues at microwave frequencies. *IEEE Transactions on Microwave Theory and Technique*, vol. 53, pp. 1713–1722, 2005.
- [13] *A Guide to characterisation of dielectric materials at RF and microwave frequencies*. National Physical Laboratory and The institute of Measurement and Control, 2003.
- [14] Okoniewski, M., Anderson, J., Okoniewska, E., Caputa, K. and Stuchly, S.S.: Further analysis of open-ended dielectric sensors. *IEEE Transactions on Microwave Theory and Techniques*, vol. 43, pp. 1986–1989, 1995.

- [15] Popovic, D. and Okoniewski, M.: Effects of mechanical flaws in open-ended coaxial probes for dielectric spectroscopy. *IEEE Microwave and Wireless Components Letters*, vol. 12 No.10, pp. 401–403, 2002.
- [16] Gregory, A.P. and Clarke, R.N.: Dielectric metrology with coaxial sensors. *IOP Publishing - Measurement Science and Technology*, 2007.
- [17] et al., M.A.S.: Equivalent circuit of an open-ended coaxial line in a lossy dielectric. *IEEE Transactions on Instrumentation and Measurement*, vol. IM-31, pp. 116–119, 1982.
- [18] Gajda, G. and Stuchly, S.S.: An equivalent circuit of an open-ended coaxial line. *IEEE Transactions on Instrumentation and Measurement*, vol. IM-32 No.4, pp. 506–508, 1983.
- [19] Chan, T.V.C.T. and Reader, H.C.: *Understanding Microwave Heating Cavities*. Artech House Publishers, 2000.
- [20] Bulmer, C.H.: Sensitive, highly linear lithium niobate interferometers for electromagnetic field sensing. *Applied Physics Letters*, vol. 53, pp. 2368–2370, 1988.
- [21] Mann, W. and Petermann, K.: Miniaturized electro-optical e-field probe with high sensitivity. *URSI Proceedings paper*, p. p1928, 2002.
- [22] Young, P.: Electro-optic e-field sensors for shielding measurements up to 18 ghz. *IEEE International Symposium on Electromagnetic Compatibility 1995*, pp. 87–91, 1995.
- [23] Meier, T., Kostrzewa, C., Petermann, K. and Schuppert, B.: Integrated optical e-field probes with segmented modulator electrodes. *Journal of Lightwave Technology*, vol. 12, pp. 1497–1503, 1994.
- [24] Fuwen, Z., Fushen, C. and Kun, Q.: An integrated electro-optic e-field sensor with segmented electrodes. *Microwave and Optical Technology Letters*, vol. 40, pp. 302–305, 2004.
- [25] Schwerdt, M., Berger, J., Schuppert, B. and Petermann, K.: Integrated optical e-field sensors with a balanced detection scheme. *IEEE Transactions on Electromagnetic Compatibility*, vol. 39, pp. 386–390, 1997.
- [26] Yariv, A. and Pochi, P.: *Photonics, Optical Electronics in Modern Communications*. Oxford, 2007.
- [27] Alferness, R.C., Ramaswamy, V.R., Korotky, S.K., Divina, M.D. and Buhl, L.L.: Efficient single-mode fiber to titanium diffused lithium niobate waveguide coupling for $\lambda = 1.32\mu\text{m}$. *IEEE Transactions on Microwave Theory and Techniques*, vol. 30, pp. 1795–1800, 1982.
- [28] Minford, W.J., Korotky, S.K. and Alferness, R.C.: Low-loss ti:linbo3 waveguide bends at $\lambda = 1.3\mu\text{m}$. *IEEE Transactions on Microwave Theory and Techniques*, vol. 30, pp. 1790–1794, 1982.
- [29] Tsirlin, M. and Dariel, M.: Some peculiarities of ti in-diffusion in lithium niobate. *Cryst. Res. Technol.*, vol. 42, pp. 678–683, 2007.
- [30] Fouchet, S., Carencu, A., Deguet, C., Guglielmi, R. and Riviere, L.: Wavelength dispersion of ti induced refractive index change in linbo3 as a function of diffusion parameters. *Journal of Lightwave Technology*, vol. LT-5, pp. 700–707, 1987.
- [31] *OlympIOs Integrated Optics Software*. C2V, version 5.2 edn, December 2004.

- [32] Bulthuis, H.F.: *Generation of Titanium indiffused LiNbO₃ index profiles*. C2V, June 1998.
- [33] Bulthuis, H.F.: *Optimization of the voltage-length product of an EO modulator*. C2V, June 1998.
- [34] Radhakrishnan: *Apparatus for magnetic field pulsed laser deposition of thin films*. *United States Patent 6024851*, 2000.
- [35] Computer simulation technology studio suite help files.
- [36] *User's Guide, Agilent Technologies, 8510 Network Analyzer Introductory*. Agilent Technologies, 1994.
- [37] *Agilent AN 1287-1: Understanding the Fundamental Principles of Vector Network Analysis*. Agilent Technologies, 2002.
- [38] *Agilent Specifying Calibration Standards for the Agilent 8510 Network Analyser*. Agilent Technologies, 2001.